

PHD THESIS

INFLUENCE OF RESIDUAL STRESSES ON THE FATIGUE LIFE  
OF WELDED JOINTS

ANDREA CHIOCCA



Doctoral Thesis in Industrial Engineering

University of Pisa  
Cycle XXXIV– October 2021





UNIVERSITY OF PISA

---

Department of Civil and Industrial Engineering  
Doctoral Program in Industrial Engineering  
Curriculum of Land Vehicle Engineering and Transport Systems

## INFLUENCE OF RESIDUAL STRESSES ON THE FATIGUE LIFE OF WELDED JOINTS

A thesis submitted in partial fulfilment of the requirements for the degree of  
DOCTOR OF PHILOSOPHY IN INDUSTRIAL ENGINEERING  
by  
Andrea Chiocca

Supervisors  
Prof. Francesco Frendo  
Prof. Leonardo Bertini

Candidate  
Andrea Chiocca



**Don't panic.**

— Douglas Adams, *The Hitchhiker's Guide to the Galaxy*



## ABSTRACT

---

A deep knowledge of the production process is needed, in order to achieve quality and safety requirements in a structural component. As a matter of fact, manufacturing processes can introduce defects such as residual stresses, internal and superficial imperfections. Together with the inherent geometric variations, such as notches, cracks or defects in general, it is often difficult to precisely characterise the structural strength of such parts. In this context, residual stresses play an important role, especially in welded structures. The evaluation of residual stresses is typically performed using both experimental and numerical methods. Both present strengths and drawbacks which demand their combined usage to achieve a consistent and meaningful evaluation of the residual stresses. Within this scope, this PhD thesis presents an evaluation of residual stresses in a pipe-to-plate welded joint and studied their influence on the fatigue life of torsionally and bending loaded components. In the first part, the finite element method was used to assess the capability of different thermal methods used to simulate a single pass of the gas metal arc welding process in reproducing the temperature distribution around the weld bead. Results of the simulations were compared to experimental measurements of the surface temperature close to the weld region. The considered thermal techniques adopted different levels of complexity, from the basic implementation of a constant initial temperature assigned to a given material volume, to the more comprehensive and widespread Goldak's double-ellipsoid model. The study shows that, close to the weld seam, very similar thermal behaviours can be achieved by employing each one of the analysed methods. Secondly, considering the constant initial temperature method, the comparison between experimental measurements and numerical simulations showed a fairly good agreement, suggesting that a relatively simple method (i.e., requiring the setting of only one parameter) can be used to efficiently reproduce the thermal history of a welding process. In the second part, the study of residual stresses for a S355JR carbon steel pipe-to-plate welded joint is presented. Numerical simulations and experimental tests were both employed in order to gain wide-ranging knowledge. Numerical simulations were performed with the software Ansys through uncoupled thermal-structural simulations in order to evaluate the stresses, strains and temperature at each node of the finite element model for each phase of the simulation. Temperature-dependent elastic-plastic material properties were adopted in combination with the *element birth & death* method to simulate the welding process. Two different numerical approaches were implemented for reproducing the weld seam solidification process. The obtained results were discussed and compared with experimental data, in terms of relaxed radial strains measured nearby the seam weld, due to a material removal procedure. The third part investigates the influence of residual stresses on the fatigue life of the welded joints. Influencing factors such as geometric discontinuities and the material heterogeneous microstructure were considered. Experimental tests on as-welded and stress relieved specimens with fully reversed torsion and bending loading conditions were carried out. Experimental results showed how residual stresses exhibited an influence mainly on torsionally loaded components. Numerically, the uncoupled thermal-structural finite element simulation presented in the chapters before was used to assess the complete residual stress field within the specimens. Secondly, residual stresses were mapped and included as initial condition in numerical models intended for fatigue damage factors calculation. Finally, experimental results were then used to corroborate numerical models and verify their efficacy in assessing fatigue endurance. In the last part of this work, a preliminary numerical study of a notched specimen geometry is presented. The work attempts to reproduce residual stress conditions comparable to those found on the welded joint critical notch section on notched specimens thus in order to explain the results observed on welded specimens. Indeed, by varying notch radius and opening angle of a cylindrical specimen, it is possible to obtain a stress gradient similar to that obtained after the welding process at the weld notches. The use of simplified geometry allows easier analysis and a possible improved understanding of the processes taking place within the material.



## SOMMARIO

---

Per ottenere elevati standard di qualità e sicurezza in un componente strutturale, occorre una notevole familiarità con il processo di produzione. Di fatto, i processi di produzione tendono a generare difetti quali tensioni residue, imperfezioni interne e superficiali, e considerando anche le variazioni geometriche intrinseche, come intagli, cricche o difetti in generale, è spesso complesso caratterizzare con precisione la resistenza strutturale di tali parti. In questo contesto, le tensioni residue giocano un ruolo importante, specialmente nelle strutture saldate. La stima delle tensioni residue è tipicamente effettuata tramite metodi sperimentali e numerici. Entrambi presentano punti di forza e svantaggi che ne richiedono l'uso combinato in modo da ottenere una valutazione coerente e significativa delle tensioni residue. La presente tesi di dottorato si inserisce in tale ambito. Il lavoro presentato nel seguito propone uno studio sulla generazione delle autotensioni e analizza il loro effetto sulla vita a fatica di giunti saldati tubo-piastra caricati in torsione e in flessione. Nella prima parte, viene valutata la capacità di diversi metodi termici nel riprodurre la distribuzione della temperatura intorno al cordone di saldatura, utilizzando simulazioni agli elementi finiti. I risultati delle simulazioni sono stati successivamente confrontati con misure sperimentali della temperatura superficiale calcolata in prossimità al cordone di saldatura. I modelli termici considerati presentano diversi livelli di complessità, partendo da quello base, che implementa una temperatura iniziale costante degli elementi appartenenti al cordone di saldatura, al più completo e diffuso modello a doppia ellissoide di Goldak. Lo studio mostra come i diversi metodi termici impiegati, presentino comportamenti termici simili in prossimità del cordone di saldatura. In secondo luogo è stato ottenuto un buon accordo tra le misure sperimentali e quelle numeriche utilizzando un metodo semplificato (cioè che richiede l'impostazione di un solo parametro). Il seguente modello può essere utilizzato per riprodurre efficacemente la storia termica durante un processo di saldatura. Nella seconda parte, viene presentato lo studio sulle autotensioni per un giunto saldato tubo-piastra in acciaio al carbonio S355JR. Per ottenere una conoscenza più ad ampio raggio sono state utilizzate sia simulazioni numeriche che prove sperimentali. Il software Ansys è stato utilizzato per effettuare simulazioni termo-strutturali disaccoppiate e valutare così le sollecitazioni, deformazioni e la temperatura in ogni nodo del modello. Per simulare correttamente il processo di saldatura agli elementi finiti sono state implementate proprietà del materiale elasto-plastiche e dipendenti dalla temperatura mentre, per riprodurre il processo di solidificazione del cordone, sono stati analizzati due diversi approcci numerici. I risultati ottenuti sono stati discussi e confrontati con dati sperimentali di deformazioni radiali rilassate misurate vicino al cordone di saldatura e ottenute tramite una tecnica di foratura incrementale. Nella terza parte del lavoro è stata studiata l'influenza delle autotensioni sulla vita a fatica dei giunti saldati. Nell'analisi sono stati considerati fattori critici quali discontinuità geometriche e la microstruttura eterogenea del materiale. Sono state eseguite prove sperimentali sui giunti saldati in condizioni as-welded e rilassati, sottoposti a carichi di torsione e flessione. I risultati sperimentali hanno mostrato come le tensioni residue abbiano un'influenza principalmente sui componenti caricati in torsione. In questo contesto il modello termo-strutturale presentato nei capitoli precedenti è stato usato per valutare il campo completo delle sollecitazioni residue all'interno del provino, così da poterle mappare e includerle come condizioni iniziali nei modelli numerici destinati al calcolo dei fattori di danno a fatica. Infine, l'efficacia dei modelli numerici nel descrivere il danneggiamento a fatica è stata valutata tramite confronto con risultati sperimentali. Nell'ultima parte di questo lavoro viene presentato uno studio numerico preliminare su un provino con intaglio acuto. Il lavoro si pone lo scopo di riprodurre nel provino intagliato condizioni di stress residuo paragonabili a quelle riscontrate sulla sezione critica del giunto saldato. Infatti, è possibile ottenere un gradiente di stress simile a quello ottenuto dopo il processo di saldatura variando il raggio e l'angolo di apertura dell'intaglio. L'uso di una geometria semplificata permette un'analisi più accessibile e migliora la comprensione dei processi che avvengono all'interno del materiale in presenza di autotensioni e carichi affaticanti.



## PUBLICATIONS

---

Some of the concepts and figures presented in the following thesis have appeared previously in the following publications

- [1] A. Chiocca, F. Frendo and L. Bertini, 'Evaluation of heat sources for the simulation of the temperature distribution in gas metal arc welded joints,' *Metals*, vol. 9, no. 11, p. 1142, 2019, ISSN: 20754701. DOI: [10.3390/met9111142](https://doi.org/10.3390/met9111142).
- [2] ——, 'Evaluation of residual stresses in a tube-to-plate welded joint,' *MATEC Web of Conferences*, vol. 300, p. 19005, 2019. DOI: [10.1051/matecconf/201930019005](https://doi.org/10.1051/matecconf/201930019005).
- [3] ——, 'Experimental evaluation of relaxed strains in a pipe-to-plate welded joint by means of incremental cutting process,' *Procedia Structural Integrity*, vol. 28, pp. 2157–2167, 2020, ISSN: 24523216. DOI: [10.1016/j.prostr.2020.11.043](https://doi.org/10.1016/j.prostr.2020.11.043).
- [4] F. Frendo, G. Marulo, A. Chiocca and L. Bertini, 'Fatigue life assessment of welded joints under sequences of bending and torsion loading blocks of different lengths,' *Fatigue and Fracture of Engineering Materials and Structures*, vol. 43, no. 6, pp. 1290–1304, 2020, ISSN: 14602695. DOI: [10.1111/ffe.13223](https://doi.org/10.1111/ffe.13223).
- [5] A. Chiocca, F. Frendo and L. Bertini, 'Evaluation of residual stresses in a pipe-to-plate welded joint by means of uncoupled thermal-structural simulation and experimental tests,' *International Journal of Mechanical Sciences*, vol. 199, p. 106401, 2021, ISSN: 00207403. DOI: [10.1016/j.ijmecsci.2021.106401](https://doi.org/10.1016/j.ijmecsci.2021.106401).



*Culture tends to argue that it forbids only that which is unnatural.  
But from a biological perspective, nothing is unnatural.  
Whatever is possible is by definition also natural.  
A truly unnatural behaviour, one that goes against the laws of nature,  
simply cannot exist, so it would need no prohibition.*

— Yuval Noah Harari, *Sapiens: A Brief History of Humankind*

## ACKNOWLEDGEMENTS

---

First of all, I would like to thank my supervisor Prof. Francesco Frendo, without whom I would never have undertaken this experience. Although I had some doubts at the beginning, it turned out to be one of the best choices I could have made.

I would like to thank all those who made the PhD experience so much more enjoyable, through small talks, coffees and useful discussions. Starting with all PhD students of the *PhD room DICI*, up to researchers, professors and technical staff<sup>1</sup>.

Many thanks Oliver and Michele, for a brief but exiting year in the LRF.

Thanks to Salam for showing me what it means to be resolute.

To my parents for giving me the opportunity to embark on this journey.

And last but not least to *Silvia* who shared with me every moment, including the worst ones. She is the reason why I have come this far.

It is mainly because of all of you that I never considered the PhD as a job, but rather as a life experience.

## RINGRAZIAMENTI

---

Ringrazio innanzitutto il mio supervisore Prof. Francesco Frendo senza il quale non avrei mai intrapreso quest'esperienza. Sebbene fossi reticente ad iniziare il dottorato, si è rivelata essere una delle scelte migliori che potessi fare.

Vorrei ringraziare tutti coloro che hanno reso questo percorso molto più stimolante, attraverso chiaccerate, caffè e discussioni varie. A partire da tutti i dottorandi della *PhD room DICI* fino ai ricercatori, professori e personale tecnico.

Molte grazie Oliver e Michele, per l'anno passato in LRF, seppur breve ma intenso.

Grazie a Salam per avermi mostrato cosa significa essere determinati.

Alla mia famiglia, la quale mi ha dato la possibilità di iniziare questo percorso.

Per ultimo ma non meno importante ringrazio *Silvia* che ha condiviso con me ogni momento, anche i peggiori. Lei è la ragione per la quale sono arrivato fin qui.

È soprattutto grazie a tutti voi che non ho mai considerato il dottorato come un lavoro, bensì come un'esperienza di vita.

---

<sup>1</sup> Alessio, Andrea, Dario, Elena, Emanuele, Flavio, Francesco A., Francesco B., Francesco T., Gabriele , Giuseppe, Gonzalo, Leonardo, Lorenzo, Luca, Mahmoud, Marko, Matilde, Mattia, Michele S., Michele V., Mohamad, Nicola, Oliver, Paolo, Roberto, Salam



## CONTENTS

---

<b>1</b>	<b>INTRODUCTION</b>	<b>1</b>
1.1	History . . . . .	1
1.2	Motivation . . . . .	1
1.3	Outline of the work . . . . .	2
<b>I</b>	<b>LITERATURE REVIEW</b>	<b>5</b>
<b>2</b>	<b>STATE OF THE ART</b>	<b>7</b>
2.1	Fatigue assessment of welded joints . . . . .	7
2.1.1	Stress-based fatigue life estimation . . . . .	7
2.1.2	Theories of critical distances . . . . .	9
2.1.3	Notch stress approach . . . . .	10
2.1.4	Strain-based fatigue life estimation . . . . .	11
2.1.5	Critical plane approaches . . . . .	12
2.1.6	Fracture mechanics based approaches . . . . .	13
2.2	Residual stresses . . . . .	14
2.2.1	Technical standards . . . . .	14
2.2.2	Experimental methods . . . . .	14
2.2.3	Numerical methods . . . . .	15
<b>II</b>	<b>RESEARCH ACTIVITY</b>	<b>17</b>
<b>3</b>	<b>EVALUATION OF HEAT SOURCES FOR SIMULATING A WELDING PROCESS</b>	<b>19</b>
3.1	Material . . . . .	19
3.2	Thermal analysis . . . . .	20
3.2.1	Constant Initial Temperature . . . . .	22
3.2.2	Constant Volumetric Heat Flux . . . . .	23
3.2.3	Goldak's Heat Source Distribution . . . . .	23
3.2.4	Weld Pool Shape . . . . .	25
3.2.5	Experimental Set-up . . . . .	27
3.3	Results and Discussion . . . . .	28
3.3.1	Preliminary sensitivity analysis . . . . .	28
3.3.2	Results . . . . .	29
3.3.3	Comparison with Experimental Temperature Measurements . . . . .	30
3.4	Conclusion . . . . .	31
<b>4</b>	<b>EVALUATION OF RESIDUAL STRESSES</b>	<b>33</b>
4.1	Incremental hole drilling analysis . . . . .	33
4.2	Finite element analysis . . . . .	34
4.2.1	Structural analysis . . . . .	34
4.2.2	Incremental hole drilling numerical model . . . . .	38
4.3	Relaxed strain experimental measurements . . . . .	38
4.4	Results and discussion . . . . .	42
4.4.1	Experimental results of relaxed radial strain . . . . .	43
4.4.2	Strain sensitivity to dimensional variation of the weld seam geometry . . . . .	43
4.4.3	Comparison between experimental and numerical relaxed strain . . . . .	44
4.5	Residual stresses due to the welding process . . . . .	46
4.6	Conclusion . . . . .	48
<b>5</b>	<b>EXPERIMENTAL FATIGUE TESTING OF WELDED JOINTS</b>	<b>49</b>
5.1	Material and methods . . . . .	49
5.2	Experimental analyses . . . . .	50
5.2.1	Fatigue analysis . . . . .	50
5.2.2	Microstructure analysis . . . . .	52
5.2.3	Fracture analysis . . . . .	54

5.3	Experimental results . . . . .	56
5.4	Conclusion . . . . .	57
6	NUMERICAL SIMULATION OF THE FATIGUE DAMAGE	59
6.1	Thermo-structural analysis . . . . .	59
6.2	Fatigue analysis . . . . .	61
6.3	Numerical results . . . . .	64
6.4	Conclusion . . . . .	67
7	RESIDUAL STRESSES INFLUENCE ON THE FATIGUE STRENGTH OF STRUCTURAL COM- ONENTS	69
7.1	Material and method . . . . .	69
7.2	Finite element model . . . . .	69
7.3	Results . . . . .	71
7.4	Conclusion . . . . .	72
8	CONCLUSION	73
	III APPENDIX	75
A	FINITE ELEMENT MODELS COMPARISON	77
A.1	Finite element analysis . . . . .	77
A.1.1	Thermal analysis . . . . .	78
A.1.2	Structural analysis . . . . .	78
A.2	Results and discussion . . . . .	79
B	ANALYTICAL MODELS FOR EVALUATING RESIDUAL STRESSES	81
B.1	Membrane-Plate & Williams theories . . . . .	81
B.1.1	Membrane model . . . . .	82
B.1.2	Plate model . . . . .	83
B.1.3	Williams model . . . . .	85
B.2	Results and discussion . . . . .	87
	BIBLIOGRAPHY	89

## LIST OF FIGURES

---

Figure 1	Thesis layout flowchart . . . . .	4
Figure 2	Example of fatigue design curve for International Institute of Welding (IIW) . . . . .	8
Figure 3	Usage of structural hot-spot stress method . . . . .	8
Figure 4	Graphical representation of the Point Method (PM) . . . . .	9
Figure 5	An example of strain life curve using the Coffin-Manson relation with material constants $\sigma'_f$ , $\epsilon'_f$ , $b$ , $c$ of Aluminium Alloy 6061 series, obtained from [76] . . . . .	11
Figure 6	Williams model with free-free edges boundary condition . . . . .	13
Figure 7	Image of the investigated specimen (a), micrograph of the weld seam (b) and technical drawing of the pipe-to-plate welded joint with dimensions in millimetres and welding representation according to ISO 22553:1992 (c) . . . . .	20
Figure 8	Temperature dependent thermal material properties derived from [108] . . . . .	21
Figure 9	Meshed specimen (bottom) and simulation techniques applied on the welding seam: constant initial temperature (a), constant heat flux (b), and Goldak's double-ellipsoid model (c) . . . . .	22
Figure 10	Activated elements for the Constant Initial Temperature (CIT) model with a temperature of $T_i$ (a) cross section of the weld seam (b) . . . . .	23
Figure 11	Coordinate system transformation between global and local reference frame, for Goldak's double-ellipsoid model . . . . .	24
Figure 12	Goldak's heat source parameters estimated directly by examining the fusion zone	24
Figure 13	Goldak's double-ellipsoid model: overview of the thermal solution (a), finite element model cross section of the weld seam (b), real cross section of the weld seam (c) . . . . .	26
Figure 14	Heat flux model: overview of the thermal solution (a), finite element model cross section of the weld seam (b), and real cross section of the weld seam (c) . . . . .	26
Figure 15	Constant initial temperature: overview of the thermal solution (a), finite element model cross section of the weld seam (b), and real cross section of the weld seam (c) . . . . .	26
Figure 16	Experimental set-up for temperature measurement (a) and FE-model (b) of the simplified specimen . . . . .	27
Figure 17	Real specimen's geometry (a), simplified specimen's geometry (b) . . . . .	28
Figure 18	Relative error percentage with respect to the maximum temperature of the reference curve . . . . .	29
Figure 19	Behaviour of the curve temperature vs. time at a distance of 3 mm from the weld toe, for a $\pm 30\%$ modification of thermal conductivity . . . . .	29
Figure 20	Temperature vs. Time curve of the thermal models employed, specifically for three points on the surface of the plate . . . . .	30
Figure 21	Comparison between experimental and numerical results of temperature over time	31
Figure 22	Experimental machining of the bottom part of the specimen plate (a), numerical simulation of the incremental cutting process (b) . . . . .	33
Figure 23	Incremental hole drilling process used to detect relaxed strains (a) and qualitative layout of the strain gauges (b) . . . . .	34
Figure 24	Temperature dependant structural material properties of S355 steel acquired from [108] . . . . .	35
Figure 25	Weld seam volume segment for the <i>classic</i> (a) and <i>RWP</i> (b) methods; cooling sequence of a weld seam section during the structural simulation for the <i>classic</i> (c) and <i>RWP</i> (d) methods . . . . .	36
Figure 26	Graphic representation of the iterative process required to perform the <i>RWP</i> method (a), and example of active and inactive elements evolution in a weld seam section (b) . . . . .	37

Figure 27	<i>Test-1</i> specimen, with eight strain gauges applied at a $90^\circ$ step angle (a); <i>Test-3</i> specimen with twelve applied strain gages with $30^\circ$ step angles (b) . . . . .	39
Figure 28	Technical drawing of the strain gauges positioning over a small arc of circumference (a), picture of the actual bead geometry at the point of application of the $0.6\text{ mm}$ grid length strain gauges (b) . . . . .	40
Figure 29	Relaxed radial strain over specimen hoop coordinate measured through $1.5\text{ mm}$ grid length strain gauges for a fixed strain gauge radial distance of $\Delta r_{ext} = 6.5\text{ mm}$ . The mean value line was obtained considering only group <b>B</b> measurements . . . . .	42
Figure 30	Relaxed radial strain data over the hoop coordinate measured through $0.6\text{ mm}$ grid length strain gauges; mean values are plotted as continuous lines . . . . .	43
Figure 31	Comparison between numerical and experimental data of relaxed radial strains over distance from the weld toe for two different incremental hole depths in the group <b>B</b> . Experimental results are presented through mean value and standard deviation while numerical results are the convex hull of $\varepsilon_{Rrr}$ data obtained in the angular domain $\theta \in (60^\circ, 300^\circ)$ . . . . .	44
Figure 32	Cross-sectional view of the base plate and weld bead with outlined the bending and skin effects due to the incremental cutting process . . . . .	45
Figure 33	Comparison between numerical and experimental data of relaxed radial strains over distance from the weld toe for two different incremental hole depths in the group <b>A</b> . Experimental results are reported through of mean value and standard deviation while numerical results are the convex hull of $\varepsilon_{Rrr}$ data obtained for two angular domains $\theta \in [-60^\circ, 60^\circ]$ . . . . .	46
Figure 34	Overall residual radial stress field on the plate surface ( $z = 0$ ), for a radial domain $r \in [42\text{ mm}, 78\text{ mm}]$ , together with a graphical representation of the domain under consideration . . . . .	46
Figure 35	Overall residual hoop stress field on the plate surface ( $z = 0$ ), for a radial domain of $r \in [42\text{ mm}, 78\text{ mm}]$ , together with a graphical representation of the domain under consideration . . . . .	47
Figure 36	Technical drawing of the investigated pipe-to-plate welded joint with dimensions in millimetres and welding representation according to ISO 22553:1992 . .	49
Figure 37	Test-bench employed for fatigue testing (a), pipe-to-plate welded joint (b) and micrography of the weld seam (c) . . . . .	50
Figure 38	Optical microscope micrograph of the joint in As-Welded (AW) condition. Focus on the weld toe showing Fusion Zone (FZ), Coarse Grain Zone (CGZ), Fine Grain Zone (FGZ) and Base Material (BM) (a). Detail of the microstructure transition between FZ and CGZ (b), CGZ and FGZ (c), FGZ and BM (d) . . . . .	52
Figure 39	Optical microscope micrograph showing the microstructures of the BM (a), FGZ (b), CGZ (c) and FZ (d) of the joint in the AW condition; the subfigures (e-h) show the corresponding microstructures of the joint in the SR condition . . . . .	53
Figure 40	Vickers hardness distribution around the weld toe in as-welded and stress relieved conditions . . . . .	54
Figure 41	Fractured surfaces from torsional loading: plate view (a) and pipe view (b) . .	54
Figure 42	Fractured surfaces from bending loading: plate view (a) and pipe view (b) . .	55
Figure 43	Fractured surfaces for pure bending (a) and pure torsion (b) loading . . . . .	55
Figure 44	Nominal stress range over number of cycles to break-through for pure bending loading in as-welded and stress relieved conditions; expected vs. experimental number of cycles to break-through are displayed in the top right corner of the figure . . . . .	56
Figure 45	Nominal stress range over number of cycles to break-through for pure torsion loading in as-welded and stress relieved conditions; expected vs. experimental number of cycles to break-through are displayed in the top right corner of the figure . . . . .	57
Figure 46	Flow chart of the uncoupled thermal-structural simulation for residual stresses evaluation in the pipe-to-plate welded joint . . . . .	59

Figure 47	Example of cooling sequence during the structural simulation for the Representative Welding Process ( <a href="#">RWP</a> ) method for a cross section of the weld seam . . . . .	<a href="#">60</a>
Figure 48	Radial and hoop residual stress on the upper plate surface with indication of the angular coordinate (i.e. run in-run out point at $0^\circ$ ) and weld bead deposition area (i.e. between red lines); together with a graphical representation of the domain under consideration . . . . .	<a href="#">61</a>
Figure 49	Finite element models for the linear-elastic analysis and elastic-plastic sub-model analysis for fatigue damage parameters evaluation . . . . .	<a href="#">62</a>
Figure 50	Examples of cross sections of the weld root to highlight shape heterogeneity . . . . .	<a href="#">63</a>
Figure 51	Pure bending and pure torsion hydrostatic stress and <i>Fatemi-Socie</i> critical plane factor in the weld root (a) and weld toes (b), (c); hydrostatic stress and critical plane factor values are related to a nominal stress range of $143 \text{ MPa}$ in bending and $250 \text{ MPa}$ in torsion . . . . .	<a href="#">65</a>
Figure 52	<i>Fatemi-Socie</i> critical plane factor over nominal stress range under pure bending for a load ratio $R = -1$ . . . . .	<a href="#">65</a>
Figure 53	<i>Fatemi-Socie</i> critical plane factor over nominal stress range under pure torsion for a load ratio $R = -1$ . . . . .	<a href="#">66</a>
Figure 54	<i>Fatemi-Socie</i> critical plane factor over the number of cycles to break-through for pure bending and pure torsion loading in as-welded and stress relieved conditions . . . . .	<a href="#">67</a>
Figure 55	Weld seam cross section dimensional analysis (a), and dimensions of the notch specimen based on the weld root radius evaluation (b) . . . . .	<a href="#">69</a>
Figure 56	3D finite element model of the notched specimen used for simulating torsional loading (a), 2D finite element model of the notched specimen used for simulating traction/compression loading (b) . . . . .	<a href="#">70</a>
Figure 57	True stress and strain results obtained from three tensile tests performed on S355 structural steel specimens . . . . .	<a href="#">70</a>
Figure 58	Hydrostatic stress for a pipe-to-plate welded joint over the crack path starting from the weld root; <a href="#">AW</a> and Stress Relieved ( <a href="#">SR</a> ) conditions, before and after torsional fatigue loading are shown . . . . .	<a href="#">71</a>
Figure 59	Hydrostatic stress for a notched specimen over the notch section; <a href="#">AW</a> and <a href="#">SR</a> conditions, before and after torsional fatigue loading are shown . . . . .	<a href="#">71</a>
Figure 60	Hydrostatic stress for a pipe-to-plate welded joint over the crack path starting from the weld root; <a href="#">AW</a> and <a href="#">SR</a> conditions, before and after bending fatigue loading are shown . . . . .	<a href="#">72</a>
Figure 61	Hydrostatic stress for a notched specimen over the notch section; <a href="#">AW</a> and <a href="#">SR</a> conditions, before and after tensile fatigue loading are shown . . . . .	<a href="#">72</a>
Figure 62	3D and 2D FE-models . . . . .	<a href="#">78</a>
Figure 63	2D simulation results comparison for different initial temperatures ( $T_i$ ) of the welding seam. . . . .	<a href="#">79</a>
Figure 64	2D simulation results comparison for different initial temperatures $T_i$ and material properties (M.p. = Partial multi linear elastic-plastic, M.c. = Complete multi linear elastic-plastic) . . . . .	<a href="#">79</a>
Figure 65	Comparison between numerical and experimental results for different cutting depth. . . . .	<a href="#">80</a>
Figure 66	Weld seam shrinkage effect on the global deformation of the component . . . . .	<a href="#">81</a>
Figure 67	Axisymmetric membrane-plate model and Williams' notch theory . . . . .	<a href="#">82</a>
Figure 68	Membrane model with a constant radial load $p_o$ over the plate thickness $h$ . . . . .	<a href="#">82</a>
Figure 69	Plate model with a constant momentum load $M_o = \frac{p_o h}{2}$ over the thickness . . . . .	<a href="#">83</a>
Figure 70	Solution deriving from superposition of membrane and plate theory for $p_o = 5000 \text{ N mm}^{-1}$ . . . . .	<a href="#">88</a>
Figure 71	Solution deriving from Co and C1 continuity between Williams' theory and the membrane-plate theory for $p_o = 5000 \text{ N mm}^{-1}$ . . . . .	<a href="#">88</a>

Figure 72	Qualitative comparison between analytical and numerical residual radial stress fields on the plate surface resulting after the implementation of Williams' solution; the solution of the analytical model is represented by means of the grid-like surface . . . . .	88
Figure 73	Qualitative comparison between analytical and numerical residual hoop stress fields on the plate surface resulting after the implementation of Williams' solution; the solution of the analytical model is represented by means of the grid-like surface . . . . .	88

## LIST OF TABLES

---

Table 1	FAT values based on the Notch Stress Approach ( <a href="#">NSA</a> ) according to [75]. The stress ranges (MPa) refer to a number of cycle to failure of two million cycles, a stress ratio $R = 0.5$ and a probability of survival of $P_s = 97.7\%$ . . . . .	<a href="#">11</a>
Table 2	Welding process parameters . . . . .	<a href="#">19</a>
Table 3	Chemical composition (wt%) of S355JR steel . . . . .	<a href="#">19</a>
Table 4	Chemical composition (wt%) of EN ISO 14341-A G 464 filler material (i.e. catalog values) . . . . .	<a href="#">19</a>
Table 5	Mechanical properties of S355JR structural steel at room temperature . . . . .	<a href="#">20</a>
Table 6	Numerical input parameters employed during the calibration of the models. . . . .	<a href="#">25</a>
Table 7	Thermocouples' distance from the welding seam: $d$ = distance, $N^\circ$ = thermocouple's number . . . . .	<a href="#">28</a>
Table 8	Summary of experimental test set-up for relaxed radial strain measurements . . . . .	<a href="#">39</a>
Table 9	Summary of experimental relaxed strains measurements in <i>italic</i> ( $\mu\epsilon$ ) for 1.5 mm grid length strain gauges and hole diameter $d = 100\text{ mm}$ . . . . .	<a href="#">41</a>
Table 10	Summary of experimental relaxed strains measurements in <i>italic</i> ( $\mu\epsilon$ ) for 0.6 mm grid length strain gauges and hole diameter $d = 100\text{ mm}$ . . . . .	<a href="#">42</a>
Table 11	Experimental results of as-welded specimens under pure bending ( <b>B</b> ) and pure torsion ( <b>T</b> ) loading (load ratio $R = -1$ ) . . . . .	<a href="#">51</a>
Table 12	Experimental results of stress relieved specimens under pure bending ( <b>B</b> ) and pure torsion ( <b>T</b> ) loading (load ratio $R = -1$ ) . . . . .	<a href="#">52</a>

## ACRONYMS

---

**AW** As-Welded

**BC's** Boundary Conditions

**BM** Base Material

**CIT** Constant Initial Temperature

**CGZ** Coarse Grain Zone

**CVHF** Constant Volumetric Heat Flux

**DIY** Do It Yourself

**FEA** Finite Element Analysis

**FEM** Finite Element Method

**FGZ** Fine Grain Zone

**FZ** Fusion Zone

**GHSD** Goldak's Heat Source Distribution

**GMAW** Gas Metal Arc Welding

**HAZ** Heat Affected Zone

**ICM** Imaginary Crack Method

**IIW** International Institute of Welding

**LEFM** Linear Elastic Fracture Mechanics

**LM** Line Method

**NSA** Notch Stress Approach

**NSIF** Notch Stress Intensity Factor

**PM** Point Method

**PSM** Peak Stress Method

**RWP** Representative Welding Process

**SED** Strain Energy Density

**SR** Stress Relieved

**TCD** Theory of Critical Distances

## INTRODUCTION

---

### 1.1 HISTORY

Welding is one of the best known and most important processes used for joining metal components together. Known since the Middle Ages for joining iron parts through heating and hammering, it developed into the process we know today around the beginning of the 20<sup>th</sup> century. As a matter of fact, welding, as a process of local fusion, had to wait for the development of electric generators powerful enough to melt iron. This process has also become increasingly popular thanks to the invention of coated electrodes, which have greatly improved the quality of welded joints. A major surge in the use and research of welding took place during the Second World War. During the conflict, in addition to faster construction of vehicles, welding also made it possible to carry out quick and easy vehicle repairs. Today, the existing welding methods have grown enormously. They range from automated welding, which allows precision and speedy processes, to welding in hostile environments such as the seabed, which is widely used in the construction and repair of oil & gas platforms.

Welding allows the indissoluble bound of both identical and, in some cases, dissimilar materials and comes in different varieties depending on the nature of the joint to be created. One of the main characteristics is the creation of monolithic structures that present nearly uniform mechanical strength and environmental resistance. Welding can be used to join components of very different sizes and shapes. It allows the production of a wide variety of joint geometries suitable for diverse applications. The main fields of application range from heavy industry (e.g. mechanical, civil, nuclear, aerospace and chemical engineering), to large production sectors (e.g. automotive and manufacturing in general) to the Do It Yourself ([DIY](#)) sector.

### 1.2 MOTIVATION

During the welding process many mechanisms take place simultaneously, e.g. inelastic deformations, temperature gradients, and phase transformation to name a few. One of the main drawbacks related to these mechanisms is the generation of residual stresses. Especially tensile residual stresses are often degrading for the integrity and durability of a component; for this reason, their study and evaluation should be recommended starting from the design phase. Residual stresses are commonly associated with unexpected failures and dimensional inaccuracies. In particular, they can affect a component strength, by reducing the strain resistance [1], the fatigue life [2] and by promoting stress-corrosion failures [3]. Sometimes, residual compressive stresses are intentionally introduced, in order to increase the strength of a part (e.g. shot peening and plastic deformation used to increase the fatigue endurance of automotive helical springs [4]). For the optimized design of a component, for example aimed at reducing the weight and/or costs (i.e. lightweight design), the accurate knowledge of the state of stress, including residual stresses, is highly recommended.

From a general perspective, two major approaches exist for residual stresses evaluation. The first one is experimental; here a series of limitations and difficulties exist regarding the different techniques that can be used. The experimental evaluation of residual stresses is always obtained by indirect ways [5]. Some methods are based on the elastic deformation or displacement produced by the removal of a given (stressed) material volume: the most commonly employed methods include destructive techniques (e.g. sectioning method [6]) or semi-destructive techniques (e.g. hole drilling [7]); other, non-destructive, methods are based on the alteration of wave transmission properties induced by the crystal lattice deformation associated to residual stresses (e.g. neutron diffraction [8] and ultrasound [9], [10]). Unfortunately, experimental procedures are often highly conditioned, both for destructive and non-destructive tests. Successful measurements depend heavily on the stress gradient. In addition, experimental measurements result complex in case of three-dimensional stress fields and are susceptible of evaluation errors due to algorithm inversion. For these reasons it is difficult to obtain complete

and statistically relevant results through experimental tests alone [11], [12]. An example is given by the extensive experimental campaign carried out through the NeT project [13], where the comparison of several experimental measurements (i.e. performed through different techniques) shows significant different residual stress results.

The second approach is numerical, mostly thorough Finite Element Analysis (**FEA**). In facts, in the last decades, numerical methods have been applied for predicting residual stresses resulting from manufacturing processes such as casting [14]–[18], welding [19]–[30] and additive manufacturing [31]–[36]. This technique allows easy computing of residual stresses, although some limitations exist because of the large number of parameters involved in the process (e.g. transient behaviour, heat sources, phase transformations, temperature distribution, temperature dependent materials properties, etc.). The results may be biased by the simplifications introduced in the model in order to make it computationally efficient (e.g. simplified component geometry and material properties). A valid application of the **FEA** lies in understanding how different input parameters affect the simulation results. In this way **FEA** becomes a valuable tool, easily accessible and with less economic effort than experimental tests, which can be time consuming and expensive.

Several studies can be found relative to finite element analysis of residual stress, both for bi- and three-dimensional problems, some examples are: Zhou et al. [37] analysed the influence of residual weld stresses on creep behaviour, Barsoum et al. [2] obtained a forecast of the stresses that will later be incorporated into a crack growth model and Wang [38] computed residual stresses in a welded specimen for a later use of them in a multiaxial fatigue assessment study.

What makes the numerical evaluation of residual stresses challenging is often the multi-physics environment involved. Simulations are highly dependent on material properties and the boundary conditions employed. In order to obtain an accurate simulation of a welding process, thermal and structural simulations must be carried out. The two macro-categories of multiphysics simulations that can be performed involve either uncoupled or coupled approaches. In the first case, the solution of one environment depends sequentially on the solution of another but not the opposite. In this way all the environments involved are solved independently starting with the one that presents no dependencies. In the second case, the different environments are solved simultaneously since the solution of one depends on the knowledge of the others. Uncoupled thermo-structural simulations are normally carried out in the scientific literature when welding, casting or additive manufacturing processes are involved. In fact, as the displacements obtained during these processes are limited and have a negligible influence on the thermal distribution, the uncoupled formulation is acceptable in this context [39]. Although the recent developments in computing methods allowed multi-physics simulations to become increasingly time-efficient and trustworthy, the combined application of experimental procedures is currently necessary for the accurate validation of numerical results.

### 1.3 OUTLINE OF THE WORK

The following section will explain how the work has been organized through the thesis. For a better understanding the reader is referred to Figure 1 which provides a schematic flowchart showing the arguments of the various chapters.

As introductory part of the thesis ([chapter 2](#)), a state of the art analysis was performed. The topics addressed here include the two core subjects of this research project: fatigue assessment and residual stresses in welded joints. The two topics were dealt with separately, firstly presenting the most commonly used methods for fatigue assessment and then introducing residual stresses both from the point of view of standards and as regards their calculation both experimentally and numerically.

In the *first part* of the research work ([chapter 3](#)), the investigation focused on numerical aspects related with the thermal simulation, and in which way the material thermal properties affected the results. The process parameters and joint geometries were kept fixed, as they are both well known, while uncertainties in the material parameters were considered as being the main issue. Other authors already studied the effect of the production process; see, for example, the effect of the heat source distribution, energy input and welding speed on temperature variation as discussed by [40]. Furthermore, a comparison of different simulation techniques of the welding process were discussed to understand to what extent simplified models can be adopted to simulate the temperature distribution close to the weld. Three numerical methods were considered: a Constant Initial Temperature (**CIT**) of

the welding seam elements, Constant Volumetric Heat Flux ([CVHF](#)) and the well known Goldak's Heat Source Distribution ([GHSD](#)) [41]. The Goldak's double-ellipsoid heat source distribution was taken as the reference welding simulation process, as it is widely used in the literature ([42]–[44]). The [CIT](#) technique [45] and the [CVHF](#) [19] were compared with Goldak's double-ellipsoid model to appreciate the differences in the simulated thermal behavior of the three models. In addition, a sensitivity analysis was performed to rank the parameters in order of importance, thus determining the ones that exhibit the greatest influence on simulation results. Finally, a comparison of the temperature profile during a welding process was made between the simplified [CIT](#) model and temperature data obtained by means of thermocouple readings.

In the *second part* ([chapter 4](#)) a comprehensive analysis of residual stress on a pipe-to-plate welded joint was carried out using both numerical and experimental analyses. An uncoupled thermal-structural simulation has been used in Ansys FE software. This kind of simulation is commonly used for welding processes, as already shown by different authors [46]–[50]. The welding process was replicated by means of the *element birth & death* technique<sup>2</sup>, combined with a heat source model [CIT](#). Numerical results were corroborated by comparison with several experimental results. The adopted heat source model has already been validated [chapter 3](#), while the structural analysis was verified through comparison with relaxed strains, which were experimentally obtained by an incremental cutting process performed from the bottom of the plate [51].

In the *third part*, an experimental ([chapter 5](#)) and numerical ([chapter 6](#)) analysis are presented regarding the influence of residual stresses on the fatigue life assessment of a pipe-to-plate welded joint made of structural steel S355JR. The aim was to determine whether welding residual stresses exhibit an influence on the fatigue life of a pipe-to-plate welded component, under different loading conditions.

In [chapter 5](#), the experimental fatigue assessment is discussed regarding a pipe-to-plate welded joint in As-Welded ([AW](#)) and Stress Relieved ([SR](#)) conditions, under fully reversed (i.e. load ratio  $R = -1$ ) bending and torsion. In addition, the microstructure of the Fused Zone ([FZ](#)), Heat Affected Zone ([HAZ](#)) and Base Material ([BM](#)) were studied for both [AW](#) and [SR](#) conditions, thus to better understand microstructure influence on the fatigue life assessment of the welded joint.

Afterwards in [chapter 6](#), the numerical analysis is presented and validated by comparison with experimental results. Specifically, the solution of the uncoupled thermal-structural simulation presented in [chapter 4](#) was used by mapping residual stresses generated after the welding process. Subsequently, an elastic-plastic structural simulation was performed to determine damage due to fatigue loading in as-welded and stress-relieved conditions.

In the *fourth part* ([chapter 7](#)), a preliminary numerical analysis was carried out on a notched specimen geometry made of S355 structural steel. The analysis provides an insight into the generation process and general performances of residual stresses in presence of a notch. In particular, the hydrostatic stress behaviour was examined, which, as already highlighted [chapter 6](#), proved to be an important predictor to assess the residual stresses influence on the fatigue life of welded joints. The comparison of numerical results was made on the critical section for both the notched and welded specimen, in the presence and without residual stress. The critical section of the welded specimen consists of the propagation path of a majority of the cracks within the weld bead, while the notch ligament section was utilised for the notched specimen. The results showed how, for both geometries examined, a similar pattern of hydrostatic stresses occurred during loading. The aim of the analysis was to identify a suitable notched geometry to describe the fatigue damage process found in the welded joint. As a matter of fact, the notched geometry allows an advantageous numerical and experimental investigation respect to the welded joint.

---

<sup>2</sup> This method requires the deactivation and reactivation of the bead elements, by multiplying the stiffness matrix with a coefficient close to zero or one respectively.

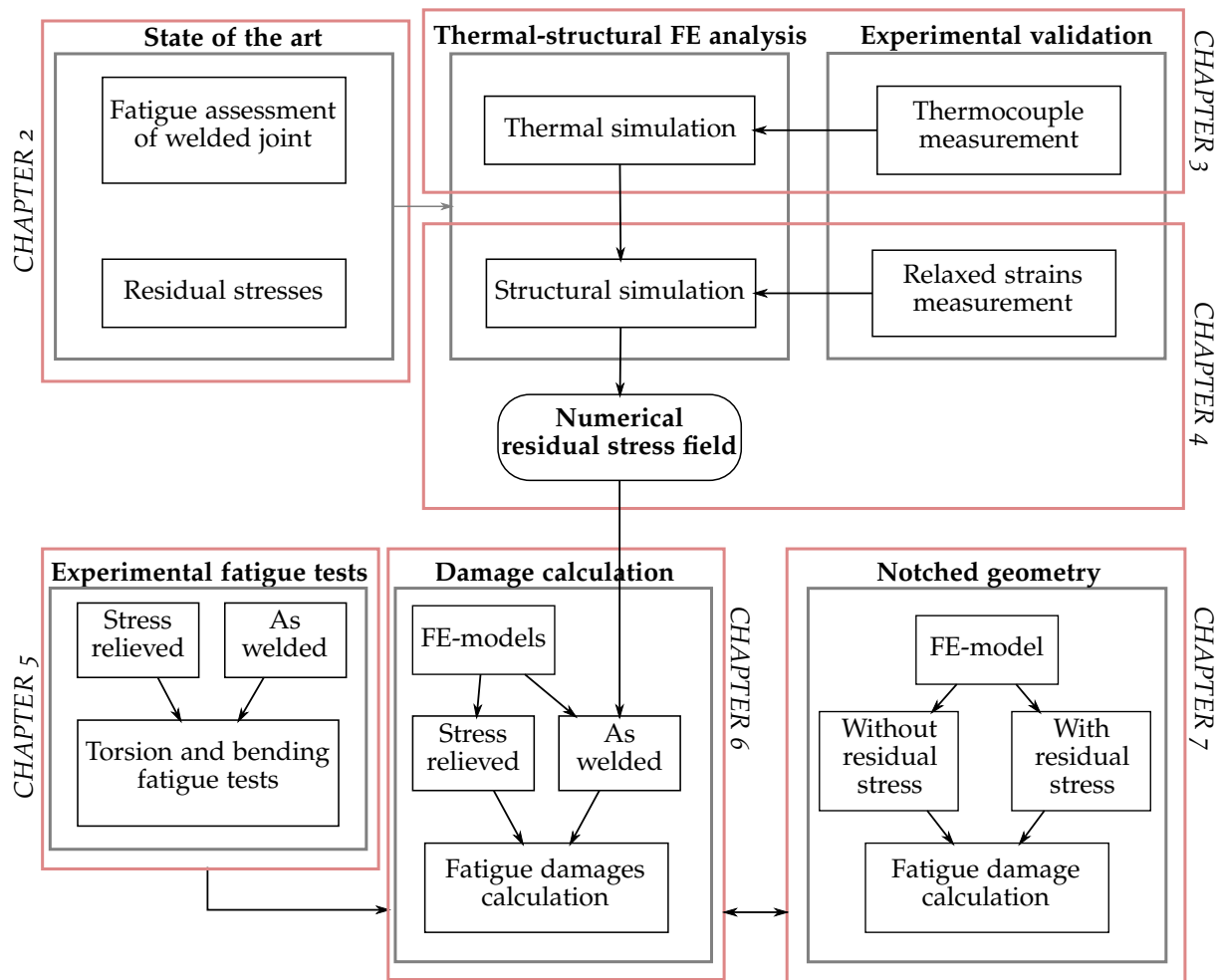


Figure 1: Thesis layout flowchart

Part I  
LITERATURE REVIEW



# 2

## STATE OF THE ART

---

Fatigue failure of a metallic component is mainly driven by repeated plastic deformations over a small volume of material; in contrast to instantaneous failure, which requires extensive plasticisation over the whole resistant section. Since fatigue is a typically localized phenomenon that affects the resistance of the whole body, it is good practice to pay attention to geometrical details such as notches and stress concentration points in order to prevent it. Particularly for welded joints, a combination of different critical factors can lead to a component failure in unexpected ways. It is therefore of paramount importance to employ the proper assessment method according to the problem to be solved. No method is the best, in fact, it mainly depends on different factors such as the available information, stage of design, type of component, consequences of the failure, etc.

In the following the most widespread criteria adopted for fatigue assessment of welded components will be presented together with their discussion. It is worth noting how several notable articles present an overview or state of the art about fatigue assessment methods for welded joints [52], [53].

### 2.1 FATIGUE ASSESSMENT OF WELDED JOINTS

#### 2.1.1 Stress-based fatigue life estimation

The stress life approach was the first one developed, in the context of fatigue, by Wöhler (1860 ca.). Under this approach evolved the concept of *endurance limit*, that refers to the stress amplitude below which the material is expected to show an infinite life. These methods consider mainly linear-elastic stress state and are suggested to be used for high cycle fatigue life regime.

**NOMINAL STRESS METHOD** The nominal stress method is among the most straightforward and basic methods that can be applied to welded joints. It is recommended by both Eurocode 3 [54] and the IIW [55]. Nominal stresses are calculated based on the conventional formulae of beam theory and calculate stresses without considering intensifications due to notches. Fatigue assessment is performed by comparing the nominal stress range obtained for a particular joint geometry with the fatigue design curve corresponding to the structural detail under investigation. The calculation of nominal stresses can be performed on rather simple joint geometries or by simplifying more complex joint geometries. In fact both Eurocode 3 and the IIW propose a list of structural details on which the experimental curves are derived. It is highly recommended to consider structural details which resemble the studied geometry since the reported design curves are based on extensive experimental campaigns. Each of these design curves is defined by a detail category [54], or FAT value for [55]. As the underlying approach between Eurocode 3 and IIW is similar, solely the IIW approach will be reported below.

The FAT value represents the stress range at two million cycles for a survivability of  $P_s = 97.7\%$  at a stress ratio  $R = 0.5$ . The underlying assumption is that all SN curves for welded joints present the same pattern and can therefore be differentiated based on a single parameter (FAT) related to the structural detail investigated. The shape of the curves, shown in Figure 2, presents a knee point at  $1 \times 10^7$  cycles and a slope of  $k = 3$ . Furthermore, experimental evidences have shown that no fatigue limit exist [56], therefore the curve continues with a slope of  $k = 22$ .

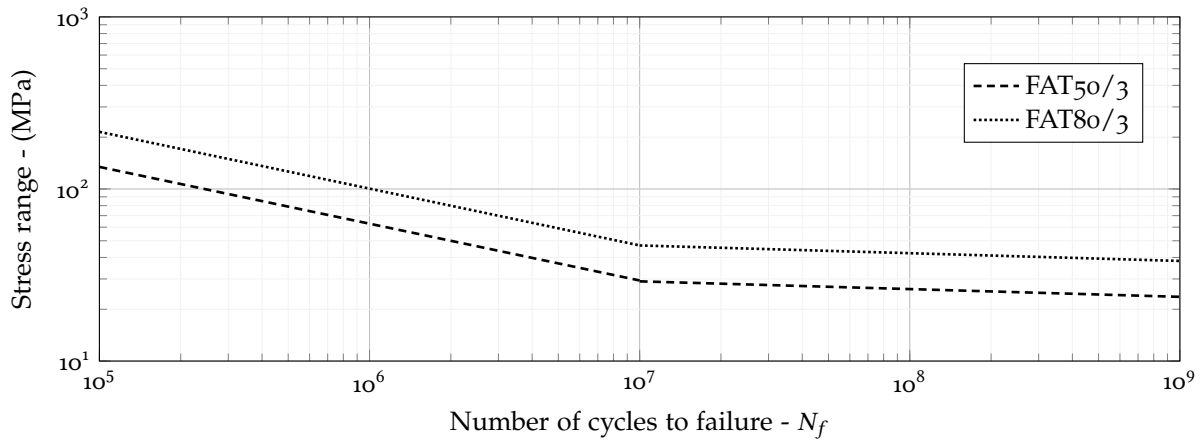


Figure 2: Example of fatigue design curve for IIW

The nominal stress method provides the main advantage of ease of use, as it involves simple analytical formulas. All the time-consuming steps associated with the finite element method are therefore skipped. However, it suffers from many disadvantages which reduce its utility to specific cases. First of all, it is not possible to always define a nominal stress as the method is restricted to well defined geometries. Some geometrical sections present different stress states if different planes are considered (i.e. tubular T-joint). In addition, nominal stresses do not take macro-geometrical notch factors into account. In fact, it is not possible to calculate nominal stresses by means of Finite Element Method (FEM), as FEM considers geometrical stress concentrators, resulting in a local and no longer nominal stress result. In addition, since every structural detail requires special experimental tests, aspects such as scale factors, variation of the welding process, etc. are not considered. This makes it necessary to use high scatter and safety factors.

**HOT-SPOT STRESS METHOD** If a nominal stress has to be calculated via FEM or experimental measurements, the most accurate option to use is the hot-spot stress. As mentioned before, for very complicated welded joints the stress value changes frequently and it is not guaranteed to find a joint category for which the nominal stress method can be applied. The structural hot-spot stress includes all macro-structural effects of the joint excluding those due to the local weld profile. Thus, the structural stress depends on the overall dimensions and the loading parameters as defined by IIW [55]. The method, as defined by IIW, cannot be used for weld root assessment but only for weld toe.

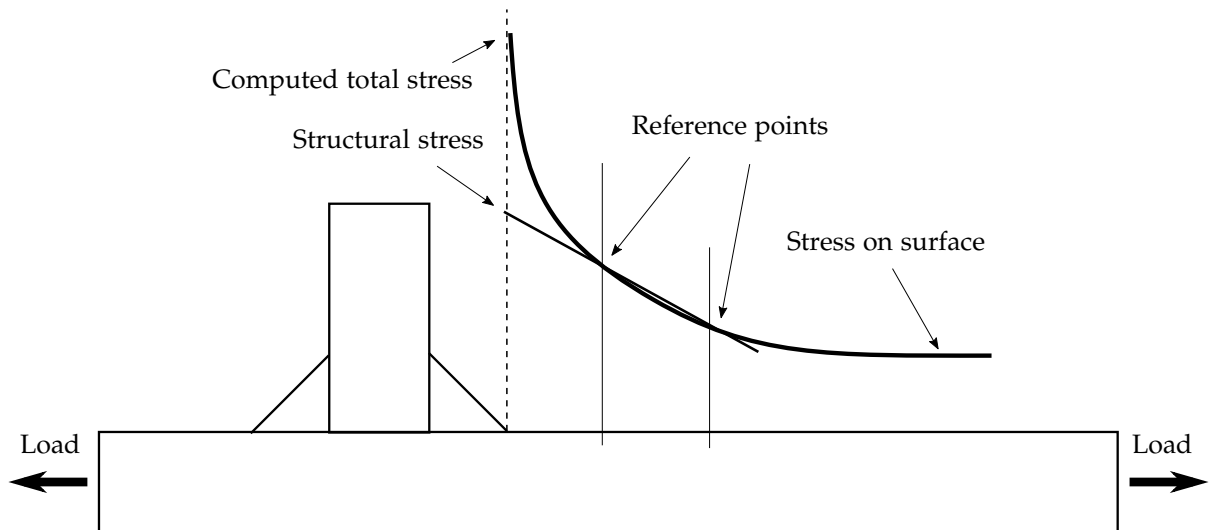


Figure 3: Usage of structural hot-spot stress method

The structural stress is calculated by numerical or experimental extrapolation, as shown in Figure 3. The reference points can be two or three and their distance from the weld toe is defined in the standards (e.g.  $0.4t$ , where  $t$  represents the plate thickness).

### 2.1.2 Theories of critical distances

A popular group of methods that gained increasing importance in recent times belong to the Theory of Critical Distances (TCD) [57]. These models assume that failure begins when the stress in a certain process zone reaches a critical value. This stress is normally called the effective stress  $\sigma_{eff}$ , and is defined as the value of the calculated stress at the critical length ( $a$ ) away from the notch (Figure 4). Initially formulated by Neuber ([58], [59]) the idea of the critical distance has evolved into different theories which adopt the same core concept. Several methods have been developed as modifications of the local fatigue criterion. To date models can be distinguished for averaging stresses on different geometric scales. The different formulations are:

- the Point Method (PM), under this method, an elastic stress analysis is performed and failure is expected when the stress reaches a critical value at a specific distance from the notch [60], [61];
- the Line Method (LM), resembles the PM, except that the stress is calculated as an average along a line starting from the root of the notch [62]. This method was the first one developed belonging to the TCD family [58] and is also commonly referred to as Neuber's stress averaging method [63]. Other similar methods involve averaging stress over areas and volumes [63]–[65];
- the Imaginary Crack Method (ICM), is a fracture mechanics based approach. The existence of a crack at the root of the notch is assumed. Failure is expected to occur when this crack reaches the critical stress intensity factor. An example on the application of this method is El Haddad equation [66], successfully employed for defining the non-propagating region for short and long cracks.

These models are frequently employed for multiaxial fatigue analyses of potentially complex geometries as their functioning is well established using linear-elastic finite element analyses, thereby reducing design time and costs [67].

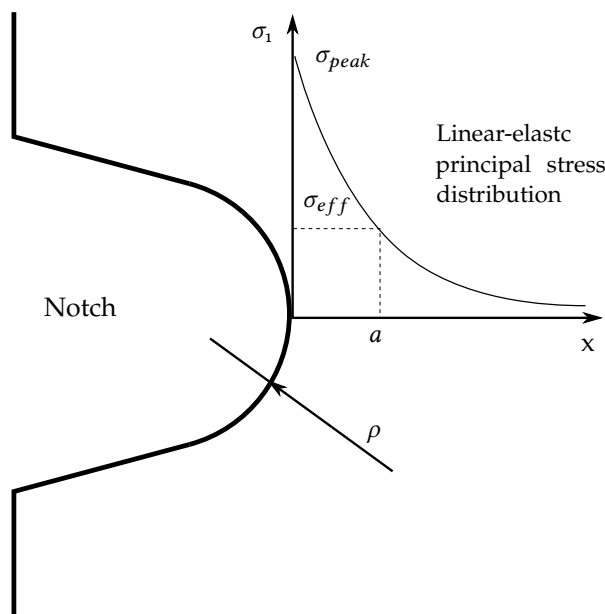


Figure 4: Graphical representation of the PM

The majority of methods belonging to the TCD share a common formulation and they mainly diversify for the definition of the effective stress. An example is reported in Equation 1–2, where the effective stress for the PM and LM are shown.

$$\sigma_{eff} = \sigma_1(x = a) \quad (1)$$

$$\sigma_{eff} = \frac{1}{\rho^*} \int_0^{\rho^*} \sigma_1(x) dx \quad (2)$$

where  $\rho^*$  is the microstructural length and  $a$  is the critical distance, while  $\sigma_1$  is the principal stress. Both  $\rho^*$  and  $a$  are considered as material parameters that can be evaluated by experimental fatigue testing [63] or found in literature. Once these material parameters are provided the effective stress can be evaluated through linear-elastic FEM calculation of the linear elastic principal stress distribution.

### 2.1.3 Notch stress approach

Among local methods, one of the most popular to assess fatigue life of welded joints is the Notch Stress Approach (NSA). The NSA applies in a rather direct way, by evaluating the elastic stress field over a varied component geometry. In practice, the notches of the component are all fictitiously scaled up to a fixed value. At this point, the range of maximum stress variation on the notches is considered in order to correlate the fatigue load to the component remaining life. Since the stress state in the presence of a notch is multiaxial, it is necessary to use an equivalent stress in order to employ NSA. Typically, the von Mises stress or the maximum principal stress are used, the former in the presence of ductile material behaviour and the latter in the presence of brittle material [52].

It is based on Neuber's concept of microstructural support (i.e. Equation 2), already presented in the previous Section 2.1.2. Neuber reformulated his model because of the difficulty in performing numerical integrations at that time (1940 ca.). Instead of calculating an effective (averaged) stress on the actual geometry of the notch with radius  $\rho$ , as shown in Equation 2, he calculated the maximum stress on a notch with enlarged radius  $\rho_f$  (Equation 3).

$$\rho_f = \rho + s\rho^* \quad (3)$$

where  $\rho$  is the notch radius and  $s$  is the support factor, which depends on many factors, such as the type of load, multi-axial notch conditions, notch opening angle and the strength criterion employed. The value of  $s$  ranges widely and requires a complex evaluation since it is influenced by so many parameters [68].

NSA was developed in its modern formulation by Radaj [69], [70] that assumed, for steel components, the worst case  $\rho = 0$ , in combination with a multiaxiality factor  $s = 2.5$  and the micro-support length  $\rho^* = 0.4 \text{ mm}$ , finally proposing  $\rho_f = 1 \text{ mm}$ .

NSA offers many advantages, especially in the presence of notches of irregular and variable geometry (e.g. welded joints). In these cases the notches do not have to be measured experimentally due to the fact that the model is based on the worst case scenario with zero notch radius ( $\rho = 0$ ). In addition, from a geometric perspective the notch is enlarged, which enables a better evaluation by FEM programs, using coarser meshes. Finally, since the method is based on linear elastic material theory, a linear elastic finite element model becomes sufficient. However, the method suffers when non-proportional multiaxial loads are used. By using equivalent stresses based on rotational invariants of the stress tensor, many non-proportionality effects are not taken into account.

This method is also recommended in guidelines and regulation codes such as [71], [72]. The fatigue strength of a welded component can be studied by means of SN curves, based on material, reference radius and chosen equivalent stress. A significant amount of experimental evidence exists to provide indications of particular types of FAT. An example is the extensive experimental investigations carried out by Sonsino [73]–[75] which lead to the FAT values shown in Table 1.

Table 1: FAT values based on the NSA according to [75]. The stress ranges (MPa) refer to a number of cycle to failure of two million cycles, a stress ration  $R = 0.5$  and a probability of survival of  $P_s = 97.7\%$

	$\rho = 1 \text{ mm}$		$\rho = 0.05 \text{ mm}$	
	Principal Stress	von Mises	Principal Stress	von Mises
Steel	225	300	630	560
Aluminium	71	63	180	160
Magnesium	28	25	71	63

#### 2.1.4 Strain-based fatigue life estimation

When observing the behaviour of traditional metallic materials such as steel or aluminium, it can be noted that after yielding, a significant increase in plastic strain occurs even with small variations in stress. This behaviour is mainly due to the severe reduction of the material stress-strain curve slope. In this context, i.e. when high material plasticisation occurs, methods based on linear elastic stresses prove to be unreliable for fatigue assessment. Experimentally, it has been shown that fractures in materials with ductile behaviour are governed by shear plastic deformation resulting in the formation of permanent slip bands.

The application of strain-based methods is widely used in the fatigue study of notched components. In these cases, indeed, the presence of a notch subjected to an external load creates high plastic deformation which results in high stress/strain concentration.

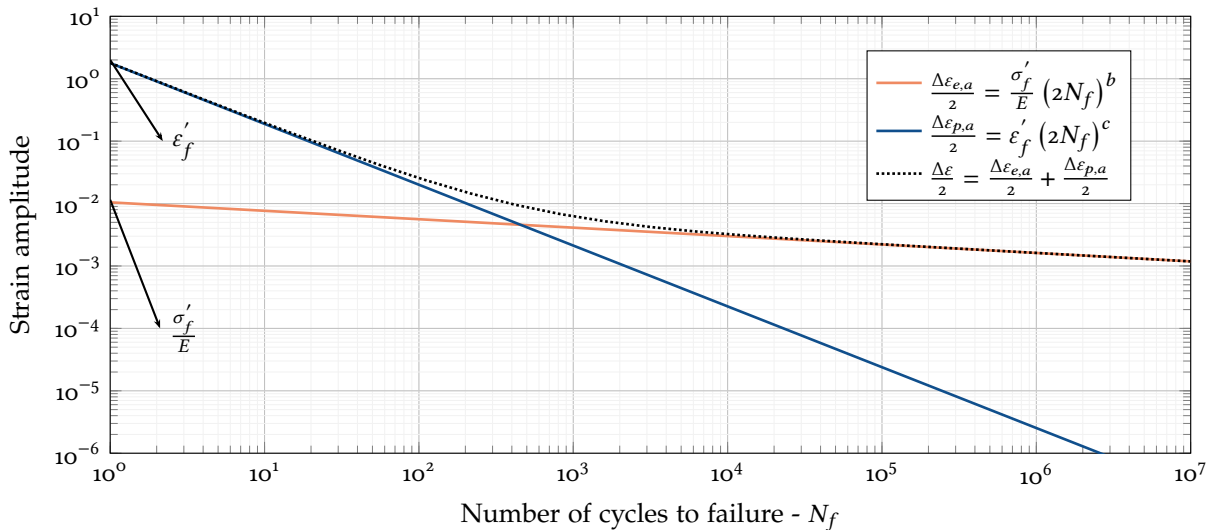


Figure 5: An example of strain life curve using the Coffin-Manson relation with material constants  $\sigma'_f$ ,  $\varepsilon'_f$ ,  $b$ ,  $c$  of Aluminium Alloy 6061 series, obtained from [76]

The most widely used law in this field is the Coffin-Manson [77], [78] relation, shown in Equation 4 and Figure 5. Fatigue assessment is done by means of a strain-life curve described by the law:

$$\frac{\Delta\varepsilon}{2} = \frac{\Delta\varepsilon_{e,a}}{2} + \frac{\Delta\varepsilon_{p,a}}{2} = \frac{\sigma'_f}{E} (2N_f)^b + \varepsilon'_f (2N_f)^c \quad (4)$$

where  $\frac{\Delta\varepsilon}{2}$  represents the total strain amplitude,  $\frac{\Delta\varepsilon_{e,a}}{2}$  is the elastic strain amplitude,  $\frac{\Delta\varepsilon_{p,a}}{2}$  is the plastic strain amplitude,  $E$  is the Young's modulus,  $\sigma'_f$  is the fatigue strength coefficient,  $\varepsilon'_f$  is the fatigue ductility coefficient,  $b$  is the fatigue strength exponent and  $c$  is the fatigue ductility exponent.

Material dependent constant, such as  $\sigma'_f$ ,  $\varepsilon'_f$ ,  $b$  and  $c$ , can be found in standards or literature more generally and are derived experimentally from fatigue tests (e.g. standard procedure ASTM No.E606).

### 2.1.5 Critical plane approaches

The idea behind critical plane approaches assumes that a favourite plane exists on which the crack propagates. This plane, which is related to the geometry of the part, and to the type of loading, suffers from a more damaging stress-strain history than the other planes. In the case of critical plane models, it is assumed that the crack does not exist in the component initially, and the orientation in which the highest damaging action occurs is assumed to be the one in which the crack nucleates.

These models therefore consist of two main steps, the first being the identification of the critical plane and the second the calculation of the damage. These steps are highly influenced by the definition of the critical plane parameter (i.e. damage parameter) and the choice of the type of load used. Common practice identifies the directions of maximum damage along the direction of maximum shear strain if the material is ductile, while along the direction perpendicular to the maximum stress for brittle behaviour. In the following, some critical plane models will be introduced, although the list is not exhaustive yet it reports some of the most common models used in research.

Among the first models proposed is Findley's model [79], as shown in Equation 5. This criterion is typically used to study fatigue at high cycle since it is based on stress quantities.

$$FI = \frac{\Delta\tau}{2} + k_{FI}\sigma_n \quad (5)$$

The damage parameter  $FI$  is nominally calculated for each plane as the sum of the magnitude of the shear stress  $\frac{\Delta\tau}{2}$  with the acting normal stress normal to the plane  $\sigma_n$  multiplied by the material constant  $k_{FI}$ .

Similarly to Findley critical plane concept, Brown and Miller proposed a critical plane model [80] valid for the low cycle regime which is presented in Equation 6. In this case, the parameter is calculated in terms of deformational and non-stress quantities.

$$BM = \frac{\Delta\gamma_{max}}{2} + k_{BM}\varepsilon_n \quad (6)$$

where  $\frac{\Delta\gamma_{max}}{2}$  is the strain amplitude on the maximum shear strain plane,  $\varepsilon_n$  is the normal strain on this plane and  $k_{BM}$  is a material fitting constant.

More recently critical plane parameters were proposed in the attempt to reproduce the physical nature of fatigue damage during multiaxial fatigue loading. Among the most successful models we can find the Fatemi-Socie model [81] presented in Equation 7.

$$FS = \frac{\Delta\gamma}{2} \left( 1 + k_{FS} \frac{\sigma_n}{S_y} \right) \quad (7)$$

where  $\Delta\gamma$  is the tangential strain amplitude,  $\sigma_n$  represent the maximum stress acting perpendicular to the shear plane,  $S_y$  is the yield strength of the material and  $k_{FS}$  is a material constant. This criterion is typically used for ductile materials and its use is normally coupled with non-linear material models. In fact, the local plasticity that occurs, especially in notches, is very common in several components and often leads to local overcoming of yielding.

Another important critical plane factor is the Carpinteri-Spagnoli (C-S) model [82]. The C-S critical plane factor is a high-cycle multiaxial fatigue criterion. The orientation of the critical plane is linked to the mean directions of the principal stress axes and to the fatigue properties of the material. The latter dependence is taken into account through a rotation angle  $\delta$ , as shown in Equation 8.

$$\delta = \frac{3\pi}{8} \left[ 1 - \left( \frac{\tau_{af}}{\sigma_{af}} \right)^2 \right] \quad (8)$$

where  $\tau_{af}$  and  $\sigma_{af}$  represent the endurance fatigue limit in fully reversed torsion and fully reversed bending respectively. The C-S model is usually applied for hard metal and in high cycle fatigue regimes, for this reason its formulation considers only stress quantities and is generally evaluated using linear elastic material models.

### 2.1.6 Fracture mechanics based approaches

In fracture mechanics, the most general methods applicable in the case of linear-elastic behaviour of the material are well known Linear Elastic Fracture Mechanics (LEFM) and Notch Stress Intensity Factor (NSIF), the latter proposed by Lazzarin and Tovo [83]. To report an example of stress intensity factors, Equation 9 reports Williams' analytical stress distributions [84] over a notch (i.e.  $K_I$  for mode I and  $K_{II}$  for mode II) and the NSIF definition  $K_{III}$  for mode III [85]. For terminology please refer to the articles already cited [84], [85]

$$\begin{aligned} K_I &= \sqrt{2\pi} \lim_{r \rightarrow 0} (\sigma_{\theta\theta})_{\theta=0} r^{1-\lambda_1} \\ K_{II} &= \sqrt{2\pi} \lim_{r \rightarrow 0} (\tau_{r\theta})_{\theta=0} r^{1-\lambda_2} \\ K_{III} &= \sqrt{2\pi} \lim_{r \rightarrow 0} (\tau_{z\theta})_{\theta=0} r^{1-\lambda_3} \end{aligned} \quad (9)$$

It should suffice to mention that the whole Williams' theory is based on the Airy stress function  $\Phi$  of Equation 10. The scalar potential function  $\Phi$  is used to calculate stresses for 2D problems by applying equilibrium equations to stress components defined in Cartesian coordinates as  $\sigma_{xx} = \frac{\partial^2 \Phi}{\partial y^2}$ ,  $\sigma_{yy} = \frac{\partial^2 \Phi}{\partial x^2}$  and  $\tau_{xy} = \frac{\partial^2 \Phi}{\partial x \partial y}$ .

$$\begin{aligned} \Phi &= r_w^{\lambda+1} F(\psi) \\ F(\psi) &= e_1 \sin(\lambda + 1)\psi + e_2 \cos(\lambda + 1)\psi + e_3 \sin(\lambda - 1)\psi + e_4 \cos(\lambda - 1)\psi \end{aligned} \quad (10)$$

where  $\Phi$  depends from the polar coordinates  $(r_w, \psi)$  (shown in Figure 6), the general parameters  $e_1, e_2, e_3, e_4$  and the exponent  $\lambda$ . Being interested in the non trivial solution, it is desired to find the minimum value of  $\lambda$  that nullifies the determinant of the system obtained from Equation 10 after applying the boundary conditions of the problem of interest.

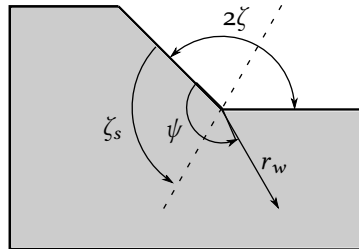


Figure 6: Williams model with free-free edges boundary condition

The main difference between LEFM and NSIF lies in the nature of the defect considered. Both consider that a defect already exists in the material but if LEFM considers this defect with a sharp V-notch with null opening angle, NSIF generalises to a sharp V-notch with arbitrary opening angle. Being both based on the linear-elastic material behaviour approximation, the methods assume that the volume of plasticised material around the crack is negligible. Both LEFM and NSIF can be applied by means of analytical formulae, although these formulations are based on different simplifying assumptions. A more reliable calculation can be conducted through numerical approaches such as FEM. However, for an accurate NSIF calculation via FEM, a very fine mesh must be used in the area of the notch e.g. in the order of  $10^{-5} m$ .

**AVERAGE STRAIN ENERGY DENSITY** A method derived from the NSIF but which overcomes the difficulty linked to the dependence on the opening angle of the notch is the Strain Energy Density (SED). Proposed by Lazzarin and Zambardi [86], this method proposes to use the elastic strain energy density averaged over an area of radius  $R_o$  centred on the notch tip.

**PEAK STRESS METHOD** A further development of the NSIF is the Peak Stress Method (PSM). The concept behind PSM is to evaluate the stress in a notch through the use of FEM with coarse mesh. The method correlates the stress in the flaw (i.e. peak stress) with the NSIF without the use of time

consuming numerical models. Initially proposed by Nisitani and Teranishi [87] to calculate the NSIF of an elliptical cavity loaded in mode I, it was later improved and generalised by Meneghetti [88]–[91].

## 2.2 RESIDUAL STRESSES

Estimating the fatigue strength of welded joints is a particularly complex problem due to the significant changes introduced by the thermal welding cycle. The microstructural changes in the material generally favours a more brittle behaviour. Furthermore, thermal gradients developed during the process originate residual stress fields or significant distortions and misalignments in the component. Specifically, the subject of residual stresses will be covered below. Methods and standards used for residual stresses assessment and calculation will be described and discussed.

### 2.2.1 Technical standards

Several standards exist which consider the effect of residual stresses on the structural integrity of different structural components such as energy systems, naval industry, pressure vessels and welded joints in general. Among the most important we find the Eurocode 3 [54], the IIW [55], the British Standard BS7910 [92] and the American API 579/ASME FFS-1 [93]. Standards consider residual stresses in a variety of ways although always with rather simplified approaches, which leads often to very conservative assessments. Some standards consider residual tensile stresses already present within the procedure to be used. Therefore, they do not provide any modifications in case as-welded components, while they introduce correction factors for considering compressive residual stresses. Specifically Eurocode and IIW consider the presence of residual stresses in the detail category and FAT curves as a result of experimental investigations performed on big size specimens<sup>3</sup>. The experimental investigations include the effects of several factors such as: stress concentrations of the detail category, local stress concentrations, weld imperfections, load direction, high tensile residual stresses, welding process and metallurgical conditions. Other methods are based on fracture mechanics and deal mainly with procedures for assessing flaws in metal components by considering fracture, fatigue and corrosion. The BS7910 provides recommended residual stress profiles on specific joint geometries and weld types, all based on upper bound fits of experimental and analytical data. Residual stresses profile are usually expressed through high order polynomial equations in order to calculate stress intensity factors including the presence of residual stresses. Similarly, the API 579 is a fracture mechanics based standard and provides parametric through-thickness residual stress profiles for pipe and vessels based on residual stresses measurement data. In both cases the stresses are divided in membrane and bending component and parametric formulation are provided in order to include a broad spectrum of weld dimensions.

### 2.2.2 Experimental methods

The experimental measurement of residual stresses is a highly investigated and discussed topic due to its importance in the industrial world. Many qualitative and quantitative methods exist for the measurement of residual stresses. However, all these techniques are indirect, as they measure strain-based rather than stress-based quantities. In the following, the two main groups of methodologies for measuring residual stress will be described, namely destructive and non-destructive techniques. The first group involves the destruction of the residual stress/strain equilibrium state in the component. This procedure is carried out in several steps, firstly by creating a new stress state through the removal of material, then calculating the local strain variation and then calculating the residual stresses using analytical or numerical approaches.

Among the best known methods in this field is the sectioning method [94]. This method is among the first to be developed (1888 ca.). By sectioning the component, the released strains are calculated using strain gauges. Particular care must be taken not to introduce plasticity during the cutting process and to apply the strips correctly for strain reading. Temperature variations have been identified as a major source of error for this method but can be eliminated by the combined use of a reference bar of the

---

<sup>3</sup> Where the presence of residual stresses is not negligible

same material.

A second method, proposed by Prime, is the contour method [95]. This is based on the superposition principle assuming that during relaxation the material behaves elastically and that the cutting process does not introduce stresses. The method involves cutting the component, normally done by wire electric discharge machining. Subsequently, the deformation of the cut surface is calculated with a very high definition (e.g. using coordinate measuring machines). At this point the residual stresses are calculated by measuring the surface contours using a FE-model.

Finally, one of the most versatile and easy methods is hole drilling. It is probably the most widely used destructive (i.e. semi-destructive) technique today as it is also largely standardised. It consists of creating a hole in the centre of a rosette made by several strain gauges in order to calculate the local deformation. The geometry of the rosette as well as the drilling process is standardised by ASTM E837-08 [96].

The second group adopts non-destructive methods based on the relationship between residual stress and the physical or crystallographic parameters of the material.

Among the best known methods in this field is the ultrasonic technique. It relies on changes in the speed of ultrasonic waves, which may be correlated to the residual stress state via the material elastic constants [97]. This method is based on the acoustoelastic effect, that relates the speed of the sound in the stressed material  $V$  and the one in the stress-free material  $V_0$  with the residual stress  $\sigma_r$  through an acoustoelastic constant  $K$ , as shown in Equation 11.

$$V = V_0 + K\sigma_r \quad (11)$$

Another important non-destructive technique uses X-ray and neutron diffraction. The diffraction methods involve measuring lattice deformations by studying variations in the lattice spacing of polycrystalline material. The different wavelength involved leads to different penetration in the material, some millimetres for neutron beam and tens of micron for X-rays.

### 2.2.3 Numerical methods

Recently, purely numerical models for calculating residual stresses have become increasingly popular. These models mainly use FEM to solve multi-physics analyses and obtain the residual stress range in the component. By means of numerical simulation, it is possible to know the solution for the whole domain, in contrast to experimental methods, which only allow local measurement of the value of residual stresses. Numerical simulations used for calculating residual stresses are employed in many different fields, the most popular of which include casting [14], [16]–[18], [98], additive manufacturing [31]–[36], welding [19]–[27], [29], [30], [99], [100] and machining processes in general [101]–[104]. In the above mentioned areas, residual stresses are mainly generated by non-linear thermal processes or by plasticisation. Whenever a thermal process is involved, multiphysical simulations are required, mainly thermal-structural, which can be performed in a coupled or uncoupled way. In the uncoupled formulation, the hypothesis is that the structural solution depends from the thermal solution but not the opposite. In this way the thermal analysis is primary solved and subsequently the temperatures results are imported in the structural analysis. This assumption is acceptable whenever the deformations of the component do not considerably influence the instantaneous temperature field [105].

In the coupled case, both thermal and structural environments are solved simultaneously, which requires much more computational resources. This type of simulation is suggested whenever there is a significant mutual influence between the two environments, i.e. the component deformation has an effect into the local temperature field [106].

Today, practically all major FEM software implement the possibility of multi-physics simulations. In all cases, it is necessary to implement both thermal and mechanical temperature-dependent material properties in order to achieve consistent results. For the thermal simulation, if a moving source is required, different heat source models can be implemented, which typically vary according to the process to be simulated. Among the best known are the Gaussian distribution heat source [107] and Goldak's double ellipsoid heat source [41]. These simulate the temperature trend normally due to processes deriving from sources such as arc welding or beam sources. For a correct implementation of the heat source, some parameters must be set, which vary in number depending on the model taken

as reference. These parameters can be taken from literature or from experimental tests. The structural simulation will automatically utilise the temperature information for calculating deformative quantities (i.e. via the thermal expansion coefficient) and thus derive stresses by means of the constitutive properties of the material.

Part II  
RESEARCH ACTIVITY



# 3

## EVALUATION OF HEAT SOURCES FOR THE SIMULATION OF THE TEMPERATURE DISTRIBUTION IN GAS METAL ARC WELDED JOINTS

### 3.1 MATERIAL

The studied model refers to the pipe-to-plate welded joint geometry shown in Figure 7a, with a cross section of the weld seam presented in Figure 7b. A technical drawing of the specimen is also shown in Figure 7c. The specimen presented in Figure 7, includes a tube reinforced internally through a circular plate and then welded to a flange by means of a single pass of Gas Metal Arc Welding (GMAW) through a TransPlusSynergic 4000 machine. The welding process was carried out manually, by maintaining the welding torch stationary and using a rotating bench whose speed was controlled, as required, by the operator. As a result, a high repeatability of the welding process was guaranteed. The welding process parameters, used as benchmark for all the simulations, are given in Table 2. Both the plate and the tube were made by structural steel S355JR, while the filler material was an EN ISO 14341-A G 464. The chemical compositions of both the base and filler materials are given in Table 3 and Table 4 respectively; while the mechanical properties of the base material are shown in Table 5, where  $R_{p0.2}$  is the yield strength,  $R_m$  is the tensile strength,  $E$  is the Young's modulus,  $G$  is the tangential modulus,  $\nu$  is the Poisson's ratio and  $HB$  is the Brinell microhardness.

As shown in Figure 7c, the tube has an internal diameter of 44 mm and a wall thickness of 10 mm, while the plate to which it is welded to, is quadrangular, with 190 mm edge length and 25 mm of thickness. Four holes, with a diameter of 21 mm, were symmetrically drilled into the plate. The holes as well as the internal volume created by the circular support were necessary for a fatigue assessment investigation of the welded joint later presented in Chapter 5. Likewise, a central gas thread of 1/4 of inches (G1/4 of standard ISO 7-1:1994) was used to pressurize the lower chamber and detect a through-the-thickness crack during fatigue testing.

Table 2: Welding process parameters

Current (A)	Voltage (V)	Welding Time (s)	Welding Speed ( $mm s^{-1}$ )
211	25	75	2.7
Filler material	Wire diameter (mm)	Shielding gas	Gas flowrate ( $m^3 h^{-1}$ )
EN ISO 14341-A G 464	1.20	82% Ar 18% CO <sub>2</sub>	0.62

Table 3: Chemical composition (wt%) of S355JR steel

C	Si	Mn	P	S	N	Cu
0.24	0.55	1.6	0.035	0.035	0.012	0.55

Table 4: Chemical composition (wt%) of EN ISO 14341-A G 464 filler material (i.e. catalog values)

C	Si	Mn	Cu
0.065–0.08	0.90–1.00	1.60–1.70	max. 0.30

Table 5: Mechanical properties of S355JR structural steel at room temperature

$R_{p0.2}$ (MPa)	$R_m$ (MPa)	$E$ (GPa)	$G$ (GPa)	$\nu$	$HV_{10}$
355	470	206	77.4	0.3	160

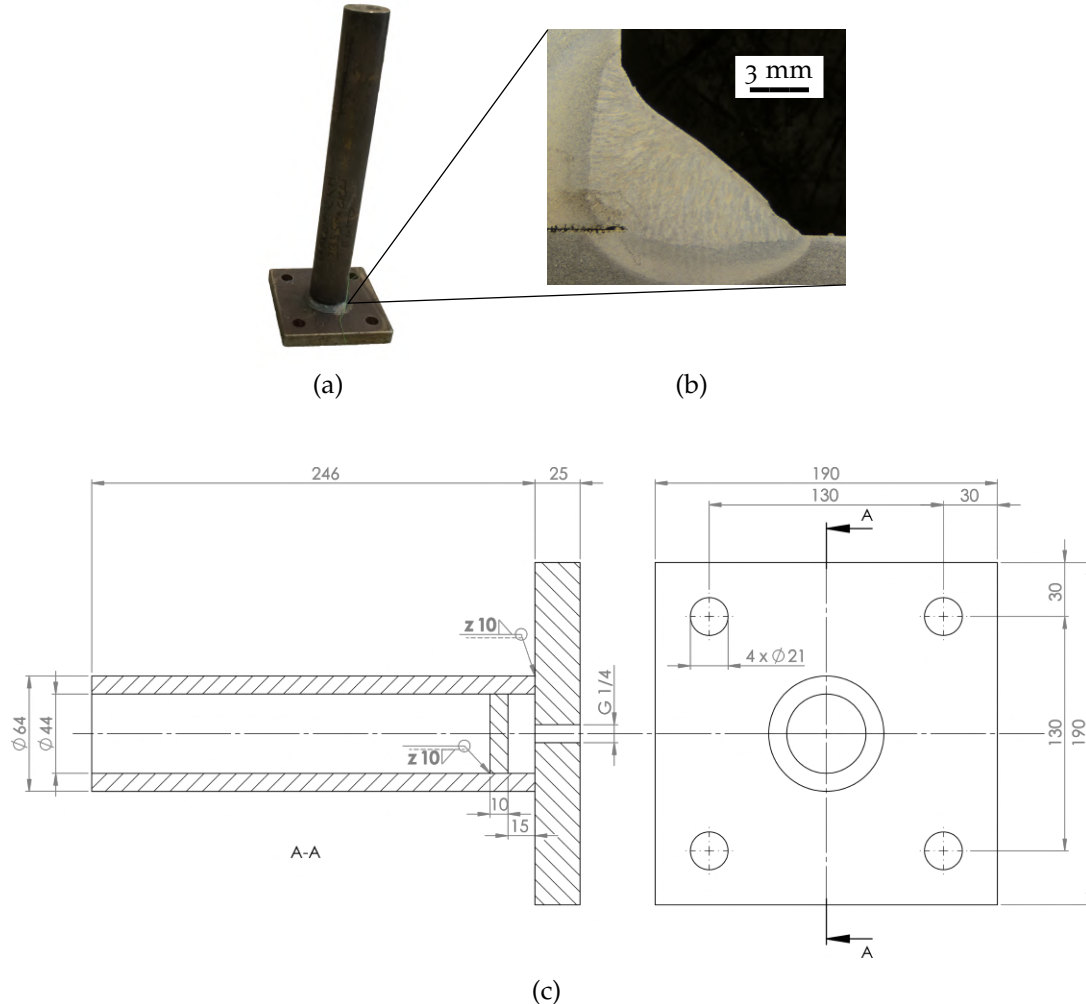


Figure 7: Image of the investigated specimen (a), micrograph of the weld seam (b) and technical drawing of the pipe-to-plate welded joint with dimensions in millimetres and welding representation according to ISO 22553:1992 (c)

### 3.2 THERMAL ANALYSIS

Numerical simulations were performed using the Ansys 19.2 software. Specifically, a transient nonlinear simulation was used for the thermal analysis, employing temperature dependant material properties. Furthermore, a full 3D model was used to take into account the asymmetry caused by the welding operation, which distributes heat over the specimen progressively in a hoop direction. The choice of a 3D model was based on a preliminary analysis carried out on the same joint geometry in which differences in results between two- and three-dimensional analysis and linear-elastic and elastic-plastic material properties were identified. The interested reader can refer to [Appendix A](#). A SOLID70 element was adopted for the 3D analysis; it is a brick with eight nodes that uses the temperature as the only degree of freedom. The temperature-dependent thermal material properties were collected from [108]. The simulated molten pool shape is commonly calibrated by means of experimental comparison, varying the thermal conductivity at high temperatures. Due to the difficulty in

experimentally validating this quantity, a fictitious thermal conductivity at 2273 K was implemented based on [108] (as shown in Figure 8), which employed the same welding process and material here described.

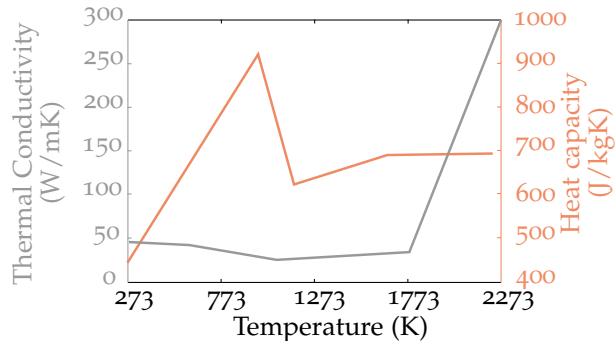


Figure 8: Temperature dependent thermal material properties derived from [108]

Meanwhile, both convection and radiation were considered constant. The heat convection coefficient was set to a value of  $20 \text{ W m}^{-2} \text{ K}^{-1}$  on all the surfaces except the bottom one in order to correctly simulate the heat transfer between steel and air. In particular, for the bottom surface, the heat sink effect was considered, as a result of contact with the metallic support during welding; the heat convection coefficient was set to a value of  $500 \text{ W m}^{-2} \text{ K}^{-1}$ , which is comparable to the one used by [109]. In addition, the radiation was taken into account through the emissivity coefficient set at 0.79 at ambient temperature. Generally, the convection is significant for lower temperatures than radiation; instead, for temperatures close to the material melting point, radiation is more relevant. However, no sensitivity was detected for emissivity and convection coefficients in the set of values found in the literature, as shown in Section 3.3.1.

The main focus of the simulation was the thermal analysis of the welding process. Three different methods were considered and used to evaluate their capability in reproducing the experimental results. The selected methods are listed below:

- Constant Initial Temperature (**CIT**), as explained in Section 3.2.1;
- Constant Volumetric Heat Flux (**CVHF**), as explained in Section 3.2.2;
- Goldak's Heat Source Distribution (**GHSD**), as explained in Section 3.2.3.

The thermal analysis follows the equilibrium Equation (12), as described by [110] :

$$k \left( \frac{\partial^2 T}{\partial x^2} + \frac{\partial^2 T}{\partial y^2} + \frac{\partial^2 T}{\partial z^2} \right) + Q_{int} = \rho c_p \frac{\partial T}{\partial t}, \quad (12)$$

where  $Q_{int}$  is the internal heat source rate, and  $k$ ,  $c_p$ , and  $\rho$  are the conductivity, specific heat and density of the material, respectively. Figure 9 qualitatively illustrates the three techniques applied in the FE-models; in particular, the parameters of Figure 9a-c are described in the following sections. In Figure 9a, a set of elements is chosen and an initial temperature of  $T_i$  is assigned to them, after which, the cooling process is simulated by a transient thermal simulation. In Figure 9b, constant volumetric heat flux is applied to the elements belonging to the weld seam. The model activation time is a function of the total welding time and the number of activated elements; while, in Figure 9c, a double-ellipsoid function is used to select the nodes depending on their coordinates with subsequent application of a volumetric heat flux whose intensity depends from the node coordinates.

It can be immediately noticed that one of the main differences among the applied methods is the number of parameters on which they depend, one for **CIT**, three for **CVHF**, and ten for **GHSD**. It comes out that the use of the **CIT** and **CVHF** methods can be handled more easily than the other one. Nevertheless, from a thermal point of view, the **CIT** has some limitations in accurately describing the thermal profile during welding. A transitory is necessary before the simulated temperature profile matches the real temperature profile, as described later in Section 3.2.1. In addition, the activation of elements at a fixed temperature does not allow for the study of a moving, tilted heat source [111]. Methods like **CIT** and

CVHF are usually based on tuneable parameters, which are necessary for the correct setting of the heat source [112].

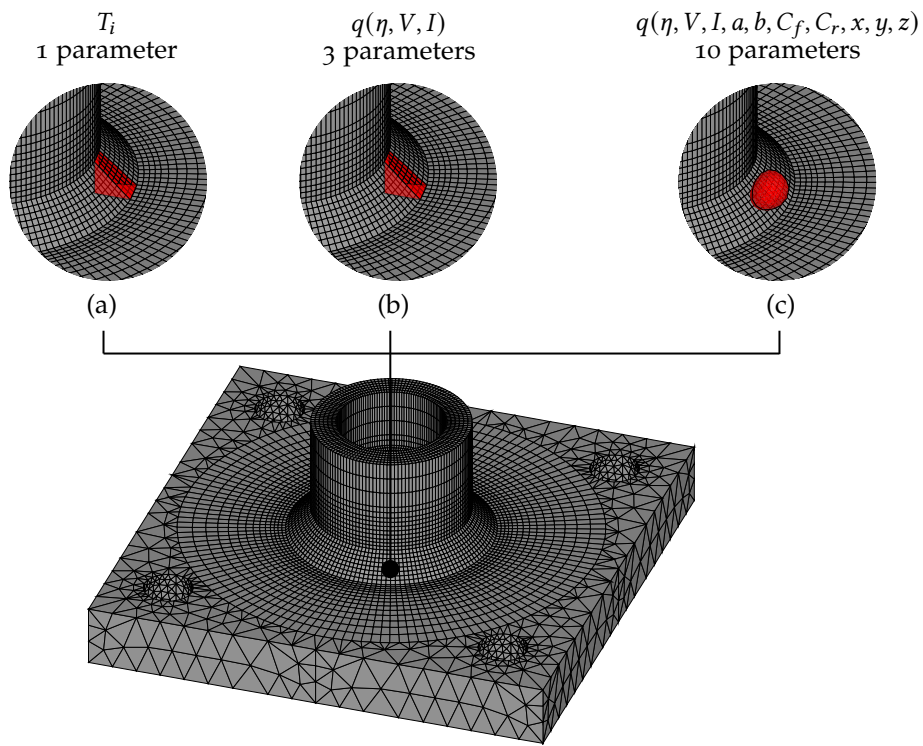


Figure 9: Meshed specimen (bottom) and simulation techniques applied on the welding seam: constant initial temperature (a), constant heat flux (b), and Goldak's double-ellipsoid model (c)

### 3.2.1 Constant Initial Temperature

The first method consisted of a sequential activation of elements with the same temperature; to do this, an *element birth and death* technique was applied. The procedure, which is now implemented in all of the most modern FEM software, deactivates the elements by multiplying their conductivity (or stiffness depending on the simulation type) for a severe reduction factor; as soon as the element is reactivated, the key quantities return to their full original values. The elements to which the CIT is applied were chosen according to the real geometry of the weld seam, as shown in Figure 10. After their activation, the elements exchange heat with the surrounding material; the transient temperature field ( $T$ ), function of time ( $t$ ), follows the equilibrium Equation (12). It is worth noting that the use of the *element birth and death* technique approximates the welding process in a discrete way, by activating only a finite set of elements. In this case,  $Q_{int} = 0$  because only the initial temperature condition was set. Another example of the application of this technique can be found in [45]. The application of this method is immediate and easy, even for complex joint geometry; actually, only the elements selection is needed and just one parameter has to be set. Nonetheless, the real complex process of material deposition with phase transition (e.g., [113]) is not simulated, and, therefore, the temperature that has to be settled on has to be considered as a fictitious parameter that has no real basis.

It is worth noting that, although the CIT method may appear approximate compared to other methods (i.e. Goldak double ellipsoid, Gaussian heat flux, constant heat flux), it is designed to resemble what occurs during arc-based welding processes involving filler material. In processes with added filler material, at a certain process time  $t_i$ , molten and base materials come into contact. On the contrary, in processes such as additive manufacturing or beam-based welding processes, base material is directly melted. Therefore, in such cases, thermal profile better resembles the one described by models such as Goldak double ellipsoid or Gaussian heat flux.

In terms of numerical performances, the implementation of the CIT model required 1069 s of elapsed

time, spent for computing the solution on a workstation endowed with four physical cores running in parallel and 16 GB of RAM available.

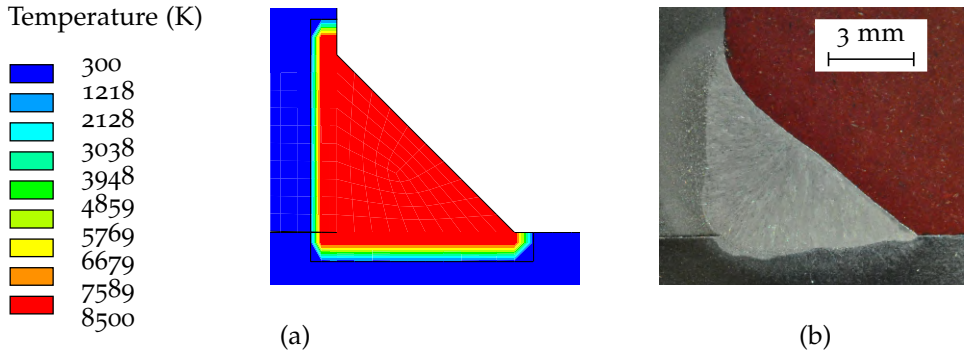


Figure 10: Activated elements for the CIT model with a temperature of  $T_i$  (a) cross section of the weld seam (b)

### 3.2.2 Constant Volumetric Heat Flux

The volumetric heat flux consists of a constant uniform heat distribution that follows Equation (13):

$$q_{vol} = c_c \frac{\eta UI}{V}, \quad (13)$$

where  $q_{vol}$  ( $\text{W m}^{-3}$ ) is the volumetric heat flux,  $U$  (V) is the welding voltage,  $I$  (A) is the current,  $\eta$  is the efficiency of the welding process, and  $V$  ( $\text{m}^3$ ) is the volume to which the flux is applied. The used parameters are given in Table 6. Additionally, in this case, the factor  $c_c$  has no physical interpretation, but its purpose is to fine-tune the volumetric heat flux to reach the desired temperature as observed in the experimental test.

The heat flux was activated sequentially on a set of elements belonging to the welding seam through the *element birth and death* technique. Again, the simulation has a discrete nature due to the activation of specific set of elements. With reference to Equation (12), the internal heat source is given by  $Q_{int} = \eta UI$ . Different authors already applied this technique (see e.g., [19] and [114]). In terms of numerical performances, the implementation of the CVHF model required 1021 s of elapsed time, spent for computing the solution on a workstation endowed with four physical cores running in parallel and 16 GB of RAM available.

### 3.2.3 Goldak's Heat Source Distribution

The double-ellipsoid heat source proposed by Goldak is based on the following set of equations:

$$Q_s = \eta UI \quad (14)$$

$$q_f(x, y, z) = \frac{6\sqrt{3}f_f Q_s}{abC_f \pi \sqrt{\pi}} e^{-(\frac{3x^2}{C_f^2} + \frac{3y^2}{a^2} + \frac{3z^2}{b^2})} \quad (15)$$

$$q_r(x, y, z) = \frac{6\sqrt{3}f_r Q_s}{abC_r \pi \sqrt{\pi}} e^{-(\frac{3x^2}{C_r^2} + \frac{3y^2}{a^2} + \frac{3z^2}{b^2})} \quad (16)$$

$$f_f + f_r = 2 \quad (17)$$

$$f_f = \frac{2}{1 + \frac{C_r}{C_f}}, f_r = \frac{2}{1 + \frac{C_f}{C_r}} \quad (18)$$

where  $Q_s$  (W) is the heat distribution of the welding heat source,  $U$  (V) is the welding voltage and  $I$  (A) is the current of the welding process, while  $\eta$  is the efficiency of the process. In Equations (15) and (16),  $q_f$  and  $q_r$  ( $\text{W m}^{-3}$ ) are, respectively, the front and rear ellipsoidal heat distribution amount at point  $(x, y, z)$ , while  $a$ ,  $b$ ,  $C_f$  and  $C_r$  are geometrical parameters of the ellipse. The geometrical parameters were collected directly from the fusion zone, as shown in Figures 11 and 12; in this way,

the ellipsoid geometry is experimentally described, as was already done by [115]. Finally, the terms  $f_f$  and  $f_r$  are the strength distributions of the ellipsoid.

For the application of the Goldak model, it is necessary to define a coordinate system, which, for instance, has to keep track of the welding torch movement; in this way, the Goldak distribution can replicate the real heat distribution without using the *element birth and death* technique. For the analyzed case, the coordinate system required for this particular joint geometry is represented in Figure 11, while Matrices 19 and 20 define it mathematically.

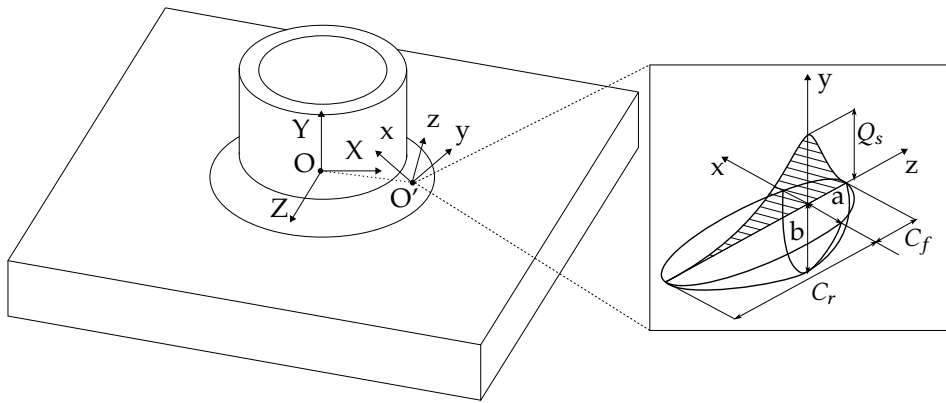


Figure 11: Coordinate system transformation between global and local reference frame, for Goldak's double-ellipsoid model

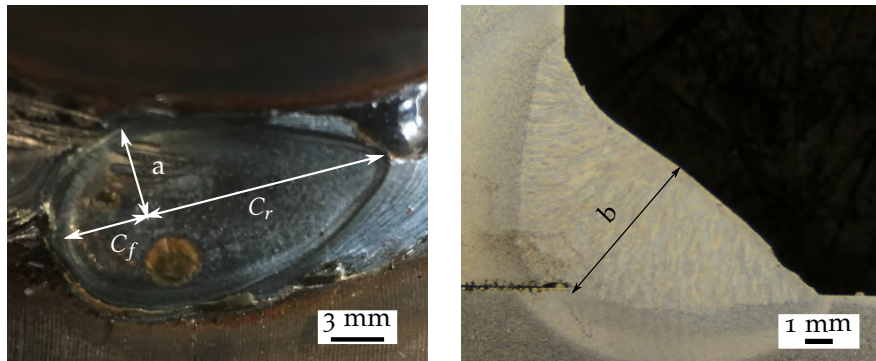


Figure 12: Goldak's heat source parameters estimated directly by examining the fusion zone

The two systems ( $X, Y, Z$ ) and ( $x, y, z$ ) of Figure 11 can be linked by the homogeneous transformation matrix written in the global reference system:

$$T = \begin{bmatrix} R_{11} & R_{12} & R_{13} & d_x \\ R_{21} & R_{22} & R_{23} & d_y \\ R_{31} & R_{32} & R_{33} & d_z \\ 0 & 0 & 0 & 1 \end{bmatrix} = \begin{bmatrix} -\frac{\sqrt{2}\cos(\omega t)}{2} & \frac{\sqrt{2}\cos(\omega t)}{2} & -\sin(\omega t) & \cos(\omega t)(\frac{D_T}{2} + \frac{L_S}{2}) \\ \frac{\sqrt{2}}{2} & \frac{\sqrt{2}}{2} & 0 & \frac{L_S}{2} \\ \frac{\sqrt{2}\sin(\omega t)}{2} & -\frac{\sqrt{2}\sin(\omega t)}{2} & -\cos(\omega t) & -\sin(\omega t)(\frac{D_T}{2} + \frac{L_S}{2}) \\ 0 & 0 & 0 & 1 \end{bmatrix} \quad (19)$$

In Matrix (19),  $t$  is the welding time,  $\omega$  is the angular rotation speed of the welding torch with respect to the  $Y$  axes, and  $D_T$  and  $L_S$  are geometrical parameters, representing the external tube diameter and welding width (whose magnitude is given in Figure 7), respectively.

With reference to Figure 11, in the software Ansys, a reference system rotation  $ZXY (\phi, \psi, \alpha)$  has to be defined in local axes (i.e., Matrix (20)), together with a translation with respect to the global reference system (translation array  $(d_x, d_y, d_z)$  of Matrix (19)):

$$R = \begin{bmatrix} \cos(\alpha)\cos(\phi) - \sin(\psi)\sin(\alpha)\sin(\phi) & -\cos(\psi)\sin(\phi) & \cos(\phi)\sin(\alpha) + \cos(\alpha)\sin(\psi)\sin(\phi) \\ \cos(\alpha)\sin(\phi) + \cos(\phi)\sin(\psi)\sin(\alpha) & \cos(\psi)\cos(\phi) & \sin(\alpha)\sin(\phi) - \cos(\alpha)\cos(\phi)\sin(\psi) \\ -\cos(\psi)\sin(\alpha) & \sin(\psi) & \cos(\psi)\cos(\alpha) \end{bmatrix} \quad (20)$$

The required angles of rotation are therefore those shown in Equations (21, 22, 23):

$$\phi = \arctan2(-R_{12}, R_{22}), \quad (21)$$

$$\psi = \arctan2(R_{32}, \sqrt{R_{31}^2 + R_{33}^2}), \quad (22)$$

$$\alpha = \arctan2(-R_{31}, R_{33}). \quad (23)$$

Table 6: Numerical input parameters employed during the calibration of the models.

Global Input Parameters			
Arc Efficiency ( $\eta$ )	Arc Voltage ( $U$ )	Welding Current ( $I$ )	Heat Source Volume ( $V$ )
0.75	25 V	211 A	$1.155 \times 10^{-7} m^3$
<b>GHSD input parameters</b>			
$a$	$b$	$C_f$	$C_r$
$5.2 \times 10^{-3} m$	$6.2 \times 10^{-3} m$	$4.9 \times 10^{-3} m$	$14.4 \times 10^{-3} m$
Parameters fine-tuned with GHSD model as reference			
<b>CVHF input parameters</b>		<b>CIT input parameters</b>	
$c_c$		$T_i$	
36		7900 K	
Parameters fine-tuned with experimental results as reference			
$c_c$		$T_i$	
40		8500 K	

In terms of numerical performances, the implementation of the GHSD model required 2036 s of elapsed time, spent for computing the solution on a workstation endowed with four physical cores running in parallel and 16 GB of RAM available.

### 3.2.4 Weld Pool Shape

All three models were validated by comparing the molten pool cross section between the real specimen and simulation results. The reference melting temperature of the material is 1773 K.

Figures 13 and 14 show the thermal solutions derived from the implemented Goldak and heat flux models, respectively. In particular, Figures 13a and 14a represent the thermal gradient in the weld seam surroundings, in which the melted areas are coloured in grey. It is worth noting that, in the case of CVHF of Figure 14a, the dashed line marks the division between the deactivated elements on the right and the molten area on the left. In addition, Figures 13b and 14b are cross sections, in which the weld pool penetration is displayed. Comparing the sub-figures (b) and (c), it can be seen that both models closely approximate the real geometry of the melt pool.

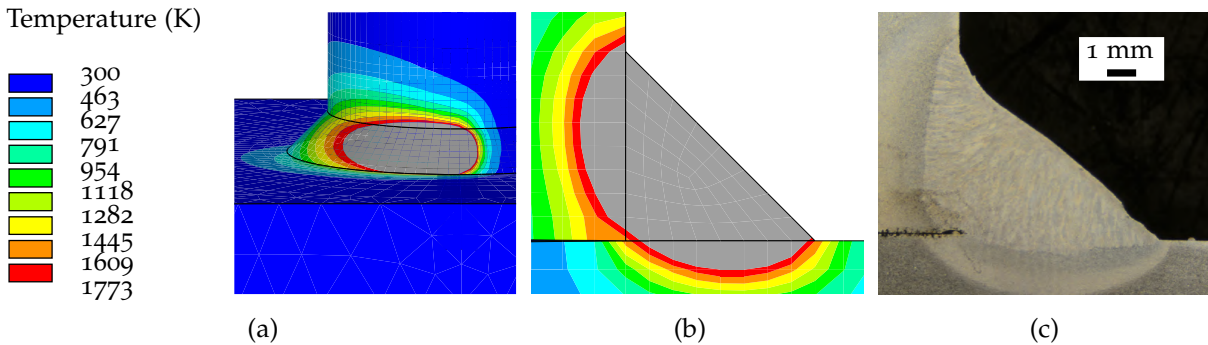


Figure 13: Goldak's double-ellipsoid model: overview of the thermal solution (a), finite element model cross section of the weld seam (b), real cross section of the weld seam (c)

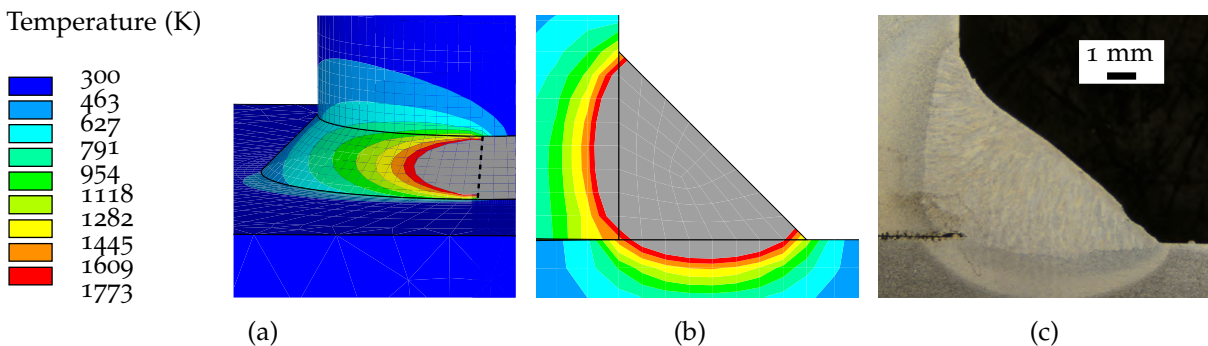


Figure 14: Heat flux model: overview of the thermal solution (a), finite element model cross section of the weld seam (b), and real cross section of the weld seam (c)

On the other hand, it could be expected that the [CIT](#) method, being an extremely simplified model, would not provide an accurate description of the the temperature distribution. For instance, a comparison between the [CIT](#) method and the weld pool geometry is shown in Figure 15. Clearly, the very physics of the [CIT](#) model make it impossible to correctly represent the weld pool geometry at the element activation time illustrated in Figure 10. Nonetheless, the geometry of the melted zone is well represented after a few tenths of a second after the element activation, Figure 15b. As for the [GHSD](#) and [CVHF](#), and even for the [CIT](#) method, the characteristic temperature distribution, the stretched-left shape of the melt area, could be detected. This typical shape is due to the different cooling rates caused by the different pipe and plate thicknesses. This effect is also highlighted in the micrography of Figure 15c. In addition, the same distinction made for [CVHF](#) between the molten zone and deactivated elements is also shown here by a dashed line.

The comparison between the methods reasonably shows that the [CIT](#) method can be meaningfully applied even for a subsequent mechanical simulation.

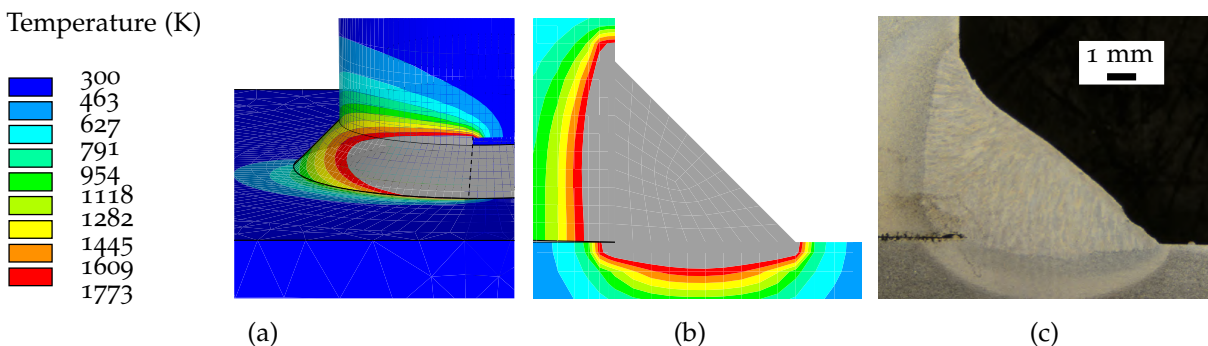


Figure 15: Constant initial temperature: overview of the thermal solution (a), finite element model cross section of the weld seam (b), and real cross section of the weld seam (c)

### 3.2.5 Experimental Set-up

The results of the numerical simulations were discussed and verified through experimental activity. Temperature over time was measured in different points of the plate surface by thermocouples, as shown in Figure 16. For practical experimental reasons, a simplified specimen geometry was selected instead of a real one, in order to measure the temperature over time distribution. The simplified geometry was required because the welding process of the original specimen does not allow for easy positioning of the thermocouples, as already described in Section 3.1. In this case, the welding process took place by keeping the sample still, with the subsequent movement of the welding torch. As in the case of the real test specimen, the welding process was also steady, except for a starting and for an ending transient phase. The experimental procedure was set up in order to use the same weld speed as in the real pipe-to-plate specimen. The specimen geometry shown in Figure 17 was selected, in which the main parameters that influence the thermal behavior, i.e., material, plates and wall thickness, were kept the same as in the pipe-to-plate specimen object of this study.

Eight thermocouples of K type (Nickel/Chrome–Nickel/Aluminium) with a maximum detectable temperature of  $1473\text{ K}$  and a diameter of  $1\text{ mm}$  were placed at different distances from the weld seam in order to compare the numerical and experimental results at different positions, as summarized in Table 7. The temperature readings were taken simultaneously through a data logger Pico TC-08, operating at a frequency of  $1\text{ Hz}$ , with cold junction compensation.

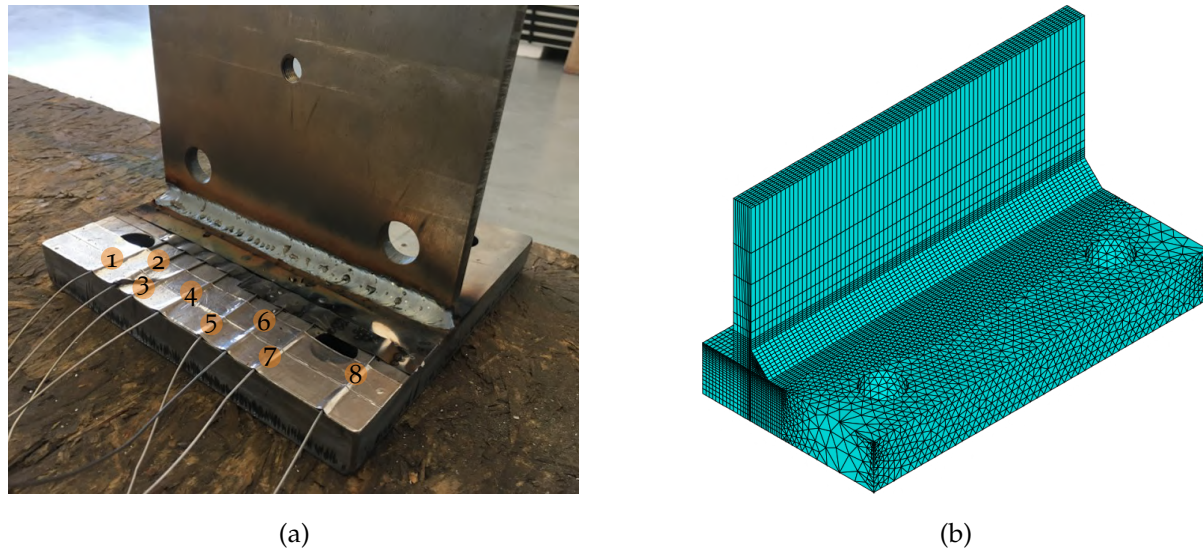


Figure 16: Experimental set-up for temperature measurement (a) and FE-model (b) of the simplified specimen

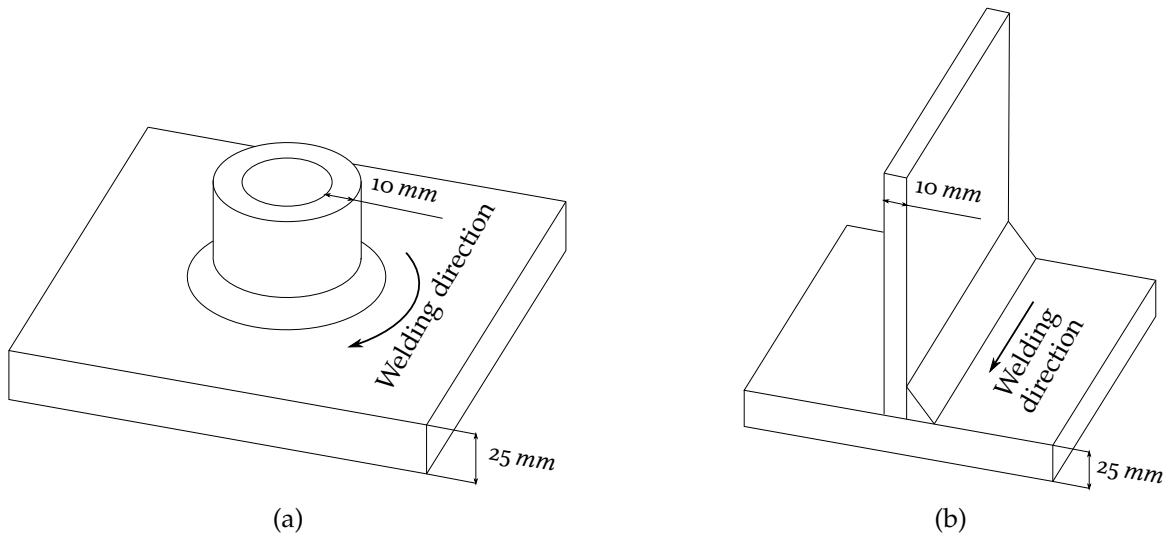


Figure 17: Real specimen's geometry (a), simplified specimen's geometry (b)

Table 7: Thermocouples' distance from the welding seam:  $d$  = distance,  $N^\circ$  = thermocouple's number

$N^\circ$	$d$	$N^\circ$	$d$	$N^\circ$	$d$	$N^\circ$	$d$
TC-1	8 mm	TC-2	10 mm	TC-3	12 mm	TC-4	14 mm
$N^\circ$	$d$	$N^\circ$	$d$	$N^\circ$	$d$	$N^\circ$	$d$
TC-5	10 mm	TC-6	13 mm	TC-7	16 mm	TC-8	19 mm

### 3.3 RESULTS AND DISCUSSION

#### 3.3.1 Preliminary sensitivity analysis

A sensitivity analysis was performed to evaluate the influence of different input parameters on the temperature distribution over time. As an example, the temperature–time history on the plate surface for the point at 3 mm from the weld toe is discussed in the following. A study was carried out on the parameters described below:

- Thermal Conductivity,  $k$  ( $W m^{-1} K^{-1}$ );
- Heat Capacity,  $c$  ( $J kg^{-1} K^{-1}$ );
- Convection,  $h$  ( $W m^{-2} K^{-1}$ );
- Emissivity,  $\epsilon$ .

Concerning thermal conductivity, heat capacity, convection and emissivity, the results are shown in Figure 18. For these quantities, a variation of  $\pm 30\%$  had been taken as a reference since it turned out to be the maximum difference found by comparing different literature sources: [108], [116], and [117]. The maximum temperature measured in the cooling curve of Figure 19 was chosen as the benchmark to assess the influence of the parameter under consideration. The error was defined as shown in Equation (24):

$$Err\% = 100 \frac{T_{Max\_Reference} - T_{Max\_Variation}}{T_{Max\_Reference}}, \quad (24)$$

where  $T_{Max\_Reference}$  is the maximum temperature calculated for the reference curve, while  $T_{Max\_Variation}$  is the maximum temperature calculated on the input variate curve. Approximatively, the maximum

temperatures are the ones highlighted from the dashed line in Figure 19; the image reports an example of how the cooling behaviour changes with a variation in thermal conductivity. As can be seen from Figure 18, only thermal conductivity and thermal capacity has a significant influence on the results. For these input parameters, a variation of 30% can produce an output variation (i.e. maximum temperature) up to 5%, while the influence of the other input parameters result negligible in this range.

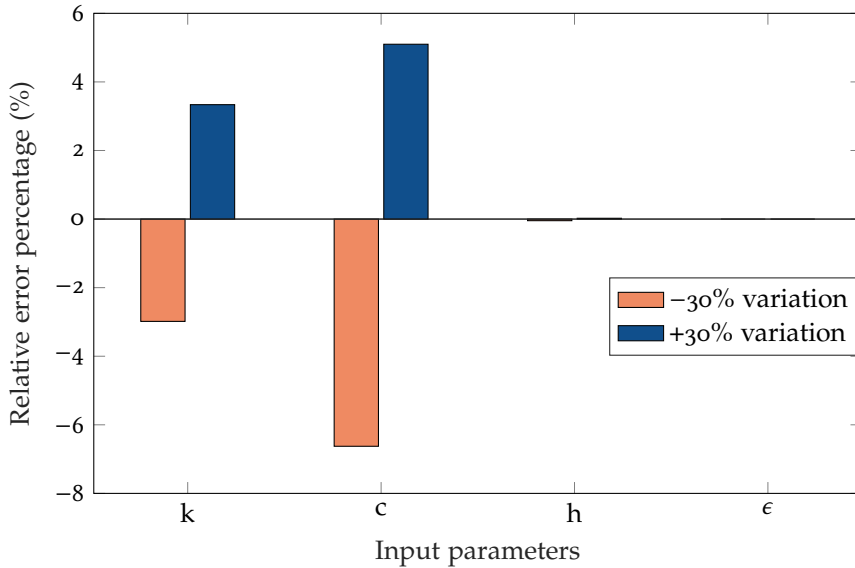


Figure 18: Relative error percentage with respect to the maximum temperature of the reference curve

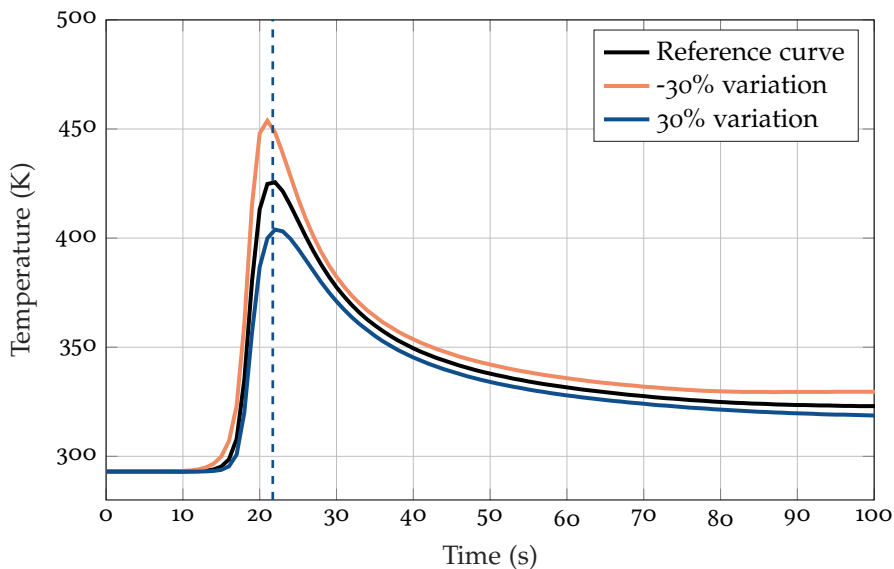


Figure 19: Behaviour of the curve temperature vs. time at a distance of 3 mm from the weld toe, for a  $\pm 30\%$  modification of thermal conductivity

### 3.3.2 Results

#### 3.3.2.1 Numerical Results

First of all, a comparison was done between the three numerical models, as explained in Section 3.2. The comparison is reported in Figure 20; the Goldak's double-ellipsoid result (continuous lines in Figure 20) was taken as the reference curve, while the temperature over time was measured in three points

on the surface of the plate.

The legend in Figure 20 refers to three points on the plate surface with the following distance from the weld toe: 3 mm for the point 1, 6 mm for the point 2, and 10 mm for the point 3.

Starting from the Goldak's numerical solution, the other methods were tuned in order to qualitatively have the same thermal behavior. The parameters that were changed were the initial temperature  $T_i$  for the CIT and the parameter  $c_c$  for the CVHF method. In particular, the setting parameters were varied in an attempt to reproduce the maximum temperature at point 1,  $T_i = 7900 K$  and  $c_c = 36$  were obtained. Figure 20 shows that, near the weld seam, the same thermal behavior can be achieved with all the implemented methods. Some subtle difference can be observed inside the weld seam as already discussed in Section 3.2.4. For instance, with reference to the CIT method, it is assumed that the total heat input derives from the molten metal droplets, whereas other heat sources also play an important role (e.g., the electric arc of plasma has a temperature range from 3000 K to 20 000 K, as reported in [118] and [119]); this leads to the slightly higher initial temperature that has to be set. Similar considerations apply to the CVHF, where only a few parameters were taken into account compared to GHSD. Obviously, it is complicated to consider all the parameters that can influence the thermal behaviour during a welding process; these numerical models can only consider some of them. An interesting example is given by the diverse heat source distribution caused by a different shielding gas composition, as illustrated by [120].

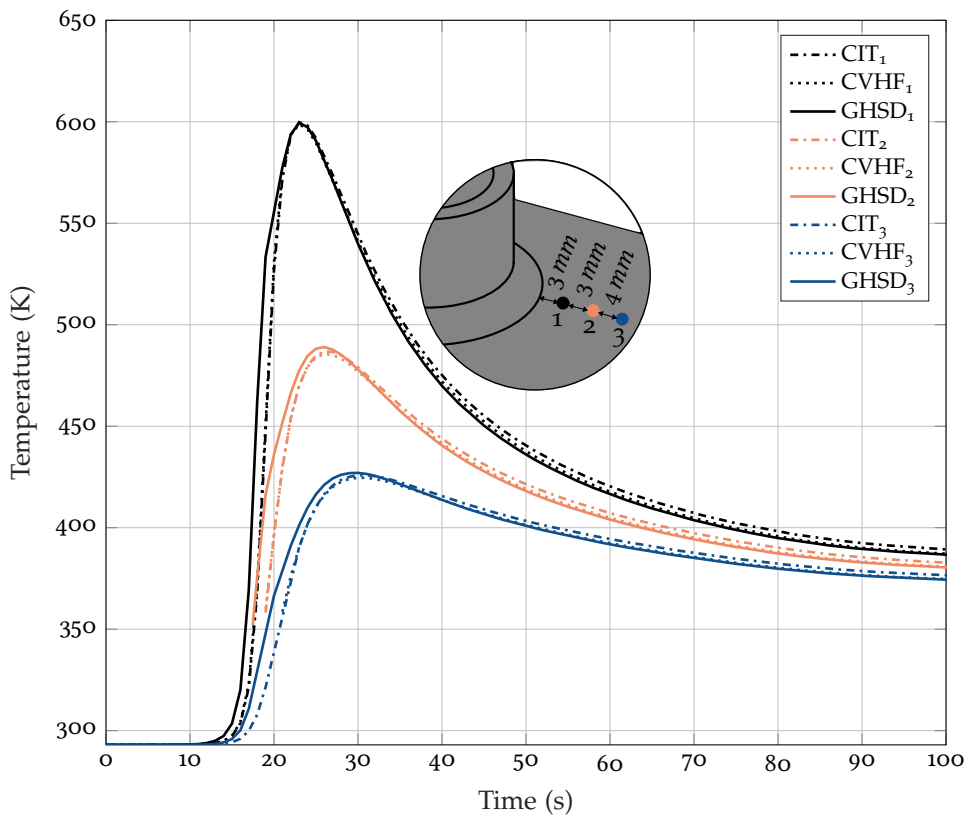


Figure 20: Temperature vs. Time curve of the thermal models employed, specifically for three points on the surface of the plate

### 3.3.3 Comparison with Experimental Temperature Measurements

The CIT method was then used in an attempt to reproduce the experimental temperature measurements. The initial temperature was varied until a value of  $T_i = 8500 K$ , while the number of elements to be activated was determined by the deposition velocity of the weld material. With reference to Figure 21, the calibration on the CIT method with respect to experimental measurements was performed at the point closest to the weld seam (i.e., point 1 at 9 mm). Figure 21 shows the experimental curves in a continuous line and those resulting from the simulation are shown as a dashed line.

A fairly good agreement was observed between the experimental and simulated temperature; the observed maximum difference in temperature during the cooling phase is less than 50 K. With reference to the heating-up phase, the measurements show the typical wave-form of manual welding; for this reason, greater temperature differences were sometimes obtained. However, the temperature gradient during the first phase was captured fairly well for all the curves.

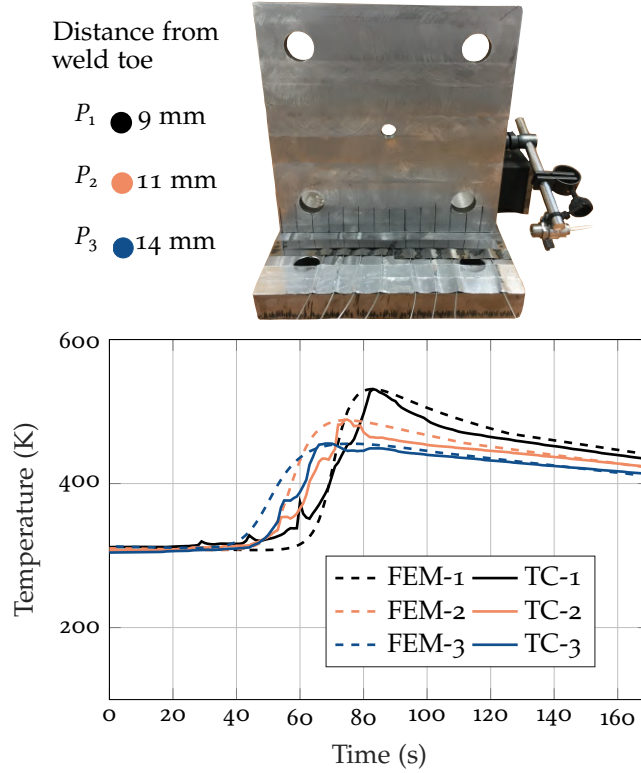


Figure 21: Comparison between experimental and numerical results of temperature over time

#### 3.4 CONCLUSION

The simplified CIT thermal model proved to be able to represent fairly well the temperature profile due to a welding process. By comparing the studied numerical models negligible differences were found between their temperature profiles (i.e. after that all models were set based on the Goldak's double ellipsoid heat source). In addition, comparing the CIT model with experimental data it was found that, although the CIT is a simplified model, can significantly describe the actual temperature profile. The CIT model will be employed in the next chapters as thermal heat source for simulating a welding process. The model parameter  $T_i$  was set with comparison with experimental temperature results deriving from an equivalent specimen geometry.



# 4

## EVALUATION OF RESIDUAL STRESSES

Once the CIT heat source had been investigated in chapter 3, the aim was to implement it for a structural simulation as well. In this case, the comparison between experimental and numerical results was carried out on relaxed strains measurements made by incremental cutting the base plate of the pipe-to-plate welded joint.

In the following, the experimental campaign that led to the calculation of relaxed strains quantities will be firstly introduced, and subsequently the structural numerical model for the calculation of residual stresses and strains will be discussed.

### 4.1 INCREMENTAL HOLE DRILLING ANALYSIS

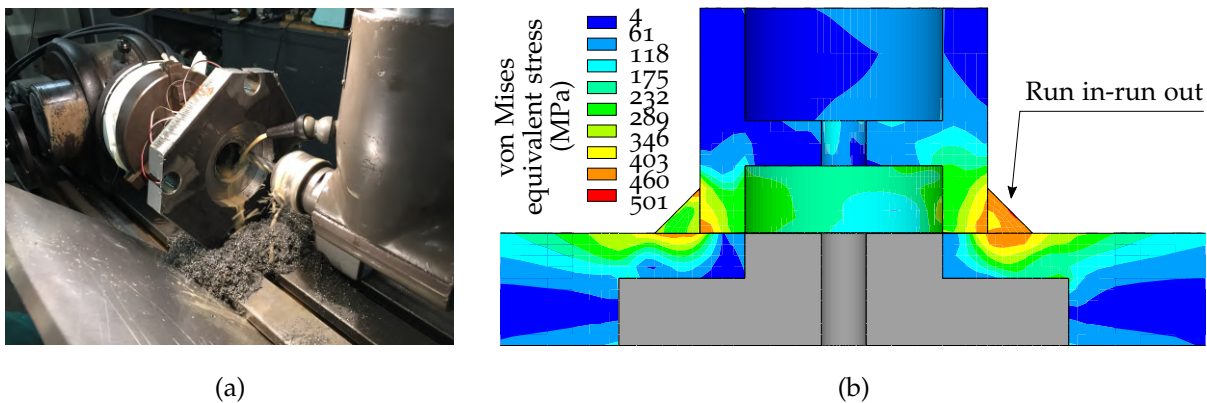


Figure 22: Experimental machining of the bottom part of the specimen plate (a), numerical simulation of the incremental cutting process (b)

An incremental cutting procedure was performed on the bottom of the plate in order to acquire a series of experimental relaxed strains, representative of the residual stress state in the welded region (i.e. Figure 22a). The process involved drilling the base of the plate, slowly increasing diameter and depth dimension of the hole. Two holes of different diameters and depths were machined. The first is a through hole of 42 mm in diameter while the second is an incremental hole, 100 mm in diameter and total depth of 20 mm; this procedure is schematised in a simplified way in Figure 23.

The experimental procedure was then reproduced by a numerical simulation in order to validate the overall numerical analysis described before (i.e. Figure 22b). A similar strategy of element deactivation has been implemented by Salerno et al. [121], applied for material removal preceding a repair welding process. However, the removed material volume made by Salerno was negligible compared to the overall volume of the component, leading to a negligible difference within the residual stress distribution caused by the original joining process. On the contrary, in our study the interest lies in obtaining a significant difference in the residual stress state between the drilled and non-drilled component in order to allow strain gauges to operate well beyond their background noise, albeit within their maximum tolerance.

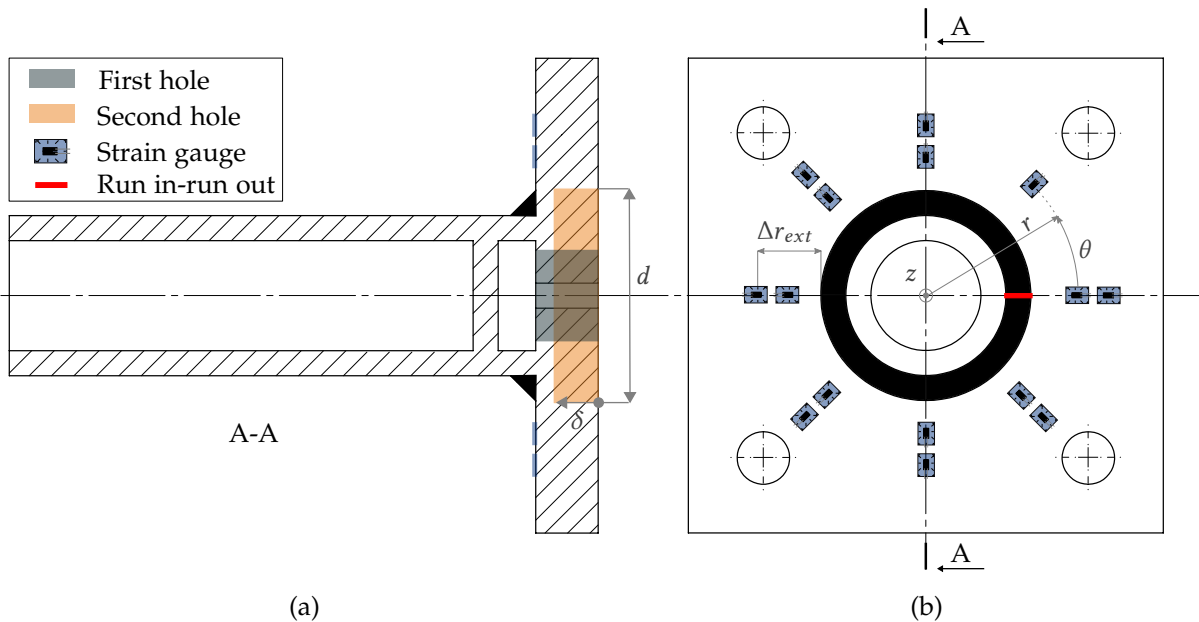


Figure 23: Incremental hole drilling process used to detect relaxed strains (a) and qualitative layout of the strain gauges (b)

The step-based cutting process was implemented to control the acquired result and be confident about the reading of the strain gauges.

#### 4.2 FINITE ELEMENT ANALYSIS

Uncoupled thermal-structural simulations were performed by using the software Ansys vers. 19.2. An uncoupled simulation was adopted to limit the computational effort, given the complex nature of the investigated process. The thermal problem was firstly solved (i.e. [chapter 3](#)) and then the results, in terms of nodal temperatures, were used in the structural analysis as thermal loads. The analysis is transient and capable of describing how the temperature history affects the structural results, mainly, through the use of temperature-dependent material properties.

In general, the simulation is divided into three steps, to be sequentially solved, in order to reproduce the entire<sup>4</sup> process: thermal analysis, structural analysis and incremental hole drilling analysis. Each step, with exception of the thermal analysis, will be described in more details in the following.

A fully three-dimensional model was adopted since the thermal load during the welding process cannot be considered axisymmetric. Stresses and strains produced through the welding process ultimately depend on the hoop coordinate [2], because heat is transferred gradually along the angular direction and this results in a non uniform deformation of the component. In [Appendix A](#), a residual stresses investigation regarding two-dimensional and three-dimensional models have been reported and compared together with the difference in employing linear-elastic or elastic-plastic material properties.

##### 4.2.1 Structural analysis

After the thermal analysis the welding process was then structurally reproduced. The load, obtained as a time-temperature binary data file resulting from the thermal simulation, was applied to the nodes of the FE-model. In this stage, the structural stresses and strains over time are computed starting from the temperature evolution. The structural problem is, actually, time-dependent and, as explained in [39], the cause is mainly due to the material plasticity, time-history of the thermal load and the time-varying FE-domain.

However, since the distortions that are obtained during the entire welding process are not significant

<sup>4</sup> The whole process is constituted by welding the tube to the top surface of the plate and then incrementally drilling a hole from the bottom surface of the plate, in order to get the relaxed strains.

enough to affect the overall initial temperature profile, the adopted procedure is assumed as appropriate. Nevertheless, due to the low yield stress of the material at high temperature, a significant mesh distortion may cause a bad numerical convergence of the solution. To overcome this issue, re-meshing operations or gradual application of the thermal load (e.g. by increasing the number of substeps for the solution phase) can be alternatively used. In this case, the number of substeps was incremented until a satisfactory solution was achieved.

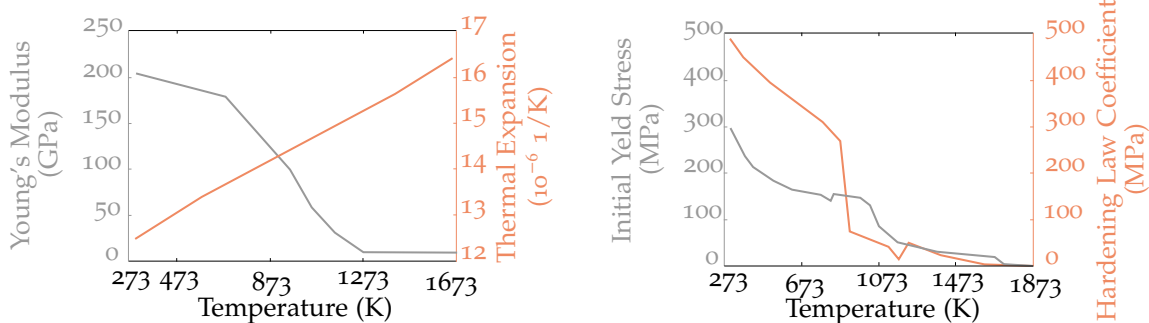


Figure 24: Temperature dependant structural material properties of S355 steel acquired from [108]

Temperature dependent material properties for the structural analysis were derived from [108] and are presented in Figure 24. The linear elastic stress-strain model is described through a temperature dependent Young's modulus ( $E$ ) and a constant Poisson's ratio ( $\nu = 0.3$ ). Instead, the elastic-plastic stress-strain relationship follows Equation 25

$$\sigma = \sigma_y + H(\varepsilon_p)^N \quad (25)$$

where  $\sigma$  is the total stress,  $\sigma_y$  is the yield stress,  $H$  is the hardening law coefficient,  $\varepsilon_p$  is the plastic strain and  $N$  is the hardening exponent that in this case was assumed as constant ( $N = 0.25$ ). A satisfactory convergence of the numerical stress/strain results was obtained implementing the material properties of Figure 24 up to a maximum temperature of 1273 K. A reasonable explanation for this, is that negligible changes in the material stiffness take place beyond a given (high) temperature. For temperatures higher than 1273 K, material properties like the Young's modulus and initial yield stress are almost negligible, meaning that the material above that temperature cannot bring a significant contribution in terms of stiffness.

The same mesh grid of Figure 9 was applied for both thermal and structural analyses, to correctly implement the thermal load in the right nodal position. Elements were updated, from thermal to mechanical element type; the eight-node SOLID185 element was used, with three degrees of freedom (the displacements in x, y and z directions) at each node. As boundary conditions, displacements of nodes on the upper surface of the tube (far away from the weld) were constrained. Although this did not reflect the real bound used during the welding process, it allows the specimen to freely deform as it happens during the real process. Any edge effect caused by the imposed constraint did not affect the stress and strain fields in proximity of the weld seam (it may alter the solution nearby a cylindrical area defined by the shell characteristic lengths<sup>5</sup>).

Similarly to the thermal simulation, also in the structural analysis the *element birth & death* method was implemented to better reproduce the component behavior during the welding process.

Two methods were employed, i.e. the *classic approach* and a **RWP** in the following. According to the *classic approach* all elements belonging to a section of the molten bead are sequentially activated for the structural analysis, independently from their temperature at that given time. With the **RWP** method, the elements having a temperature higher than the melting point ( $T_m=1760\text{ K}$ ) are deactivated, while elements whose temperature drop below the melting point are reactivated, as reported by [122]). The melting point can be defined as the temperature for isothermal solidification or the liquidus or solidus temperature otherwise (given the inherent assumptions of a finite element problem, there is a negli-

<sup>5</sup>  $I_c = \frac{\sqrt{R}h}{\sqrt[4]{3(1-\nu^2)}} = 13.65\text{ mm}$ , where  $R = 27\text{ mm}$  is the mean tube radius,  $h = 10\text{ mm}$  is the tube thickness and  $\nu = 0.3$  is the Poisson's ratio

gible difference in the choice of  $T_m$  for classic steel alloys, as long as it remains within the range described above).

Figure 47 schematically describes both the *classic* and the *RWP* methods applied to solve the structural problem, showing an example of weld bead cooling sequence after applying the *CIT* thermal model. Figure 47a and Figure 47b, give an overview of the active elements at a generic welding time  $t_i$ . If there is no correlation between activated elements and their temperature for the *classic* method, the same cannot be stated for the *RWP* method. As a matter of fact, from Figure 47c and Figure 47d, the difference in the cooling sequence between the two models can be identified. According to the *classic* method, elements are deactivated/activated solely based on the simulation time, whereas, according to the *RWP* method, the element activation is additionally related with the element temperature. In Figure 47d, it is possible to identify a sequential activation of the elements with temperature lower than the melting point. The result thus obtained represents what expected from the solidification of a pool of molten metal during the welding process. This process is repeated for every iteration of metal deposition, leading to a quite different structural result compared to the *classic* method. It can be observed, for instance, in Figure 47d, that a colder layer is created during the process, on the surface of the molten material, caused by the elevated thermal convection between the hot metal and the environment.

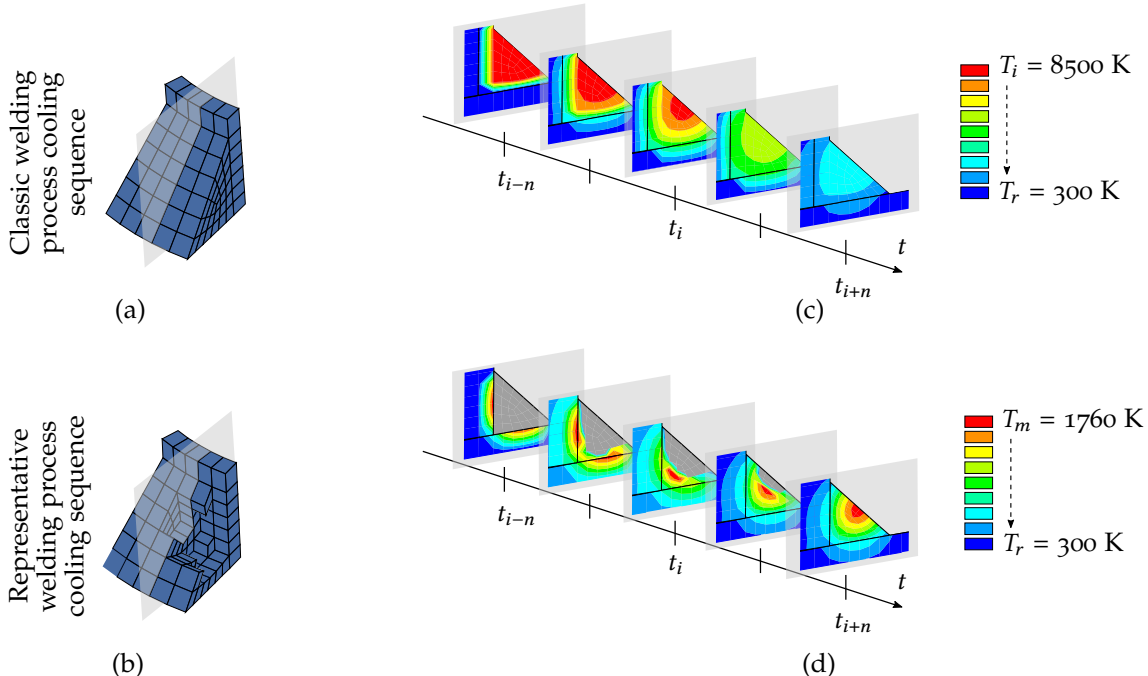


Figure 25: Weld seam volume segment for the *classic* (a) and *RWP* (b) methods; cooling sequence of a weld seam section during the structural simulation for the *classic* (c) and *RWP* (d) methods

A graphical flowchart of the code sequence used to implement the *RWP* is shown in Figure 26, with reference to the generic simulation time  $t_i$ . The process can be summarized as follows:

1. first of all elements belonging to the weld bead are selected, part of which are active while others remain inactive depending on the actual  $t_i$  time considered;
2. afterwards, only some of these elements are reselected, the position of which is a function of  $t_i$ ; to this regard, it is necessary to select a portion of weld seam elements circumferentially large enough to contain the entire interface area between molten and solidified material; this requirement is essential in order to activate all the elements in the right sequence and not leave some of them deactivated behind;
3. all the elements thus selected are activated for the purpose of updating the solidified material volume;

4. with regard to the molten material volume the update is done detecting all nodes with a thermal load (i.e. nodal temperature) greater than the melting point;
5. at this point, the elements attached to the selected nodes are chosen, being careful to select elements only if all their nodes are in the selected nodal set<sup>6</sup>;
6. the previously selected elements are then deactivated in order to obtain the correct melting pool shape;
7. finally, all the component elements are selected;
8. the whole model is solved at a time  $t_i$ ;
9. the simulation time is increased (i.e. from  $t_i$  to  $t_{i+1}$ ) and the next iteration is performed until the welding process is completed.

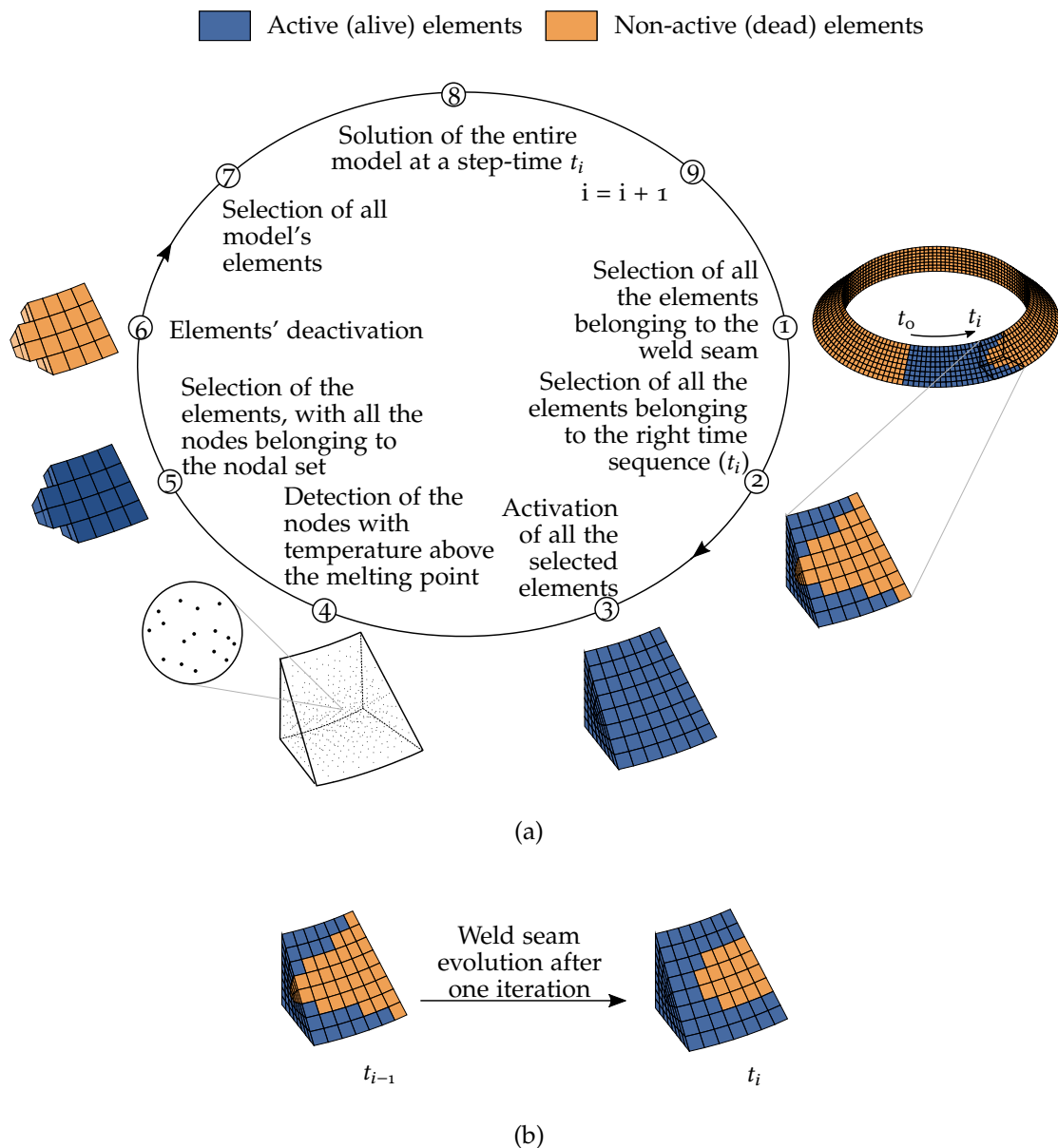


Figure 26: Graphic representation of the iterative process required to perform the RWP method (a), and example of active and inactive elements evolution in a weld seam section (b)

<sup>6</sup> This avoids selecting elements that are not completely melted.

The importance of using this formulation is related with the different stiffness that the specimen experiences during the process, which can lead to different residual stress fields at the end of the simulation. Furthermore, this method allows to set different *temperature at zero thermal strain* for the molten pool and base material, according to the following relationship used in Ansys software:

$$\varepsilon_{th} = \alpha(T - T_{ref}) \quad (26)$$

where  $\varepsilon_{th}$  represents the thermal strain,  $\alpha$  is the coefficient of thermal expansion,  $T$  is the instantaneous temperature of the element, while  $T_{ref}$  is the reference temperature at zero initial thermal strain; this temperature was set to 1760 K for the elements belonging to the weld seam and 300 K for all the others. The structural solution and especially the simulation of the molten metal deposition are highly dependent on the mesh size. However, while it is straightforward to achieve convergence for structural and thermal results (e.g. h-convergence method), the same outcome was not attainable with regard to the molten metal deposition process (RWP). The problem arose trying to simulate a continuous-based process (i.e. welding process), through a discrete model (i.e. CIT method). Unlike the methods based on thermal heat flux, the CIT model is mesh size dependent (i.e. the volume of material activated at temperature  $T_i$  varies depending on the number of selected elements). The benchmark for the convergence of both mesh size and the volume of activated elements during the thermal simulation was considered based on the convergence of both thermal and mechanical results. It was achieved with an average element dimension of approximately 1 mm in the proximity of the weld bead and the activation of elements contained in a volume defined by a 0.1 radiant arc of the weld seam (i.e. the weld seam segments of Figure 47a and Figure 47b).

#### 4.2.2 Incremental hole drilling numerical model

The incrementally cutting process was simulated by FEA through a sequential deactivation of some elements. No additional inputs were assigned to the numerical model, since the structural simulation results achieved in the previous step were used as initial conditions. The finite element model is kept unchanged compared to the structural simulation discussed above. It is worth noting that the FE-model requires an initial ad-hoc design in order to perform the hole drilling phase. Indeed, a component sub-volume partition is required, allowing a mesh generation that matches the holes diameter and depth, to be able to properly simulate the right material volume removal.

Another aspect to keep in mind is the correct location of the nodes in the right strain gauge reading positions. This is recommended to prevent the need to interpolate the solution between the nodes in the nearby positions. This technique allows the experimental determination of the relaxed strain in specific spots for direct comparison through strain gauges, as described below in section 4.3. The cutting process is easily reproduced numerically, throughout the *element birth & death* technique. The hole drilling process simulation provides a straightforward comparison of strains thus measured, both numerically and experimentally. The evaluation of the stress state is achieved directly via the FEA. In terms of numerical performances, the *classic* and RWP methods required similar simulation time of respectively 29 785 s and 32 639 s, with regard four physical cores running parallel and 16 GB of RAM available. The time spent in computing the solution was, in this case, considerably greater compared to the thermal simulations previously discussed in chapter 3.

### 4.3 RELAXED STRAIN EXPERIMENTAL MEASUREMENTS

Relaxed radial strain measurements were experimentally obtained in order to validate the numerical results derived from the simulation previously discussed. Strain gauges were placed at different radial ( $\Delta r_{ext}$ ) and angular ( $\theta$ ) coordinates to map the radial strain as a function of the two reference parameters i.e. the hole diameter ( $d$ ) and hole depth ( $\delta$ ). Figure 23 shows how both  $\Delta r_{ext}$  and  $\theta$  refer to the center of the positioning grid of strain gauges, which is required as numerical results consider this point when computing data from the FE-model.

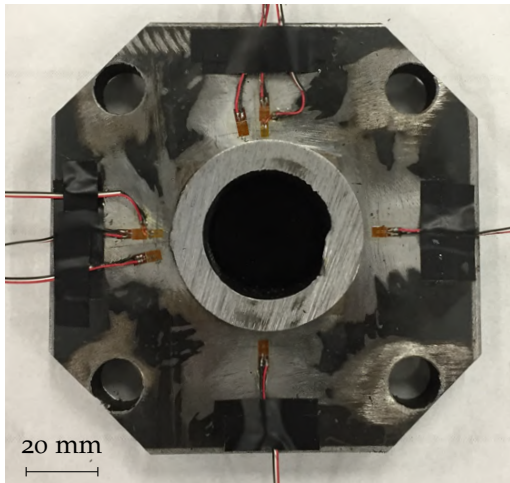
Linear strain gauges were employed with measuring grid length of 1.5 mm and 0.6 mm and with nominal resistance of 120 Ω (i.e. 1-LY1x-1.5/120 and 1-LY1x-0.6/120 from HBM), while the data acquisition system used was a *Model 5100B Scanner* from StrainSmart. Strain gauges with a grid length of 1.5 mm

were positioned at an angular step of  $\Delta\theta > 15^\circ$ , while strain gauges with a grid length of  $0.6 \text{ mm}$  were positioned at  $\Delta\theta = 6^\circ$  of angular step. Specifically, strain gauges with a grid length of  $0.6 \text{ mm}$  were used for localized strain measurements, located in the area opposite to the run in-run out point (start-end point of the single pass arc weld), to get an indication of the intrinsic variability of strain measurements, as explained later in section 4.4.2. Different strain gauge set-ups are shown in Table 8, where  $\Delta\theta$  is the angular step between strain gauges and  $\Delta r_{ext}$  is the distance between the strain gauge and the weld toe. Figure 27 shows two examples specimens set-up with  $1.5 \text{ mm}$  grid length strain gauge, specifically the *Test-1* and *Test-3* specimen of Table 8. Similarly, Figure 28 shows the *Test-4* specimen along with a view on the area where the  $0.6 \text{ mm}$  grid length strain gauges were applied together with a technical drawing to better understand their positioning. All the specimens were tested in as-welded condition.

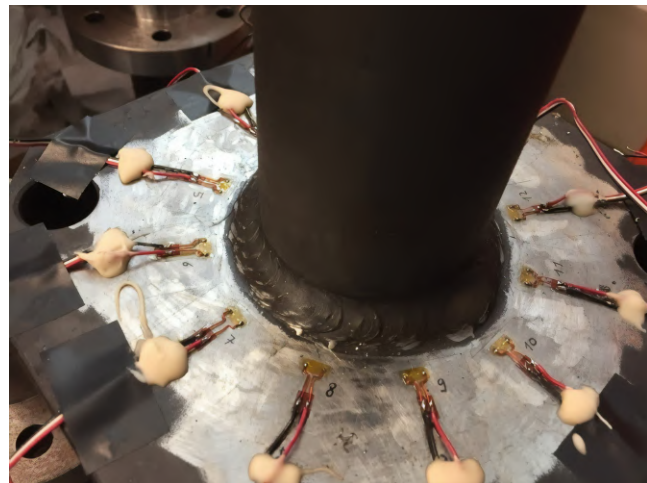
It should be noted that given the irregular geometry of the weld bead, strain gauges position with respect to the weld toe can be affected by an inherent error in radial direction. In addition, it is expected that strain gauges belonging to different specimens but placed in the same nominal angular and radial coordinate, will produce different experimental readings. For these reasons a certain variability in the experimental data is expected and it will be treated through a standard deviation estimated on the basis of the different performed measurements.

Table 8: Summary of experimental test set-up for relaxed radial strain measurements

Name	Strain gauges qty.	Grid length (mm)	$\Delta r_{ext}$ (mm)	$\Delta\theta$ ( $^\circ$ )
<i>Test-1</i>	8	1.5	6.5/9/13	90
<i>Test-2</i>	6	1.5	6.5/9/13	90
<i>Test-3</i>	12	1.5	6.5	30
<i>Test-4</i>	12	1.5/0.6	6.5	15/6



(a)



(b)

Figure 27: *Test-1* specimen, with eight strain gauges applied at a  $90^\circ$  step angle (a); *Test-3* specimen with twelve applied strain gages with  $30^\circ$  step angles (b)

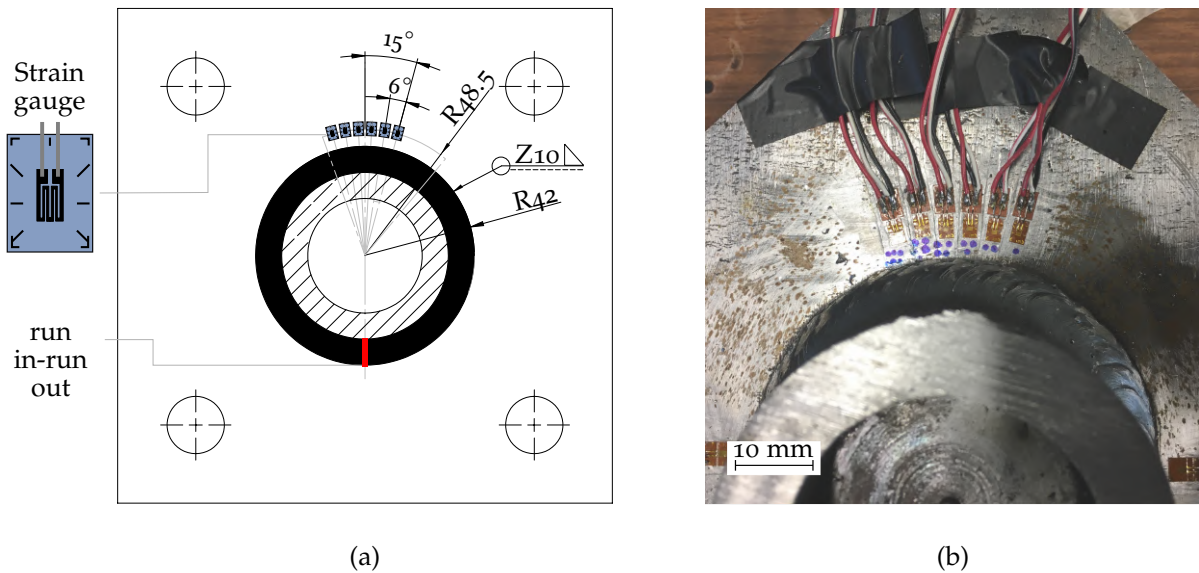


Figure 28: Technical drawing of the strain gauges positioning over a small arc of circumference (a), picture of the actual bead geometry at the point of application of the  $0.6\text{ mm}$  grid length strain gauges (b)

With reference to Figure 28a, the run in-run out point is identified by the location where the welding torch begins and ends the process. It is worth noting that the material under these circumstances is affected by a double thermal process, whereby residual stress and strain values can significantly deviate from an axisymmetric condition.

As described in section 5.1, the stress relaxation was performed by a progressive material removal from the back surface of the plate. Through material removal, relaxed strains have been progressively measured as a function of the radial distance ( $\Delta r_{ext}$ ), angular coordinate ( $\theta$ ), incremental hole depth coordinate ( $\delta$ ) and hole diameter ( $d$ ), as summarized in Equation 27

$$\varepsilon_{rr} = f(r, \theta, \delta, d) \quad (27)$$

As reported in Table 9 and Table 10, several measurements have been gathered from a single strain gauge, by maintaining  $\Delta r_{ext}$  and  $\theta$  fixed and varying  $\delta$  and  $d$ . For ease of comprehension, only the data obtained during the  $100\text{ mm}$  hole are reported since the readings obtained during the  $42\text{ mm}$  hole fall within the background noise. Table 9 summarizes relaxed radial strain measured through  $1.5\text{ mm}$  grid length strain gauges, while Table 10 summarizes relaxed radial strain measured through  $0.6\text{ mm}$  grid length strain gauges. In either cases, results have been reported as function of the strain gauge position (i.e. angular coordinate  $\theta$  and radial distance  $\Delta r_{ext}$ ) and the hole cutting depth  $\delta$ . Since the drilling was done by incremental steps of  $5\text{ mm}$ ,  $\delta$  gets discrete values of  $5\text{ mm}$ ,  $10\text{ mm}$ ,  $15\text{ mm}$  and  $20\text{ mm}$ . As can be noticed from both Table 9 and Table 10, an higher number of strain gauge readings were obtained in the vicinity of the weld toe (i.e.  $\Delta r_{ext} = 6.5\text{ mm}$ ), since residual radial stresses increase approaching the weld toe in radial direction. However, due to the steep gradient, the result variability obtained from the uneven weld bead geometry increases getting closer to the weld notch. For this reason, it is advisable not to rely on a single strain gauge reading and consider the variability in the results provided by more data, instead. This approach is adopted in the following section 4.4, where experimental and numerical results have been compared with regards to their mean values and standard deviations.

Table 9: Summary of experimental relaxed strains measurements in *italic* ( $\mu\epsilon$ ) for 1.5 mm grid length strain gauges and hole diameter  $d = 100$  mm

		Test-1						Test-2			
$\theta$ (°)	$\Delta r_{ext}$ (mm)	$\delta$ (mm)				$\theta$ (°)	$\Delta r_{ext}$ (mm)	$\delta$ (mm)			
		5	10	15	20			5	10	15	20
0	6.5	/	281	652	3299	0	9	99	262	538	993
0	13	/	298	482	408	90	6.5	18	137	298	3021
5	6.5	/	460	577	1114	90	13	75	220	456	500
90	9	/	233	440	2143	180	6.5	-5	95	256	1961
180	9	/	297	600	836	180	13	85	242	447	575
270	6.5	/	236	337	1360	270	9	60	222	296	466
270	13	/	294	274	270						
275	6.5	/	248	307	760						
Test-3											
$\theta$ (°)	$\Delta r_{ext}$ (mm)	$\delta$ (mm)				$\theta$ (°)	$\Delta r_{ext}$ (mm)	$\delta$ (mm)			
		5	10	15	20			5	10	15	20
0	6.5	28	165	329	1556	15	6.5	148	222	400	2137
30	6.5	65	184	332	1720	30	6.5	87	132	251	1884
60	6.5	0	135	204	770	45	6.5	53	94	181	1693
90	6.5	4	163	255	972	60	6.5	26	124	221	1659
120	6.5	12	148	224	1090	75	6.5	14	93	202	1668
150	6.5	19	144	245	1496	90	6.5	9	99	202	1673
180	6.5	13	145	285	1926						
210	6.5	15	142	309	2281						
240	6.5	7	113	262	2170						
270	6.5	-3	109	260	2090						
300	6.5	-17	96	190	1997						
330	6.5	-32	85	149	564						

Table 10: Summary of experimental relaxed strains measurements in *italic* ( $\mu\epsilon$ ) for 0.6 mm grid length strain gauges and hole diameter  $d = 100$  mm

Test-4				
$\theta$ (°)	$\Delta r_{ext}$ (mm)	$\delta$ (mm)		
		5	10	15
195	6.5	51	66	190
189	6.5	20	59	164
183	6.5	9	33	148
177	6.5	36	50	168
171	6.5	78	122	250
165	6.5	27	79	190
				1889

#### 4.4 RESULTS AND DISCUSSION

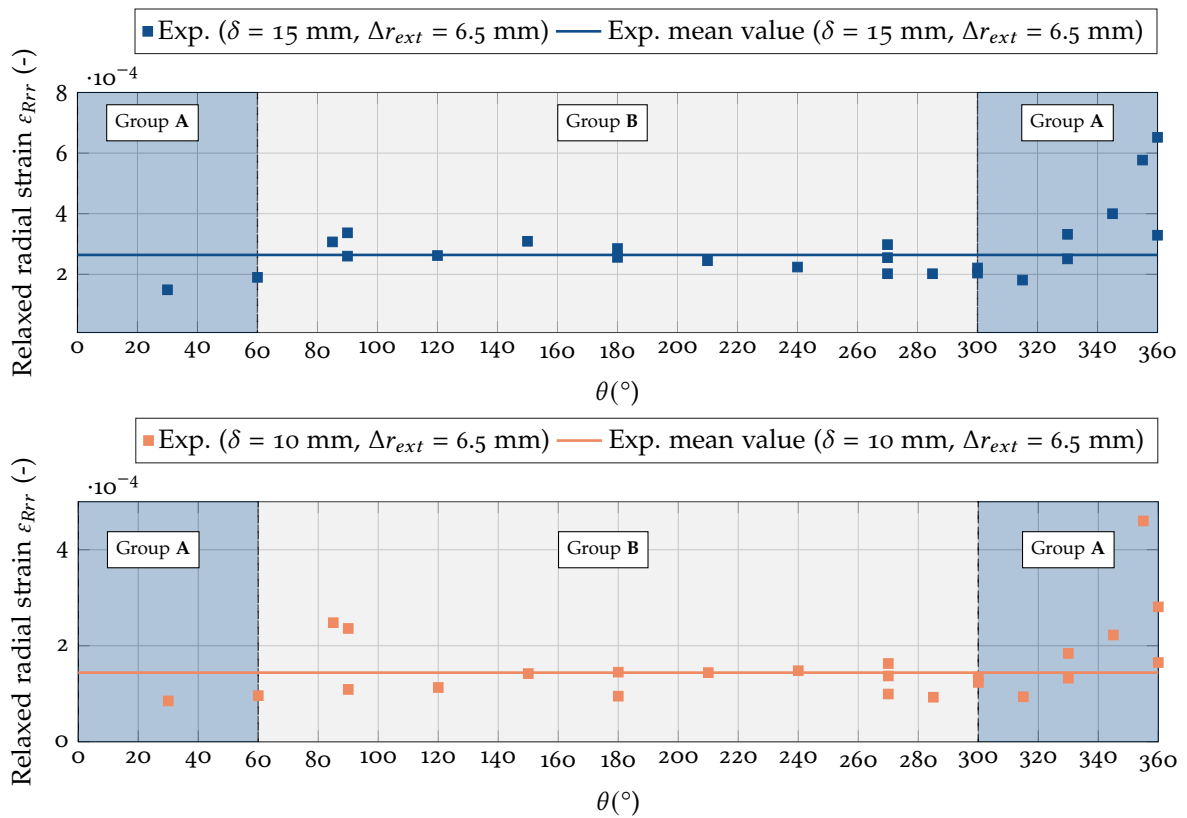


Figure 29: Relaxed radial strain over specimen hoop coordinate measured through 1.5 mm grid length strain gauges for a fixed strain gauge radial distance of  $\Delta r_{ext} = 6.5$  mm. The mean value line was obtained considering only group B measurements

In this section numerical and experimental measurements of relaxed radial strains ( $\varepsilon_{Rrr}$ ) are presented, together with a data analysis and discussion. Firstly, the experimental results of  $\varepsilon_{Rrr}$  as a function of  $\theta$  are presented in section 4.4.1. Secondly, the experimental results of  $\varepsilon_{Rrr}$  as a function of  $\theta$ , related to the 0.6 mm grid length strain gauges are given in section 4.4.2, with the aim of achieving additional indication about measurements variability related to the weld toe irregularities. In section 4.4.3, numerical and experimental results of relaxed radial strain are compared to obtain an overall validation

of the numerical model. Finally, in the following section 4.5 numerical residual stresses are discussed, specifically for the plate surface region close to the weld bead, where the fatigue crack can originate.

#### 4.4.1 Experimental results of relaxed radial strain

Experimental results of relaxed radial strain ( $\varepsilon_{Rrr}$ ) as a function of the hoop coordinate ( $\theta$ ) are shown in Figure 29 for a fixed strain gauge radial distance of  $\Delta r_{ext} = 6.5 \text{ mm}$ . In the figure two macro-regions can be roughly identified: group **A**, influence area of the run in-run out region and group **B** region where strain results can be assumed quasi axi-symmetric. It should be noted that data trend is significantly different between the two macro-regions; this is why the study of the two regions has been separated in order to enable a more accurate analysis of both numerical and experimental results.

The first region (i.e. group A), included in an approximate angular domain<sup>7</sup>  $\theta \in [-60^\circ, 60^\circ]$ , is affected by a double thermal process due to the beginning and end of the welding process and therefore presents a considerable results variation. On the contrary, in the second region (i.e. group B), included in the approximate angular domain  $\theta \in (60^\circ, 300^\circ)$ , a quasi-constant  $\varepsilon_{Rrr}$  along  $\theta$  can be observed. Data belonging to group A present mean values of  $1.80 \times 10^{-4}$  and  $3.17 \times 10^{-4}$ , and standard deviations of  $1.10 \times 10^{-4}$  and  $1.66 \times 10^{-4}$  for  $\delta = 10 \text{ mm}$  and  $\delta = 15 \text{ mm}$  respectively. Data belonging to group B present mean values of  $1.44 \times 10^{-4}$  and  $2.64 \times 10^{-4}$ , and standard deviations of  $4.9 \times 10^{-5}$  and  $4.1 \times 10^{-5}$  for  $\delta = 10 \text{ mm}$  and  $\delta = 15 \text{ mm}$  respectively.

Due to intrinsic stress variability in group A, it should be difficult to obtain a sound standard deviation value by considering all data as a single group. For this reason, a process-related variability regarding experimental relaxed strain measurements has been defined by averaging standard deviations of Group B data for  $\delta = 10 \text{ mm}$  and  $\delta = 15 \text{ mm}$ . The data involved refer to all categories of strain gauges used, i.e.  $0.6 \text{ mm}$  and  $1.5 \text{ mm}$  grid length strain gauges, obtaining a process-related standard deviation equal to  $7.8 \times 10^{-5}$ .

#### 4.4.2 Strain sensitivity to dimensional variation of the weld seam geometry

It is reasonable to expect that relaxed strains are affected by different sources of error, such as those related to accurate positioning of the grid or variability of the local weld geometry.

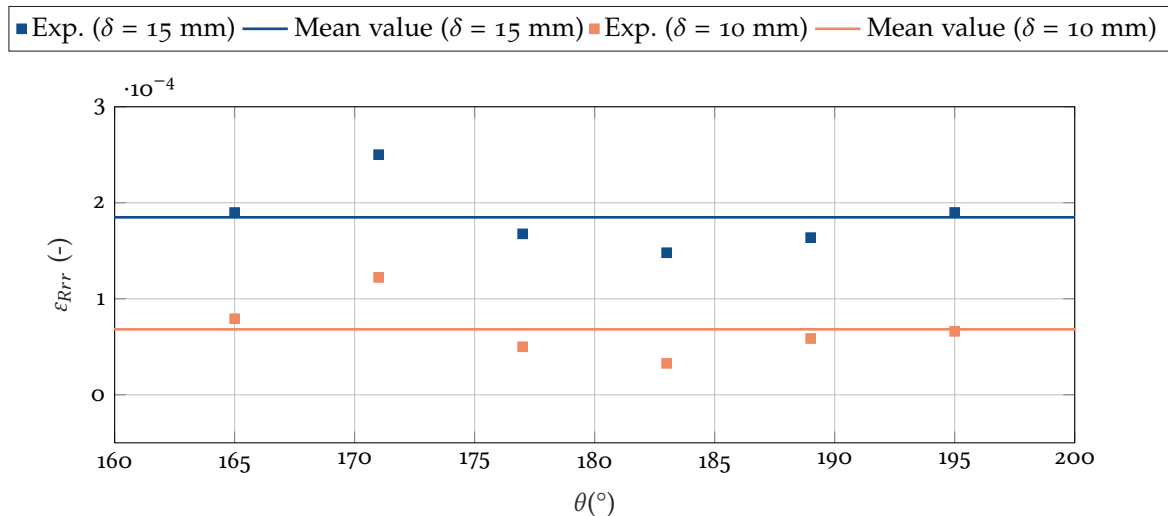


Figure 30: Relaxed radial strain data over the hoop coordinate measured through  $0.6 \text{ mm}$  grid length strain gauges; mean values are plotted as continuous lines

As already shown in Figure 29, relaxed radial strain has an almost constant trend in the angular domain  $\theta \in (60^\circ, 300^\circ)$ ; for this reason, a group of strain gauges were placed between  $165^\circ$  and  $195^\circ$ ,

<sup>7</sup> The range and domain are intended as mathematical concepts

spaced by an angle of  $6^\circ$ , to better achieve indication of the intrinsic variation due to the uneven geometry of the weld toe. Strain gauges with a grid length of  $0.6\text{ mm}$  were employed to obtain measurements shown in Table 10.

Figure 28 shows a technical drawing of the strain gauges placement together with a picture of the actual specimen geometry. As can be seen from Figure 28b, the bead geometry is not as ideal as the one implemented within the finite element model, this leads to a variable strain distribution at points where it is supposed to be constant. Figure 30 shows experimental results acquired from the measurements described above. It can be noticed that the  $\varepsilon_{Rrr}$  trend vs the angular coordinate is almost constant, for different  $\delta$  coordinates. A standard deviation of  $3.0 \times 10^{-5}$  and  $3.5 \times 10^{-5}$  and mean values of  $6.8 \times 10^{-5}$  and  $1.84 \times 10^{-4}$  have been calculated respectively for  $\delta = 10\text{ mm}$  and  $\delta = 15\text{ mm}$ . It is supposed that the observed variability mainly comes from the weld irregularities. The calculated standard deviations are comparable to the ones obtained from  $1.5\text{ mm}$  grid length strain gauges of Figure 29, which is an independent verification of the experimental reading reliability.

#### 4.4.3 Comparison between experimental and numerical relaxed strain

Since it has been already observed that relaxed strain results differ greatly between the two macro-regions (i.e. group A and group B), it was considered appropriate to study in detail these two regions, separately, according to the radial distance  $\Delta r_{ext}$ .

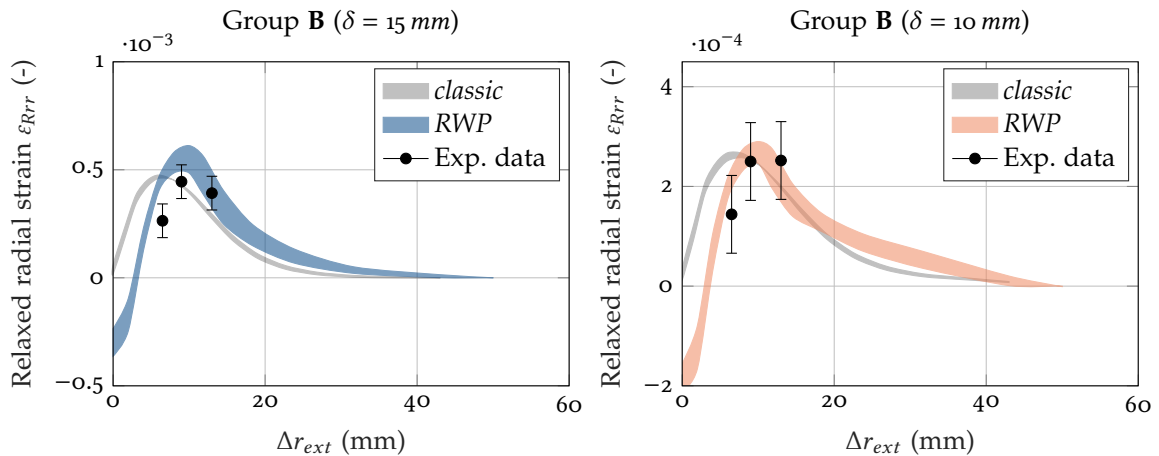


Figure 31: Comparison between numerical and experimental data of relaxed radial strains over distance from the weld toe for two different incremental hole depths in the group B. Experimental results are presented through mean value and standard deviation while numerical results are the convex hull of  $\varepsilon_{Rrr}$  data obtained in the angular domain  $\theta \in (60^\circ, 300^\circ)$

Figure 31 shows a comparison between  $\varepsilon_{Rrr}$  results for the *classic* and *RWP* methods as a function of  $\Delta r_{ext}$  for two incremental hole depths  $\delta = 10\text{ mm}$  and  $\delta = 15\text{ mm}$  in the angular domain  $\theta \in (60^\circ, 300^\circ)$ . Numerical results are presented as the convex hull of  $\varepsilon_{Rrr}$  over  $\Delta r_{ext}$  in the angular range considered (which is equivalent not to consider the dependence on the angular coordinate), while experimental measurements are reported through their mean value and standard deviation. Even if measures were taken at three different distances from the weld, the standard deviation obtained for  $\Delta r_{ext} = 6.5\text{ mm}$  was applied to all measurements. This was suggested by the fact that more data were available for  $\Delta r_{ext} = 6.5\text{ mm}$ ; moreover this was considered to be conservative, in the sense that a lower variability is expected for larger distances from the weld.

Regarding the comparison between numerical methods, both *classic* and *RWP* methods show a similar behaviour for  $\Delta r_{ext} > 13\text{ mm}$ ; however, a significant difference can be noticed in the surrounding area of the weld toe. In this case, the *RWP* method yields compressive (negative) strains for  $\Delta r_{ext} = 0$ , while the *classic* method always predicts positive relaxed radial strains. In addition, for the *classic* method, the gradient of  $\varepsilon_{Rrr}$  close to the weld toe turns out to be lower with respect the *RWP* method. These aspects, in fact, is what mainly differentiates the two models and brings the *RWP* closer to experimental data.

Although the difference between numerical and experimental results can appear considerable, it must be remembered that several assumptions have been done within the thermal-structural numerical model and experimental data examined above, the most relevant being listed below:

- simplified specimen geometry, specifically, weld seam irregularities were not considered in the FE-model;
- temperature-dependant elastic-plastic material properties largely varies within the same material between different literature sources;
- temperature field was described by a simplified thermal model ([CIT](#));
- possibility of strain gauge positioning errors, both in the radial and angular direction;
- strain gauge readings represent an averaged over the reading grid.

It is worth noting that the unusual relaxed radial strain behaviour showed in Figure [31](#) can be clarified by introducing two structural effects related to the hole drilling process. If, in an approximate way, the thermal induced shrinking of the the seam weld is considered, a structural bending and a local skin effect arise, both exemplified in the cross-sectional view of Figure [66](#). The progressive cutting, starting from the lower plate surface, allows the upper part to bend due to stress relieving. At the same time, weld bead contraction generates a skin-positive radial effect. During incremental drilling these two factors will combine generating the strain profile of Figure [31](#).

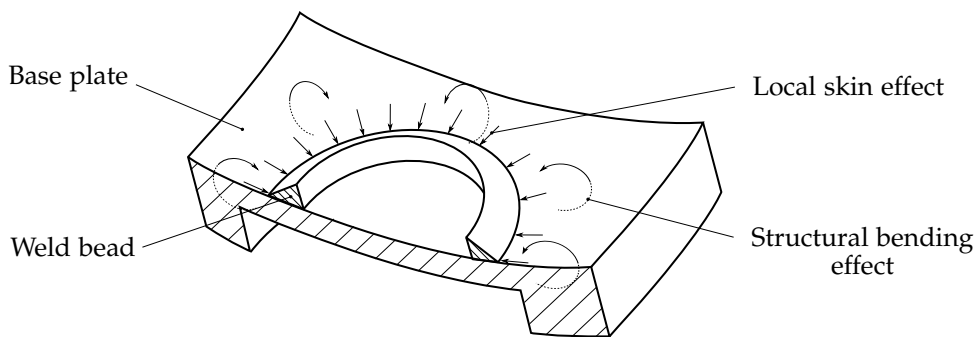


Figure 32: Cross-sectional view of the base plate and weld bead with outlined the bending and skin effects due to the incremental cutting process

For the sake of clarity, group A results are also presented in Figure [33](#). In this case, as already mentioned, given the trend of experimental data the calculation of a standard deviation seems unwise. For this reason, the total  $\varepsilon_{Rrr}$  range has been reported (i.e. represented by asterisks) with the mean value also indicated. The lack of data for  $\Delta r_{ext} = 9 \text{ mm}$  and  $\Delta r_{ext} = 13 \text{ mm}$  does not allow the identification of a mean value, making the use of the standard deviation unnecessary as well. Therefore, for  $\Delta r_{ext} = 9 \text{ mm}$  and  $\Delta r_{ext} = 13 \text{ mm}$ , the experimental points available have been directly reported.

With the exception of the experimental point at  $\Delta r_{ext} = 13 \text{ mm}$  and  $\delta = 10 \text{ mm}$ , numerical results relative to the [RWP](#) method were well predicted from experimental data. With regard to the comparison between the numerical methods, the observations made earlier regarding Figure [31](#) remain unchanged. For instance both methods resemble each other in the descending  $\varepsilon_{Rrr}$  phase while they behaved quite differently in the proximity of the weld toe.

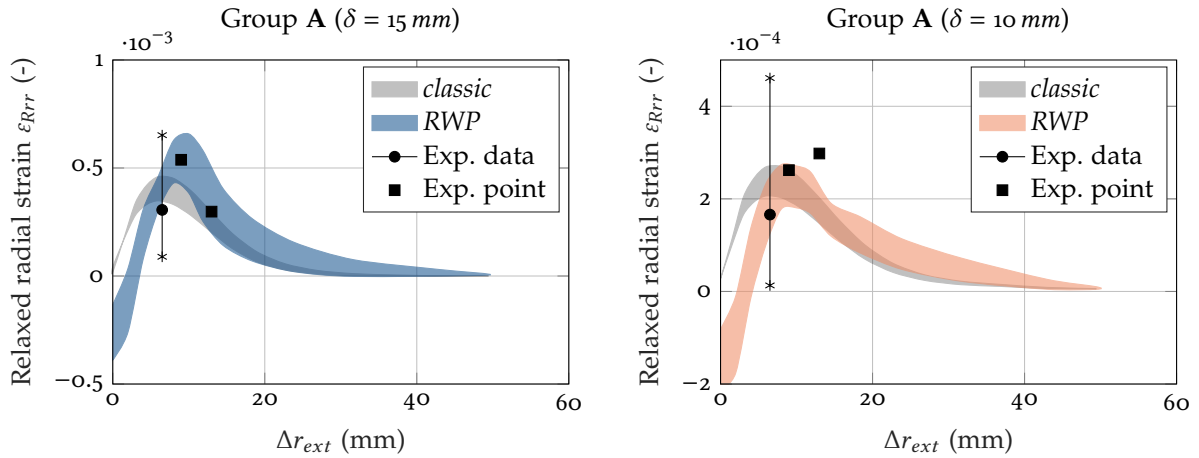


Figure 33: Comparison between numerical and experimental data of relaxed radial strains over distance from the weld toe for two different incremental hole depths in the group A. Experimental results are reported through of mean value and standard deviation while numerical results are the convex hull of  $\varepsilon_{Rrr}$  data obtained for two angular domains  $\theta \in [-60^\circ, 60^\circ]$

#### 4.5 RESIDUAL STRESSES DUE TO THE WELDING PROCESS

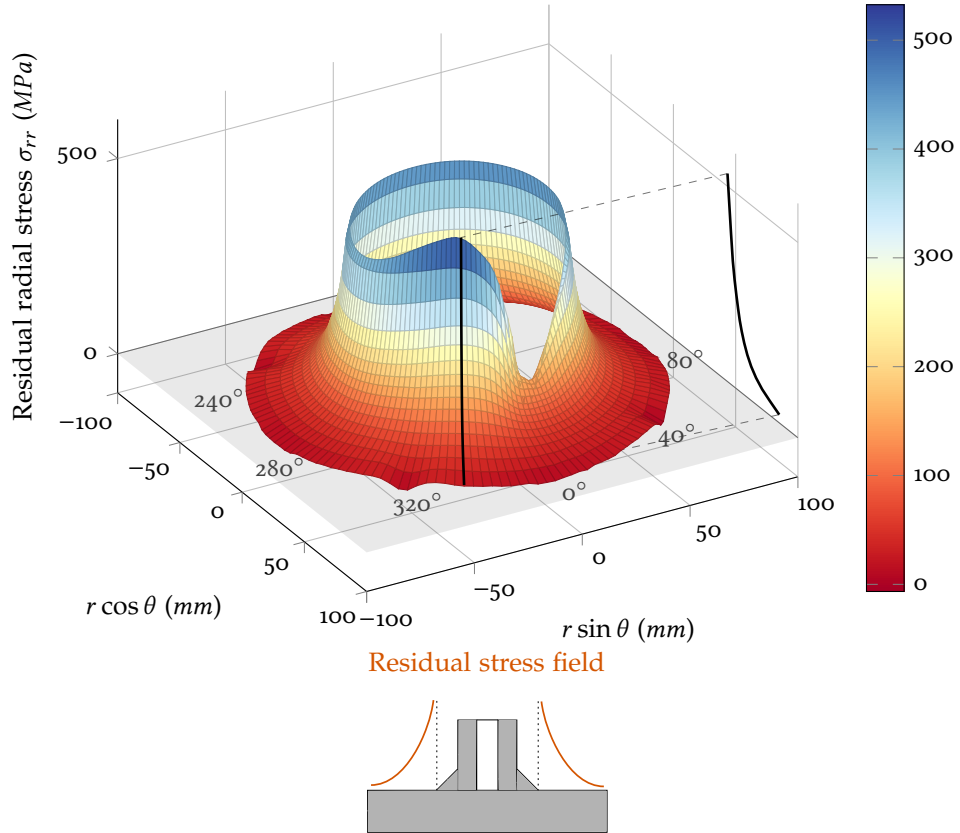


Figure 34: Overall residual radial stress field on the plate surface ( $z = 0$ ), for a radial domain  $r \in [42 \text{ mm}, 78 \text{ mm}]$ , together with a graphical representation of the domain under consideration

This section presents numerical data of residual hoop and radial stress, in order to investigate their behaviour and assess the numerical model accuracy. Figure 34 shows the global residual radial stress field on the plate surface, around the weld seam. The figure displays radial stresses in the radial domain  $r \in [42 \text{ mm}, 78 \text{ mm}]$  on the upper plate surface. Similarly, Figure 35 shows the hoop stress around

the weld bead in the same radial domain  $r \in [42 \text{ mm}, 78 \text{ mm}]$ . It can be observed that both figures clearly identify the run in-run out point through the angular coordinate at  $\theta = 0^\circ$ . For the sake of clarity, the 2D-curve of maximum stress is also represented (i.e. black line), as a projection on the vertical plane, as well as the  $z = 0 \text{ mm}$  plane (i.e. light grey plane). Because of the notch effect given by the weld seam, the maximum stress is globally reached in the weld toe both for radial and hoop residual stresses. Especially for residual radial stress, the maximum stress value reached is  $507 \text{ MPa}$  which exceeds the yield strength of the material at room temperature. It is interesting to notice that radial stresses increment was found in a region quite close to the weld toe; referring to Figure 34, in about  $\approx 7 \text{ mm}$  distance from the weld toe, radial stress increases from  $\approx 150 \text{ MPa}$  to  $\approx 500 \text{ MPa}$ . The residual stress may rise beyond the yield point in localized areas, due to the high stress concentrations [123]. It has to be considered that the weld toe had been shaped with null radius, resulting in a high stress/strain gradient near the notch. However, relaxed radial strains were obtained sufficiently far away, in area where the highest gradient had probably no effect.

In the case of radial residual stress the maximum stress value is reached for an angle of  $331^\circ$ , while in the case of hoop residual stress the maximum is reached for an angle of  $324^\circ$ . It is worth noting that in both cases the stress surface is axisymmetric for  $\theta$  values far from the run in-run out point. Actually, for  $\theta = 0^\circ$  there is a significant stress reduction both in radial and hoop stresses of  $270 \text{ MPa}$  and  $210 \text{ MPa}$  respectively; similar results have been experienced in a tube-tube welded joint when residual stresses were evaluated through the hole drilling technique by Sepe et al. [124].

Residual radial stresses are always positive, showing a monotonous growing behaviour for  $\Delta r_{ext} \rightarrow 0$ . On the contrary, residual hoop stresses are mostly compressive, except for a region close to the weld toe, where the stress gradient is steeper compare residual radial stresses. A useful comparison between analytical models and numerical results derived from FEA is given in Appendix B. Two classical analytical models have been used to predict residual stresses in the vicinity of the weld bead. The analytical models, although being rather simple, give additional insight into the process of residual stress generation.

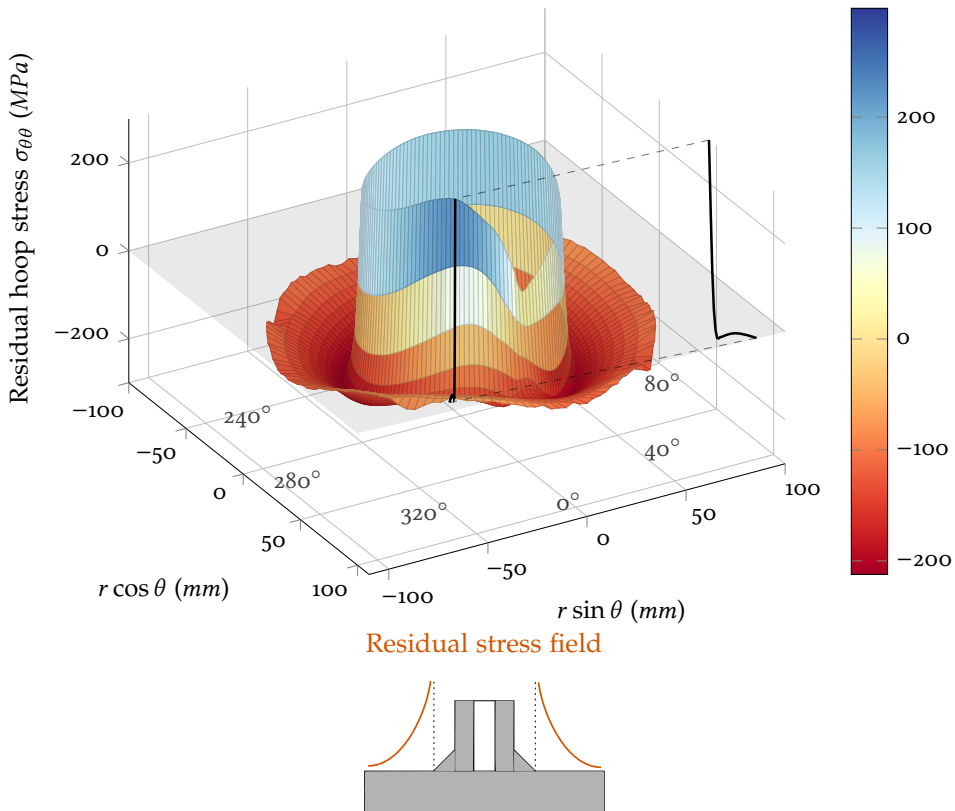


Figure 35: Overall residual hoop stress field on the plate surface ( $z = 0$ ), for a radial domain of  $r \in [42 \text{ mm}, 78 \text{ mm}]$ , together with a graphical representation of the domain under consideration

For clarity of interpretation, Figures 34 and 35 show ripples in the stress surface for stress values close to zero. This unusual behaviour is due to the quadrangular geometry of the plate and the presence of four holes on the plate corners. This behaviour, however, is related to a surface region of low stress gradient and presents a negligible stress variation compared to the stress gradient in the weld toe area.

#### 4.6 CONCLUSION

The thermal-structural model developed in this chapter has proven to be reliable to determine the relaxed strain field in the pipe-to-plate welded joint after incremental hole cutting. As a matter of fact, numerical results were in good agreement with the experimental ones. The numerical residual stress field thus derived will be used in the numerical simulation for fatigue damage calculation presented in the next chapters. Figures 34–35 shows only part of the residual stress results obtained numerically on the upper plate surface. This region has been taken as a reference as it was used for the numerical model validation through comparison with experimental relaxed strain results. However, the entire domain solution will be used in the subsequent numerical models in order to consider damage deriving from all the weld bead notches.

# 5

## EXPERIMENTAL FATIGUE TESTING OF WELDED JOINTS

After fully defining the residual stress field by means of thermal-structural simulations ([chapter 4](#)), an investigation on the effect of residual stresses on fatigue life of welded joints has been made. In this chapter the experimental fatigue campaign of pipe-to-plate welded joints is presented. Specimens in as-welded and stress relieved conditions subjected to fully reversed bending and torsion loading were tested.

### 5.1 MATERIAL AND METHODS

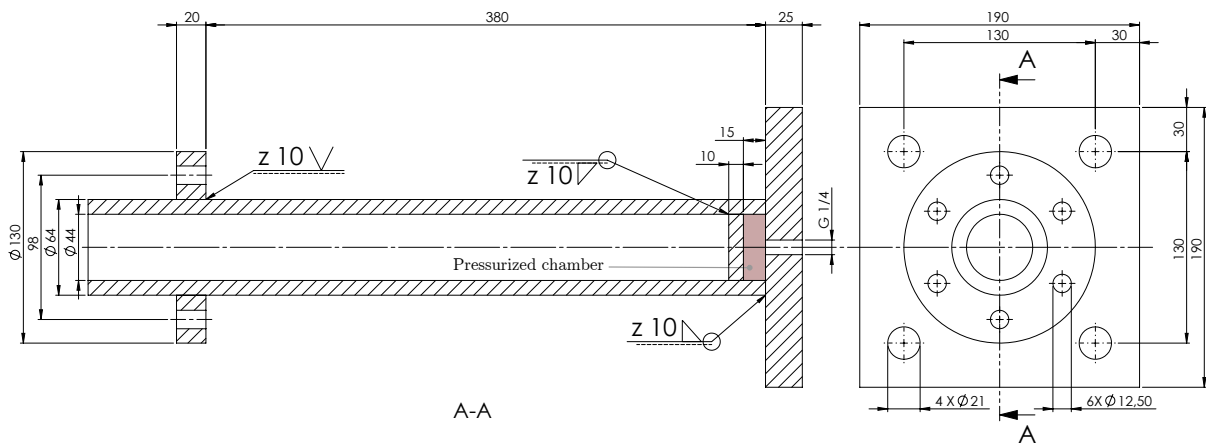


Figure 36: Technical drawing of the investigated pipe-to-plate welded joint with dimensions in millimetres and welding representation according to ISO 22553:1992

The specimen maintains the same geometry as the one already presented in Figure 7 (i.e. a pipe-to-plate welded joint made of S355JR structural steel). However, the integration of an upper circular plate (Figure 36) was essential to connect the specimen and actuators during the fatigue test campaign. The specimens were tested under load control by means of 63 kN linear actuators in a frequency range of 5 Hz – 10 Hz through a properly developed test-bench, as shown in Figure 37a. The joints were clamped to the test-bench by means of four bolts in order to engage the base plate to the crankcase. A central gas thread of 1/4 of inches (G1/4 of standard ISO 7-1:1994) was used to pressurize the lower chamber and detect, by means of a pressure transducer, any through-the-thickness crack that might nucleate during fatigue testing. The load was applied to the specimens through a loading arm, connected to two independently controlled hydraulic actuators. Tests were performed under fully reversed ( $R = -1$ ) bending (equal loads on both actuators) and under fully reversed ( $R = -1$ ) torsion (opposite loads on the actuators). Tests were interrupted when a through-the-thickness crack was detected by a pressure drop in the pressurized chamber. In order to evaluate the influence of residual stress on the fatigue life assessment of the welded joints, some specimens were stress relieved before testing; to this aim specimens were heated up to 630 °C with a heating rate of 10.5 °C min<sup>-1</sup>, held at 630 °C for 4 h and then cooled down, slowly, left in the furnace until room temperature was reached.

A microstructure analysis of the specimens, in particular in the weld seam region, was carried out by micrographs and hardness tests, obtained through an optical microscope Leica DMI3000M and an Akashi AVK-C1 hardness machine, respectively.

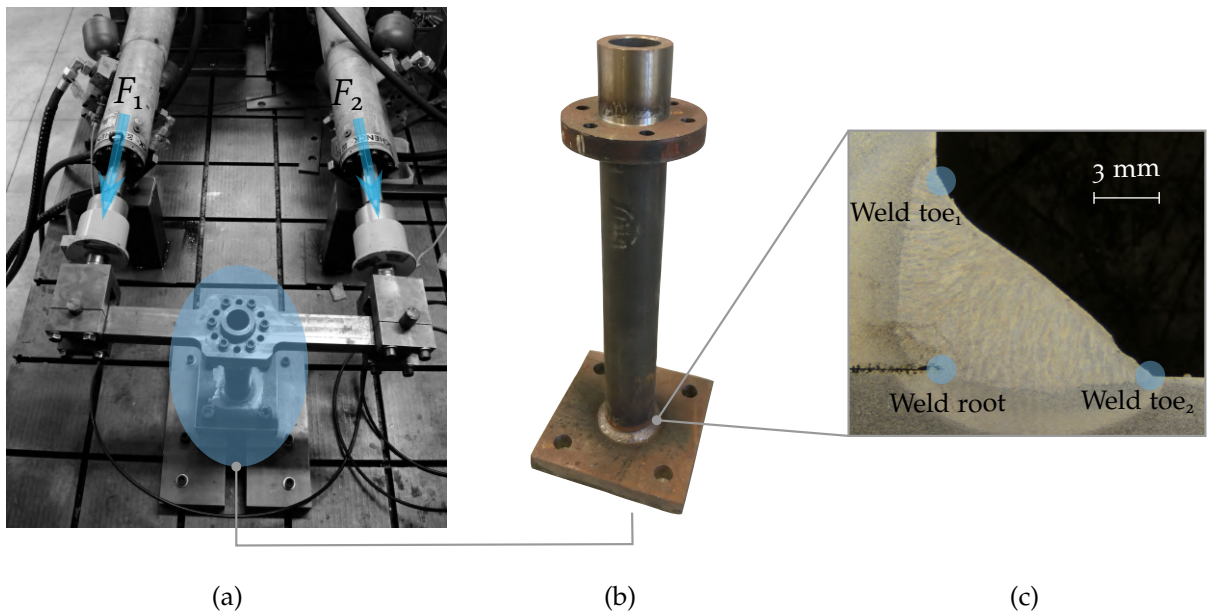


Figure 37: Test-bench employed for fatigue testing (a), pipe-to-plate welded joint (b) and micrography of the weld seam (c)

## 5.2 EXPERIMENTAL ANALYSES

### 5.2.1 Fatigue analysis

All specimens have been tested through the test bench already presented in section 5.1. Table 11 and Table 12 present experimental data related to the as-welded and stress-relieved specimens, respectively. Besides the specimen number and loading condition, the batch to which each specimen belonged to is also shown, thus to underline the different time of testing. Results are given in terms of nominal stress range ( $\Delta\sigma_n$ ) and number of cycles to break-through ( $N_f$ ), where  $\Delta\sigma_n$  has different formulation according to the load type involved (i.e. pure bending or pure torsion), as shown in equation 28.

$$\Delta\sigma_n = \frac{2M_b}{\frac{\pi}{64}(d^4 - d_t^4)} \frac{d}{2} = \frac{2\sqrt{3}M_t}{\frac{\pi}{32}(d^4 - d_t^4)} \frac{d}{2} \quad (28)$$

where  $M_b$  and  $M_t$  are the bending moment and torque respectively,  $d$  is the diameter identified by the weld toe on the plate and  $d_t$  is the external pipe diameter.

Table 11: Experimental results of as-welded specimens under pure bending (B) and pure torsion (T) loading (load ratio  $R = -1$ )

Specimen no.	Load	Batch no.	$\Delta\sigma_n(MPa)$	$N (\times 10^6)$
1	B	1	141	0.21
2	B	1	141	0.28
3	B	1	141	0.38
4	B	1	105	0.85
5	B	1	90	1.69
6	B	1	87	1.44
7	B	2	179	0.85
8	B	2	204	0.116
9	B	2	189	0.574
10	B	2	196	0.136
11	B	2	164	0.626
12	B	2	186	0.197
13	B	2	146	1.50
14	B	2	143	0.902
15	B	2	136	0.684
16	B	2	125	run out
17	B	3	130	1.49
18	B	3	143	0.826
19	B	3	196	0.182
20	T	2	202	1.89
21	T	2	222	0.51
22	T	2	182	1.62
23	T	2	202	0.564
24	T	2	192	1.23
25	T	2	232	0.190
26	T	2	202	0.427
27	T	2	192	1.36
28	T	2	242	0.130
29	T	2	242	0.235
30	T	2	252	0.266
31	T	2	272	0.235
32	T	2	171	run out
33	T	3	222	run out
34	T	4	262	0.121
35	T	4	242	0.433

Table 12: Experimental results of stress relieved specimens under pure bending (B) and pure torsion (T) loading (load ratio  $R = -1$ )

Specimen no.	Load	Batch no.	$\Delta\sigma_n$ (MPa)	$N \times 10^6$
1	B	3	137	0.602
2	B	3	137	0.463
3	B	3	124	0.613
4	B	3	111	run out
5	B	3	183	0.198
6	B	4	150	0.414
7	B	4	170	0.255
8	T	3	202	run out
9	T	3	250	0.970
10	T	3	262	1.86
11	T	3	282	0.378
12	T	3	323	0.149
13	T	4	262	0.810
14	T	4	323	0.260

### 5.2.2 Microstructure analysis

The heat treatment influence on the microstructure and mechanical properties was analyzed through microstructural analyses and hardness measurements. Two samples were employed for this. One sample was extracted from the weld bead of the AW and one from the weld bead of the SR joint. Both samples were extracted far from the crack initiation point. The samples were obtained through cuts made on a plane containing the pipe axis. The samples were incorporated in a thermosetting resin, grounded using SiC waterproof papers with grits of 120, 320, 500, 800 and 1200, then mirror-polished using diamond paste. In order to highlight the microstructure, they were etched with Nital reagent (2%). Samples were observed by Leica DMI3000 M optical microscope. Micro hardness measurements were performed according to ASTM E92-17 [125] using the approximate test force of 10 kgf. The measurements were performed along a line orthogonal to the bisector of the bead angle.

Figure 38 shows the optical microscope micrograph of the joint in AW condition. Figure 38a focuses



Figure 38: Optical microscope micrograph of the joint in AW condition. Focus on the weld toe showing FZ, CGZ, FGZ and BM (a). Detail of the microstructure transition between FZ and CGZ (b), CGZ and FGZ (c), FGZ and BM (d)

on the weld toe showing four main areas produced by welding. According to the denominations used in the scientific literature [126]–[128] they have been named: FZ, CGZ, FGZ and BM. The FZ is the region formed by the solidification of the filler metal while the BM is the region of the joint material that has kept its microstructural characteristics unchanged during the welding process. The portion of material between BM and FZ during welding undergoes a heat process that alters its original microstructure. This zone is generically referred to as the HAZ. The portion of the HAZ closest to the FZ is subjec-

ted to high temperature values, close to the melting temperature of the steel. The long stay at high temperature makes the austenite grain coarser forming the CGZ [129]. Conversely, the portion of HAZ closest to the BM is subjected to lower temperature values and short dwell times, producing fine prior austenite grain [130] forming the FGZ. Figure 38(b-d) show the microstructural variation of the bead progressively moving away from the FZ.

Figure 39(a-d) show in detail the microstructure of the four zones described above. Figure 39a shows the microstructure of the BM characterized by perlite islands surrounded by proeutectoid ferrite (white phase). Figure 39b shows the microstructure of the FGZ, it appears uniform with very fine grain showing characteristics typical of a martensitic or bainitic microstructure. The microstructures of the CGZ (Figure 39c) are characterized by the presence of pearlitic colonies with small ferrite islands. Similarly, the microstructure of the FZ (Figure 39d) is uniformly distributed perlite.

Figure 39(e-h) show the corresponding microstructures of the joint in the SR condition, obtained in the same position as the previous ones. The BM Figure 39e did not undergo microstructural changes following the thermal process, its microstructure remained the same as that of the BM in the AW condition. However, the microstructures obtained in the HAZ and FZ of the joint in the SR condition (Figure 39(f-h)) are similar among each other and significantly different from those in the AW condition. The Fe<sub>3</sub>C layers present in the perlite have lost their lamellar shape and appear uniformly distributed in the ferritic matrix [131].

The exposed metallographic analysis was also carried out on a specimen extracted from the weld bead in correspondence with the region in which there is simultaneously the beginning and the end of the welding process, both for the AW and SR condition. This is because it undergoes a thermal history that is significantly different from the other points of the joint. This point is called the "run in-run out". However, the metallographic analysis carried out on the "run in-run out" cross-section did not show any significant difference. Therefore the above analysis can be considered as representative of the entire weld bead.

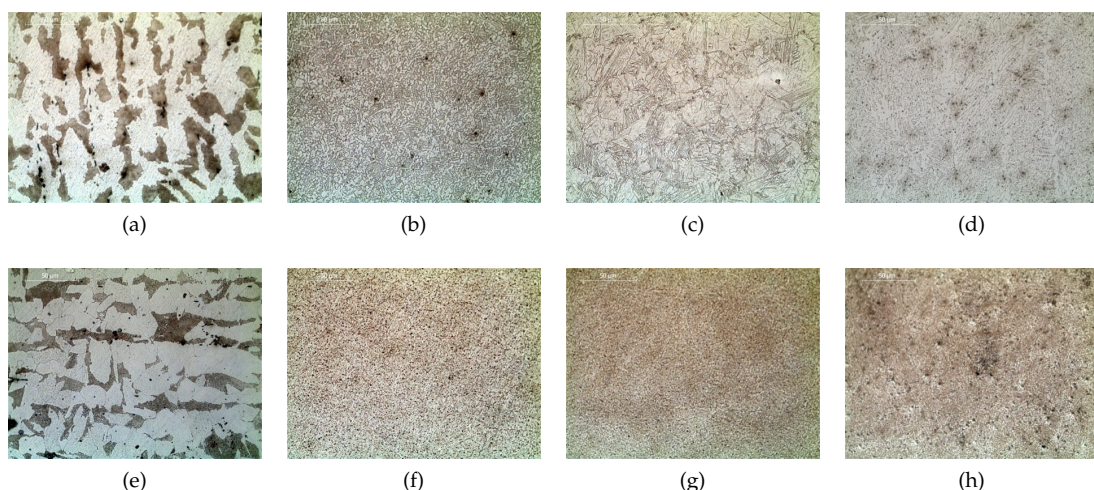


Figure 39: Optical microscope micrograph showing the microstructures of the BM (a), FGZ (b), CGZ (c) and FZ (d) of the joint in the AW condition; the subfigures (e-h) show the corresponding microstructures of the joint in the SR condition

Figure 40 shows the comparison between the hardness distribution around the weld toe in AW and SR condition.

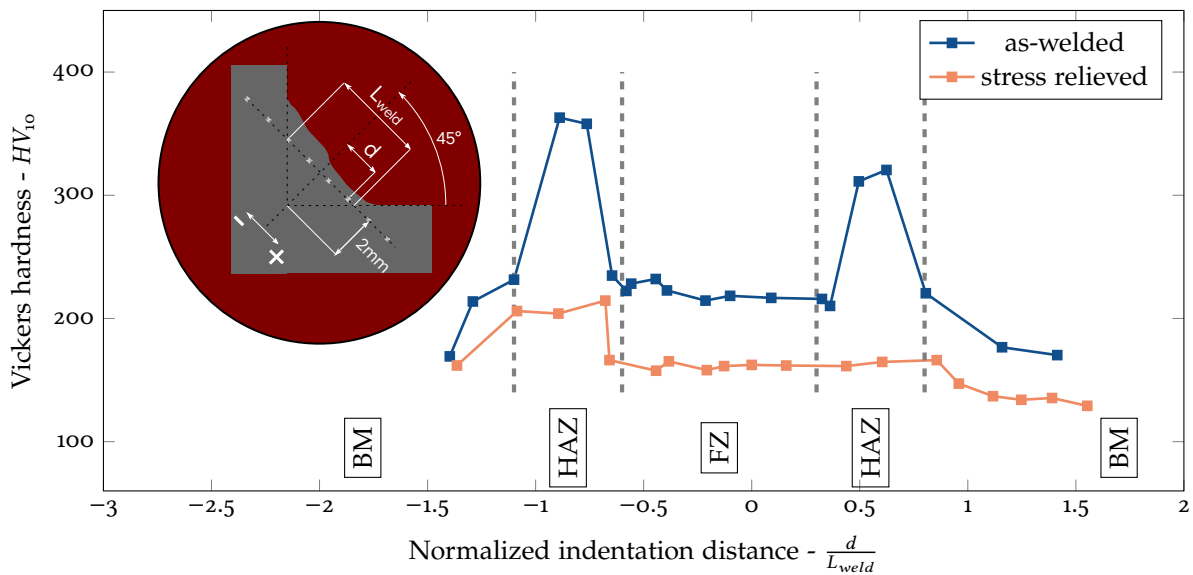


Figure 40: Vickers hardness distribution around the weld toe in as-welded and stress relieved conditions

The graph shows a diagram of the weld bead which defines the reference system adopted, the weld length  $L_{weld}$  and the indentation distance  $d$ . The normalized indentation distance  $d/L_{weld}$  is reported on the abscissa axis and the Vickers hardness on the ordinate axis ( $HV_{10}$ ). It should be noted that the ordinate scale does not start from zero but is such as to highlight differences between the examined samples. The hardness profile of the joint in the [AW](#) condition has a symmetry with respect to the center of the bead. The [FZ](#) assumes an uniform hardness value equal to 230HV. The maximum value obtained is 370HV in correspondence with the [FGZ](#) where the material has a finer microstructure. The hardness profile of the joint in the [SR](#) condition appears uniform assuming hardness value equal to 170HV in the region of [FZ](#) and [HAZ](#) while it decreases slightly in the [BM](#) area. The heat treatment has overall reduced the hardness of the steel uniforming it along the entire joint. The high hardness values obtained in the [FGZ](#) have undergone a variation  $\Delta H$  of about 170HV. Considering the percentage of carbon and of the alloying elements reported in Table 3 the value obtained is in accordance with the traditional theory which expresses the hardness of martensite after tempering at  $630^\circ$  for 4h [132], [133]. The results obtained from the metallographic and hardness analysis were found to be in agreement with the results of the literature for subcritical annealing treatments.

### 5.2.3 Fracture analysis



Figure 41: Fractured surfaces from torsional loading: plate view (a) and pipe view (b)



Figure 42: Fractured surfaces from bending loading: plate view (a) and pipe view (b)

Cracks always initiated from the weld root for pure torsion and mainly from the root, with some failures originated from the weld toe on the plate side, under pure bending loading<sup>8</sup>. The weld root represents, indeed, the region where the highest stress intensification occurs and, as illustrated in [134], where the highest damage parameters were found.

Figure 41 shows the failure surfaces on the plate and tube side for a specimen torsionally loaded with  $\Delta\sigma_n = 222 \text{ MPa}$ , while Figure 42 reports the failure surfaces on the plate and tube side for a specimen loaded in bending with  $\Delta\sigma_n = 183 \text{ MPa}$ . In both cases the sample separation was achieved by a post-fatigue-test brittle fracture process; the fracture was induced by the break-up process obtained through the combination of high static load and low temperature. It can be identified that in both cases cracks start at the weld root and propagated into the weld seam. For the torsionally loaded specimen of Figure 41, it is difficult to identify a principal direction for propagation as many initiation points exist. However, in the case of bending, the  $45^\circ$  direction appears to be predominant for crack propagation.



Figure 43: Fractured surfaces for pure bending (a) and pure torsion (b) loading

In Figure 43 two typical example of the failure surfaces obtained under pure bending and pure torsion can be observed (they are highlighted by the dashed lines).

Figure 43a shows a typical fracture surface developed by mode I fracture, both locally and globally. There is usually a single (or few) crack initiation point (i.e. in the most stressed area) from which the crack tends to propagate fairly quickly, showing no degree of interlocking. On the contrary, Figure 43b shows a typical *factory roof* crack propagation pattern with multiple fracture initiation points and frequent plane transitions (i.e. cracks alternate between planes at maximum normal stress). Cracks grow via mode III globally and mode I only locally, showing a high degree of interlocking which decreases the crack propagation rate.

It is worth noting that, no differences were observed in the macroscopic morphology of the fracture

<sup>8</sup> The variability in the starting crack location can be attributed to the inherent variability of welds geometry

surface, between the AW and SR specimens.

### 5.3 EXPERIMENTAL RESULTS

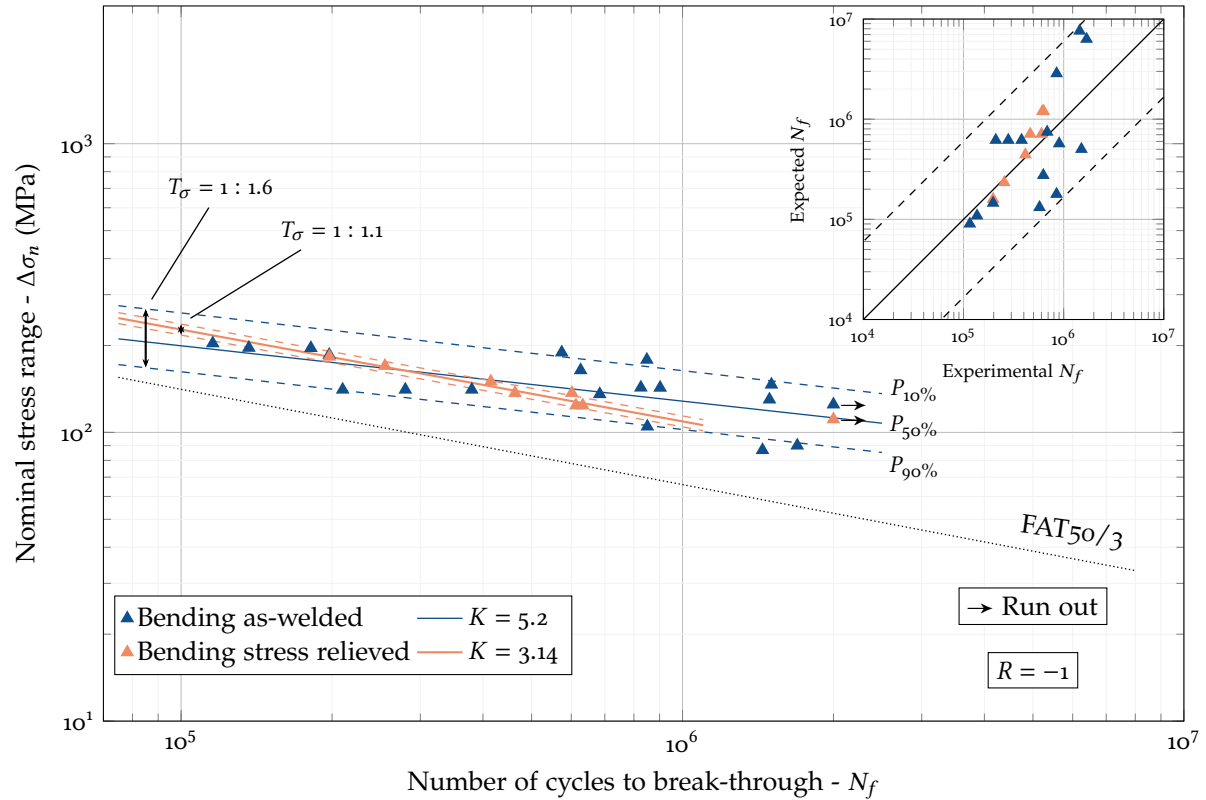


Figure 44: Nominal stress range over number of cycles to break-through for pure bending loading in as-welded and stress relieved conditions; expected vs. experimental number of cycles to break-through are displayed in the top right corner of the figure

Figure 44 and Figure 45 show the fatigue endurance of both AW and SR specimens for pure bending and pure torsion loading, in terms of nominal stress range ( $\Delta\sigma_n$ ) vs. number of cycles to break-through ( $N_f$ ). Slope coefficients of  $K = 5.2$ ,  $K = 7.4$  and nominal stress ranges at  $10^6$  cycles of  $129.4 \text{ MPa}$ ,  $199.7 \text{ MPa}$  were obtained for a survival probability of  $50\%$  ( $P_{50\%}$ ) for bending and torsion loading cases in the AW condition, respectively. While in the case of SR specimens  $K = 3.14$ ,  $K = 9.4$  and nominal stress ranges at  $10^6$  cycles of  $109.1 \text{ MPa}$ ,  $264.5 \text{ MPa}$  were obtained for a survival probability of  $50\%$  ( $P_{50\%}$ ) for bending and torsion loading cases respectively.

It can be clearly observed that residual stresses lead to a significantly different outcomes under the two load scenarios. In particular, data obtained for SR specimens subjected to pure torsion exhibit an increased in fatigue life by a factor bigger than four if compared to the torsion AW data. On the contrary, no appreciable difference can be noticed for the specimens loaded in bending, as all results lie within the same life scatter-band. Another experimental evidence resulting from Figure 44 and Figure 45 is that results of SR specimens show a significant reduced dispersion. This occurs both in bending and in torsion. The scatter band  $T_\sigma$  reduces from  $T_\sigma = 1:1.6$  to  $T_\sigma = 1:1.1$  in pure bending case, and from  $T_\sigma = 1:1.19$  to  $T_\sigma = 1:1.13$  if torsion is considered. The scatter band  $T_\sigma$  is defined as the ratio between stresses on the  $P_{10\%}$  curve against the  $P_{90\%}$  curve, specifically referred to a survival probability of  $10\%$  and  $90\%$ .

For comparison purposes, FAT curves (i.e. with a p.s. of 97.7%) relative to steel welded joints have been presented in both Figure 44 and Figure 45. The threshold curve for bending (i.e. FAT<sub>50/3</sub>) refers to IIW fatigue recommendation [135] regarding the structural detail no. 913 loaded in traction. All results fall on the conservative side. The experimental slope of the curve is higher than the one from [135] for

**AW** data, while a similar slope can be found for **SR** specimens. In the case of pure torsion, a FAT80/5 is suggested for the fatigue resistance of partial penetration welded joints on the basis of shear stresses. In order to report all data on a  $\Delta\sigma_n$  vs.  $N_f$  plane a resolved FAT curve was derived by multiplying the IIW curve by a factor of  $\sqrt{3}$ . In this case too, all the results lie on the conservative side of the plane, while FAT curve presents a greater slope if compared with **AW** and **SR** specimens experimental data.

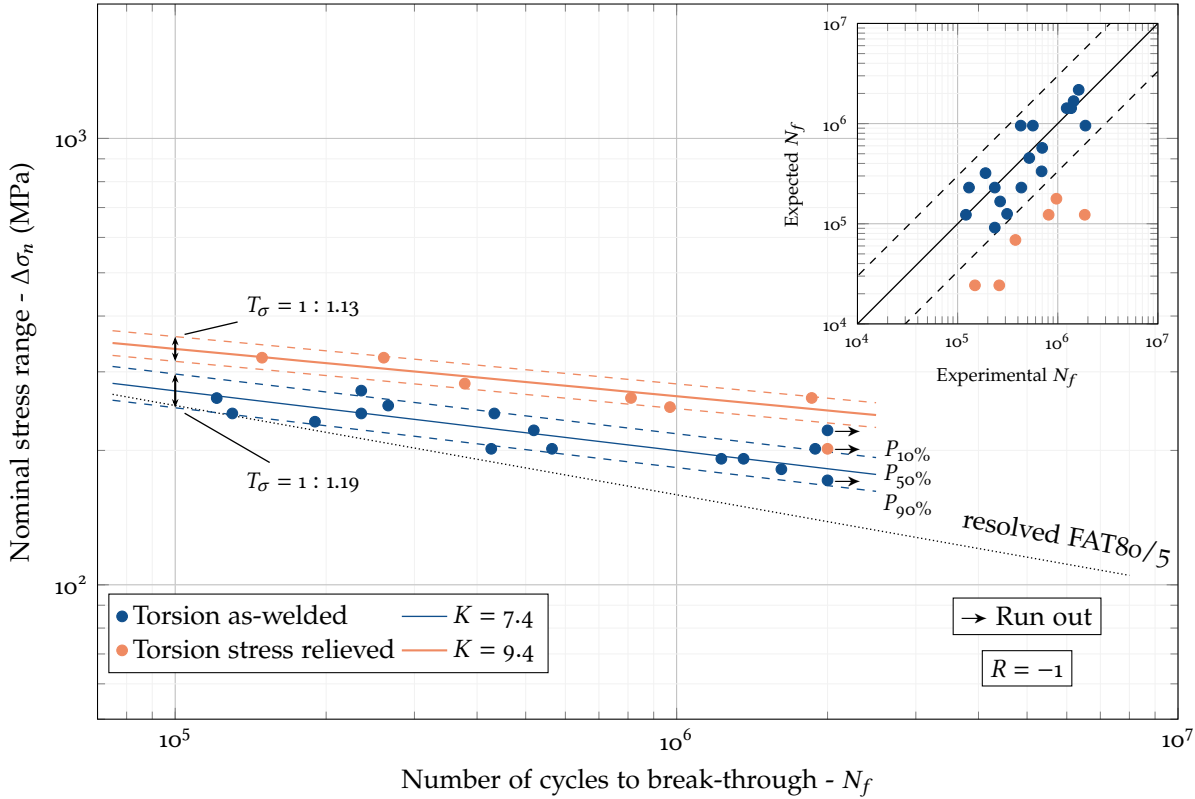


Figure 45: Nominal stress range over number of cycles to break-through for pure torsion loading in as-welded and stress relieved conditions; expected vs. experimental number of cycles to break-through are displayed in the top right corner of the figure

In the upper right corner of the Figures, the *expected vs. experimental number of cycles to break-through* graph has also been reported. All data point were derived with respect to torsion and bending power-laws in **AW** condition. Similar consideration can be drawn also in this case. Stress relieved specimens loaded in torsion exhibited an experimental endurance significantly longer the ones in the **AW** condition. Indeed, it can be observed that all **SR** torsion data fall outside the factor three life scatter-range that encompasses all **AW** torsion data. On the contrary, for bending data, no noticeable difference between **SR** and **AW** can be observed. Specifically, all points fall within a factor six life scatter-range.

#### 5.4 CONCLUSION

The experimental analysis of the fatigue data showed a clear difference in the behaviour between **AW** and **SR** specimens loaded in torsion and bending. An effect of residual stress was found only for torsionally loaded specimens, while no difference in fatigue life was observed for bending loaded specimens. In the following, a numerical analysis on fatigue damage factors will be carried out to try to confirm and understand experimental results.



# 6

## NUMERICAL SIMULATION OF FATIGUE DAMAGE

After conducting the experimental fatigue campaign for the welded tube-to-plate joints, a numerical analysis was carried out.

In this chapter numerical simulations used for the calculation of fatigue damage factors are presented and their results discussed together with experimental data obtained from [chapter 5](#).

Before introducing the model used to compute fatigue damage factors, a brief run-through of the thermal-structural simulation presented in [chapter 3](#) and [chapter 4](#) will be provided.

### 6.1 THERMO-STRUCTURAL ANALYSIS

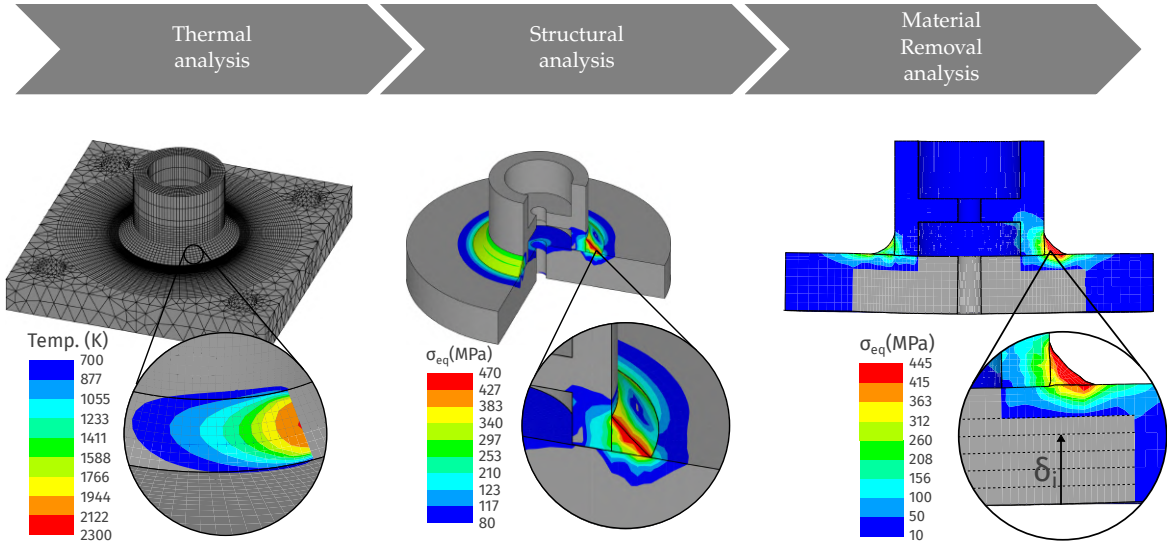


Figure 46: Flow chart of the uncoupled thermal-structural simulation for residual stresses evaluation in the pipe-to-plate welded joint

Figure 46 summarises the simulation steps used to obtain the residual stress state by means of a thermal-structural analysis, which reproduces the thermomechanical response of the material due to the welding process. The analysis has been performed through an uncoupled transient numerical model, in which thermal and structural simulations have been sequentially solved. The thermal analysis was firstly solved, in which the nodes temperature was the only degree of freedom involved. The analysis intended to determine the transient thermal profile due to the heat input occurring during the welding process. The heat source used in this case, differs from the classic Goldak models commonly employed in literature; it is a [CIT](#) model developed by the same authors and validated in the previous [chapter 3](#) and [chapter 4](#). The [CIT](#) model is based on a single calibration parameter configurable by comparison with experimental data; it was proved to be an optimal trade-off between accuracy and computation effort. The thermal model simulates the temperature profile due to the welding process using the *element birth and death* method, while activating a fixed number of elements belonging to the weld seam. Subsequently, residual stresses and strains have been determined through a structural analysis which employs the previously obtained thermal history as input load. The structural analysis applies the correct solidification sequence of the molten metal belonging to the weld bead by using a macro code implemented in the finite element program (called [RWP](#)). According to this method, at each load step, only the elements whose nodes had a temperature lower than the melting temperature

were activated. The result, shown in Figure 47, represents what is typically expected from the solidification of a pool of molten metal; it is worth noting that due to the higher conductivity between metal and air, a layer of colder metal is present on the surface of the weld material, in contact with the environment.

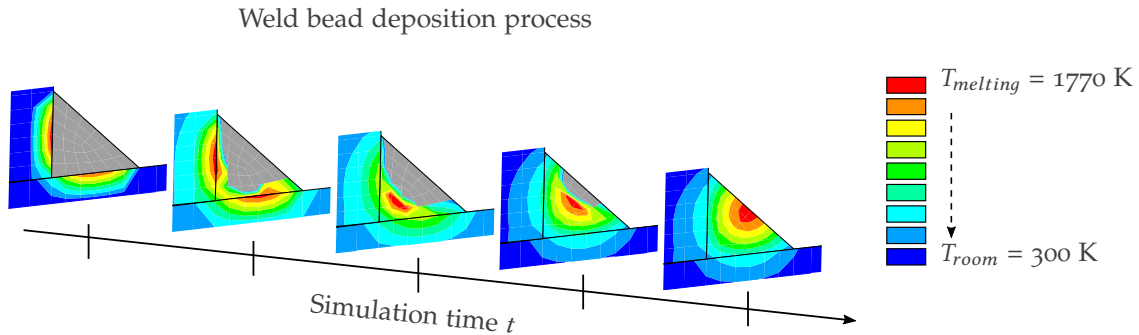


Figure 47: Example of cooling sequence during the structural simulation for the RWP method for a cross section of the weld seam

The previously described numerical model was validated by comparing the experimental relaxed strains, obtained as described in [51], with the numerical relaxed strains ([136]), obtained by reproducing the material removal in the FE model. Results were compared and the sound agreement between numerical and experimental data proved the quality of the model described above.

The temperature-dependent thermal and mechanical properties of the material were derived by Zhu et al. [108]. Material properties up to a temperature of 1273 K were implemented in the structural simulation, since no difference was exhibited from implementing properties at higher temperatures. As shown in Figure 24, Young's modulus, hardening coefficient and initial yield stress reach negligible values for temperatures greater than 1273 K, thereby making their implementation unnecessary. Furthermore, such a simplification improved solution convergence and speed up the simulation. In this case, some phase transformations (i.e. ferrite-austenite), are implicit in the evolution of the thermal properties of the material, while others were not considered in the simulation. However, it has been shown that for low carbon steels, the influence of phase transformations on residual stresses generation is negligible and can therefore be neglected [46], [137], [138].

The entire thermo-structural numerical simulation was performed using Ansys APDL vers. 19.2 with an eight nodes hexahedral element: a SOLID70 element with nodal temperature as the only degree of freedom was used for the thermal analysis and SOLID185 element with spatial displacements as degrees of freedom (i.e.  $x$ ,  $y$ ,  $z$  directions) was used for the structural analysis. As shown in Figure 46, a finer mesh has been used in the weld bead region (i.e. 1 mm), a transition mesh in the heat affected zone (i.e. 1 mm–3 mm) and a coarser mesh everywhere else (i.e.  $> 3$  mm). The FE-model consists of a total of 96420 elements and 97728 nodes. All notches (i.e. weld root and weld toes) have been modelled as perfectly sharp in order to easily simulate the boundary interface between base and weld bead material when using the *element birth & death* technique. Indeed, simulating weld toes and root radii during a thermal-mechanical analysis would have introduced additional issues regarding the convergence of the model, since a dense mesh around notches and a larger simulation time would have been required. The use of a perfectly sharp notch induces high plastic deformation in a close region around the notch that is not relevant for our purposes. Figure 48 shows both results of radial and hoop residual stresses on the plate surface. They, indeed, present a steep gradient close to the weld bead region<sup>9</sup> as a consequence of the sharp notches. In fact, the thermal-structural model validation has been carried out sufficiently far from notches in order to avoid considering stress intensification effects [136].

Nevertheless, the correct notch geometry was considered during the following fatigue assessment step (i.e. section 6.2) with the introduction of a submodel analysis in order to correctly evaluate the damage parameters.

<sup>9</sup> The weld bead area on the plate has been projected onto the stress surfaces of Figure 48 by means of red lines, the outer line represents the weld toe and the inner line represents the weld root

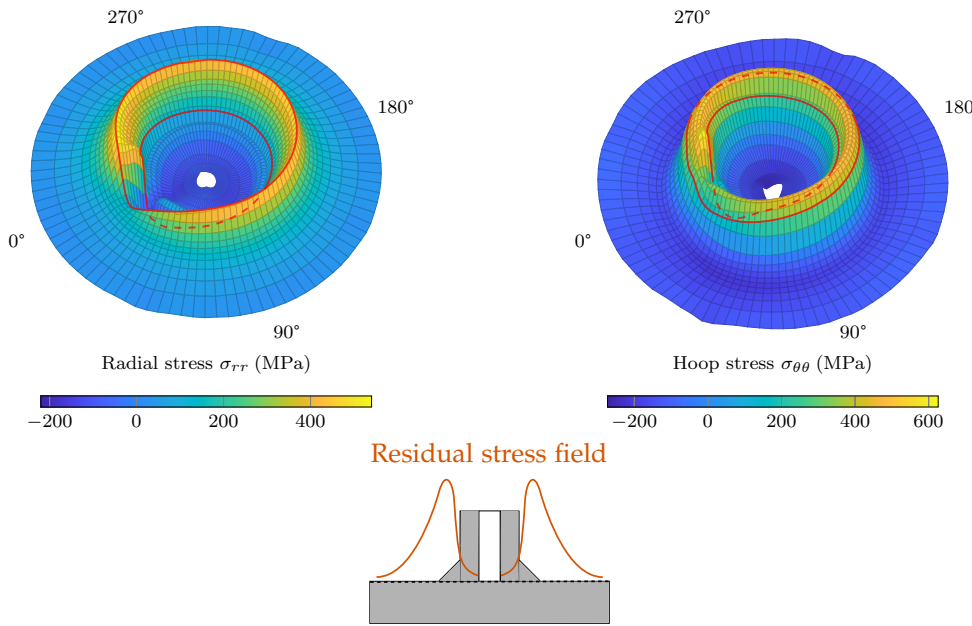


Figure 48: Radial and hoop residual stress on the upper plate surface with indication of the angular coordinate (i.e. run in-run out point at  $0^\circ$ ) and weld bead deposition area (i.e. between red lines); together with a graphical representation of the domain under consideration

## 6.2 FATIGUE ANALYSIS

The fatigue analysis consists of two main parts: a linear-elastic analysis of the entire component subjected to bending or to torsion and a local elastic-plastic analysis, carried out by a submodel. The initial linear-elastic analysis was used to obtain the nodal displacements on the boundary regions of the submodel; besides, to distinguish between AW and SR conditions, residual stresses have been initialized in the submodel for the AW case, while the initialization phase was skipped otherwise.

As shown in Figure 49a, the imposed boundary conditions were two remote forces (i.e. used to simulate the actuators load) and four bolt constraints at the interface between the plate and the crankcase. Both remote force and bolt constraint surfaces have been established in regions sufficiently far from the submodel interfaces, not to cause any effect on the submodel analysis. The linear elastic FE-model reproduces exactly the structural model already discussed in section 6.1. It uses the same mesh pattern and the same element type (i.e. SOLID185), only varying the material properties.

The sub-model geometry (Figure 49b) was defined by means of a sensitivity analysis to ensure a negligible influence of the boundary surfaces on the stress and strain results<sup>10</sup>. The submodel includes the actual fillet radii measured starting from a cross section of the real weld, thus providing a more representative stress gradient at the notches (i.e. 0.2 mm of notch radius for the weld root and weld toe belonging to the base plate and 1 mm of notch radius for the remaining weld toe).

It should be noted that geometric variability is inherent in the welding process. It is therefore impossible to achieve geometric repeatability on the weld seam dimensions. The weld toe and weld root radii, examined during this project, have shown large dimensional variations, sometimes within orders of magnitude. Especially for the weld root, which was experimentally found to be critical for crack initiation, it is sometimes challenging to define even a radius. Within the definition of the numerical model, the smallest radius measured was cautiously taken. Figure 50 shows the heterogeneity of the bead readings and demonstrates the difficulty in finding a single measurement to introduce into the numerical model.

<sup>10</sup> The sensitivity analysis was carried out on nodes belonging to weld root and weld toes, varying the submodel extension angle until no influence on results was exhibited

Elastic-plastic cyclic material properties were implemented in Ansys through a multilinear isotropic hardening material model with stress-strain curve obtained from [139]. The material properties used here refer to a cyclically stabilized curve, as the component was assumed to have been already exposed to a significant number of cycles. The FE-model was characterized by a really fine mesh in all notch regions with an average element size of  $0.05\text{ mm}$  in the weld root and weld toes and an average element size of  $1\text{ mm}$  everywhere else. The submodel had a total number of 155454 nodes and 35408 elements.

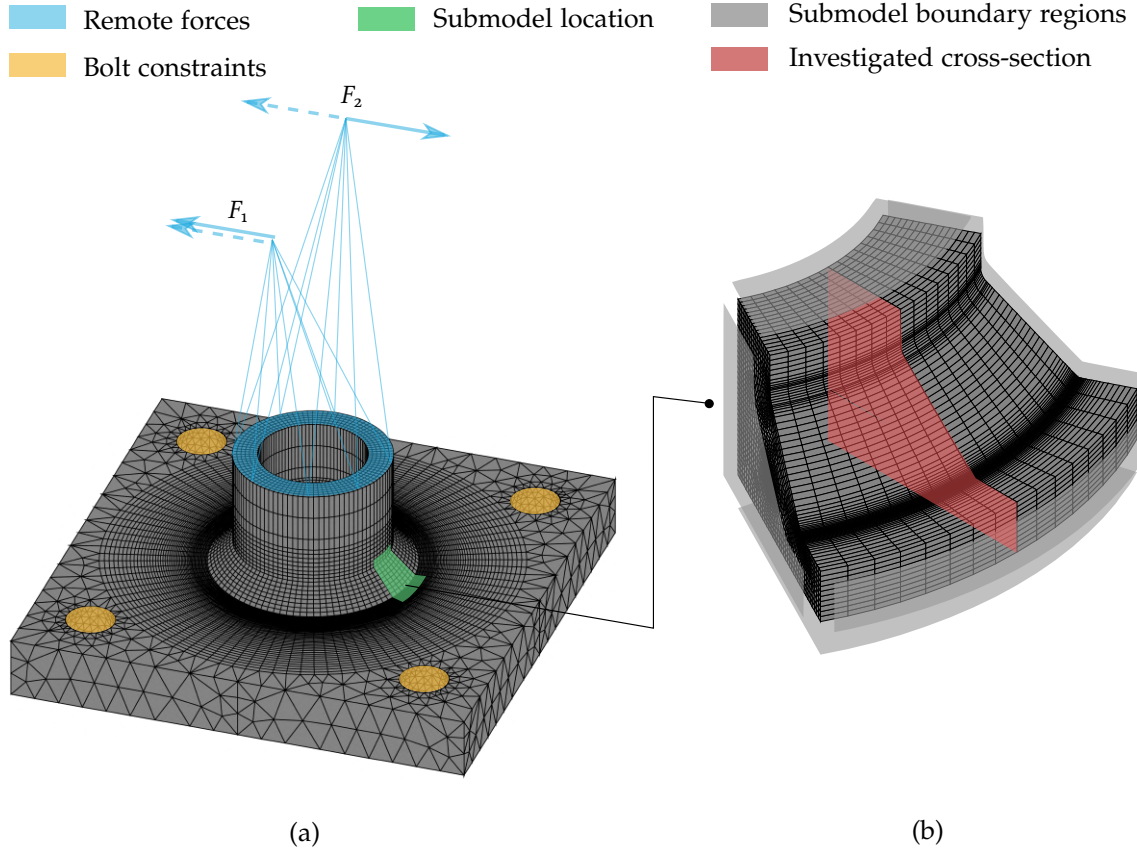


Figure 49: Finite element models for the linear-elastic analysis and elastic-plastic submodel analysis for fatigue damage parameters evaluation

Considering the complex state of stress at the critical locations, it was decided to use a damage parameter that can quantitatively describe the stress triaxiality and consider the material plasticity, as well. All approaches to damage described in the following are based on assumptions of local and continuous mechanics, since it was supposed that most of the time was spent on crack initiation. As reported in [140], specifically for tube-to-plate steel welded joints, more than 80% of the fatigue life was dominated by nucleation and growth in the maximum tangential stress direction if in-phase loading was applied.

Based on the above considerations two damage parameters were used. The first one was based on the critical plane concept of *Fatemi-Socie*, as defined by the following relationship:

$$FS = \frac{\Delta\gamma}{2} \left( 1 + k_{FS} \frac{\sigma_n}{S_y} \right) \quad (29)$$

where  $k_{FS}$  is the material parameter.  $\Delta\gamma$  is the shear strain range,  $\sigma_n$  is the normal stress acting on the critical plane and  $S_y$  is the material yield strength.

Critical plane models were developed as an attempt to explain the experimental evidence that fatigue cracks often nucleate following particular directions; the defect nucleation along specific directions is assumed as a function of the normal and tangential stress and strain component with respect to that

plane.

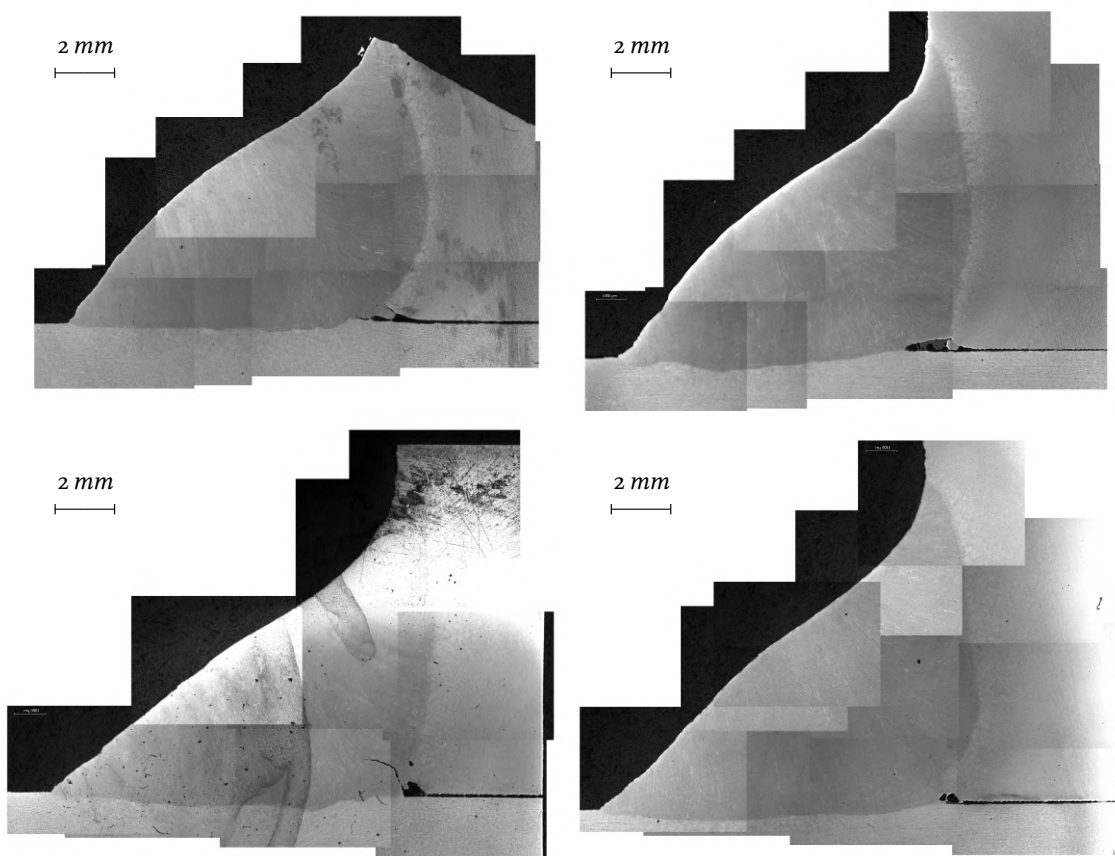


Figure 50: Examples of cross sections of the weld root to highlight shape heterogeneity

Experimental data were reinterpreted by means of the FE-model shown in the Figure 49b, calculating the planes that experiences the maximum value of  $FS$ . A ductile material parameter have been adopted,  $k_{FS} = 0.4$ , in the same way as [141]. As a matter of fact, *Fatemi-Socie* critical plane factor is usually employed for ductile materials and in proportional loading cases [142].

Critical plane factors were evaluated relatively to the cross-section of Figure 49b, which represent the most stressed area during bending loading; on the contrary, all cross-sections are subjected to the same nominal stress state when loaded in torsion. Critical plane factors were computed by implementing Equations 37 in a Matlab code. The AW condition was obtained by mapping residual stresses from the thermal-structural model described in section 6.1. In order to optimize the computation time, the critical plane code was run solely for the nodes belonging to the weld notches. The crack nucleation plane can be predicted by directly applying Equations 37 for all combinations of angles that define the spatial location of the critical plane. Two rotation angles were sufficient to describe the plane position in space, as they completely define the critical plane location according to a local coordinate system. The second damage parameter used was the hydrostatic stress. The hydrostatic stress is, de facto, the average of normal stresses acting on an infinitesimal volume of material and is mainly responsible for the volumetric changes in the part. This parameter is useful to assess the fatigue life of a torsionally loaded component [143], [144]. Hydrostatic stress is directly linked with stress triaxiality that, especially for notched components, plays a major role in the ductile fracture of metals [145]. It has been shown by the work of Crossland [146] and subsequently Burns et al. [147] that a superimposed large hydrostatic pressure has a significant effect on torsional fatigue life since a large compressive normal stress component is introduced in the planes of maximum tangential alternating stress.

### 6.3 NUMERICAL RESULTS

A preliminary analysis was performed to identify the specimen critical notch in order to perform the subsequent fatigue numerical study. Hydrostatic stress and the *Fatemi-Socie* critical plane factor were used as damage factors for the analysis.

Figure 51 shows the hydrostatic stress and *Fatemi-Socie* critical plane factor for different loading and heat treatment conditions. It is visible that under pure bending the difference in damage between AW and SR states is smaller if compared to the case of torsional loading. A possible explanation for that involves the type of loading. In the presence of pure bending, residual stresses undergoes plastic relaxation during the first loading cycles leading to a stress redistribution that results in similar hydrostatic and deviatoric stress tensor components for the AW and SR states. The opposite is true in the case of pure torsion, in this case the load has less influence (i.e. ideally no influence) on the hydrostatic component, whereas for the AW specimen, due to residual stresses, a significant hydrostatic stress component may be present after specimen loading.

When hydrostatic stress is considered, the weld root appears as the critical notch showing an higher difference between AW and SR cases when it comes to the torsional loading.

Likewise, FS critical plane factor identifies the weld root as the critical notch and shows the characteristic difference between torsional and bending load under different heat treatment conditions. It is possible to identify from Figure 51 how the FS damage factor reports the highest values within the weld root, showing a significant difference between AW and SR conditions only in case torsional loading condition.

Subsequently, the damage resulting from different loading conditions in AW and SR states was evaluated by directly comparing the maximum values of the critical plane factors as a function of the applied nominal stress range. It should be noted that in the following, only measurements involving the weld root will be reported, as it was identified before as critical notch. The analysis has been carried out with respect to pure bending, as shown in Figure 52, and with respect to pure torsion, as shown in Figure 53. The graphs provide results for the *Fatemi-Socie* critical plane factor over the nominal stress range. The relative error between the AW and SR conditions (scale on the right vertical axis) has also been reported. The relative error reaches a maximum value of 8.3% in pure bending for a nominal stress range of 108 MPa–191 MPa, while it goes up to 41.1% in pure torsion for a nominal stress range of 188 MPa–282 MPa<sup>11</sup>. The relative error never exceeds 10% for the case of bending loading, while it always exceeds 20% for the case of torsion loading. It should be noted that the quasi-linear behaviour obtained in Figure 52 and Figure 53 results as the material stabilised after the initial fatigue cycles. Actually, critical plane factors were taken as the convergence values obtained during numerical analyses (i.e. convergence was obtained in most cases after few load cycles). It is worth noticing that, critical plane parameters are not representative of the specimen loading condition, which is why the same critical parameter results in clearly different nominal stresses ranges between AW and SR conditions. This can be concluded by looking at Figure 52 and Figure 53, where the same critical parameter yields different values of nominal stress ranges, particularly in the case of pure torsion.

---

<sup>11</sup> The adopted nominal stress ranges for bending and torsion were chosen to be consistent with the experimental fatigue behaviour of the specimens in as-welded conditions. Both stress ranges yield to an experimental fatigue life range  $10^5$ – $10^6$ .

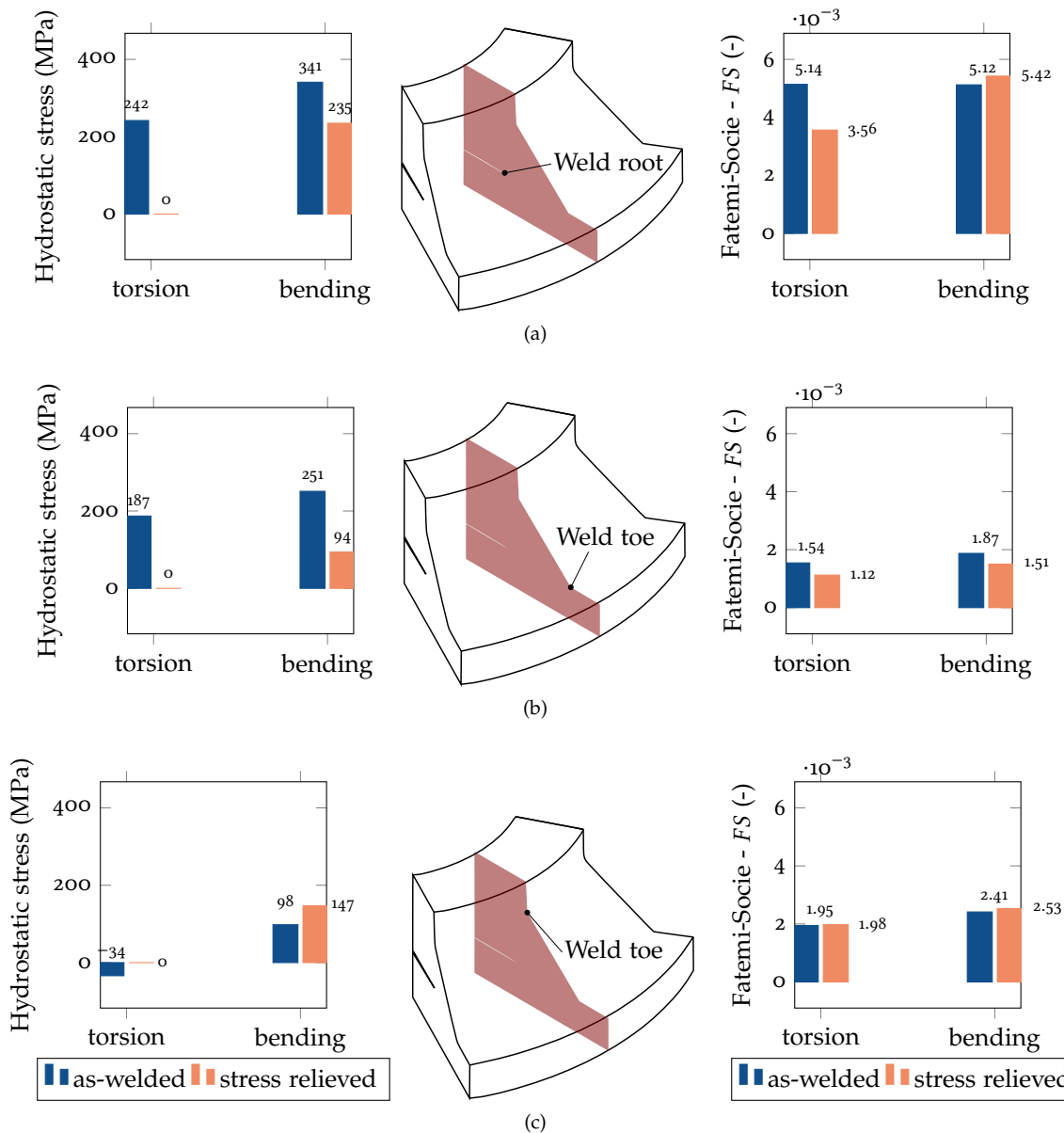


Figure 51: Pure bending and pure torsion hydrostatic stress and *Fatemi-Socie* critical plane factor in the weld root (a) and weld toes (b, c); hydrostatic stress and critical plane factor values are related to a nominal stress range of 143 MPa in bending and 250 MPa in torsion

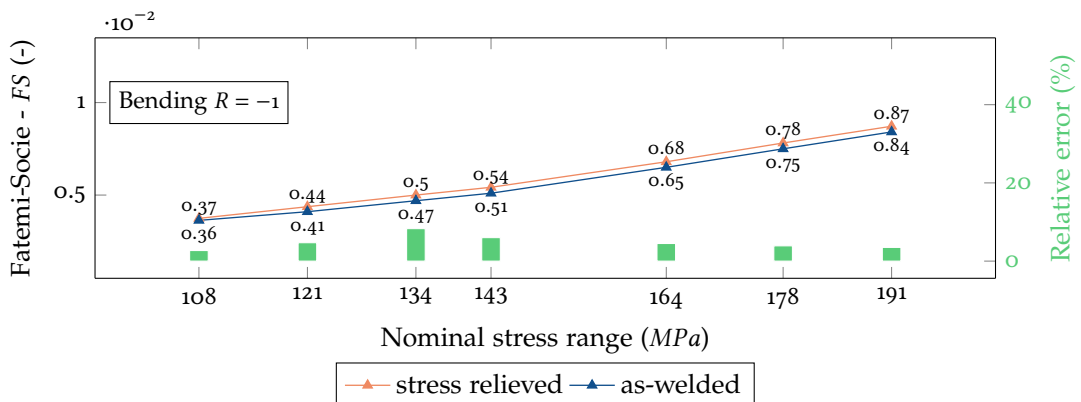


Figure 52: Fatemi-Socie critical plane factor over nominal stress range under pure bending for a load ratio  $R = -1$

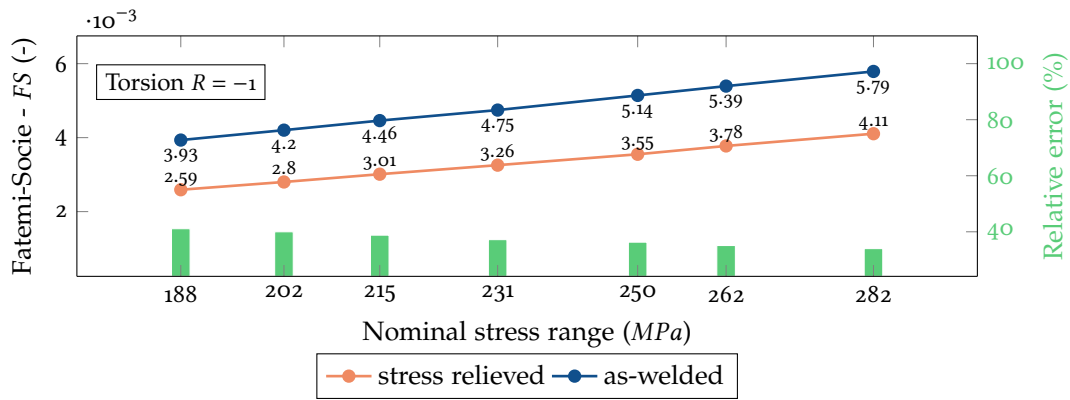


Figure 53: Fatemi-Socie critical plane factor over nominal stress range under pure torsion for a load ratio  $R = -1$

Figure 54 presents the endurance curves in terms of critical plane factors vs. experimental number of cycle to break-trough. Data of  $FS$  over the experimentally evaluated number of cycles to break-trough are shown for all loading and heat treatment conditions.

In this case, as the damage factor considered is a local damage parameter, all data were represented on a single plot. Since the calculation of the AW data derived from the implementation of the numerical thermal-structural model, uncertainty in the damage factor calculation could arise. For this reason, solely the fitting of the SR points was reported and used for the evaluation of the *expected vs. experimental number of cycles to break-through* graph as it was considered to be representative for the whole distribution.

It can be observed that no clear distinction between pure torsion loading and pure bending loading exists as occurred under nominal stresses. This is mainly caused by the local definition of the damage parameter, which accounts not only for the loading condition but also for the local geometry of the component as well as residual stresses.

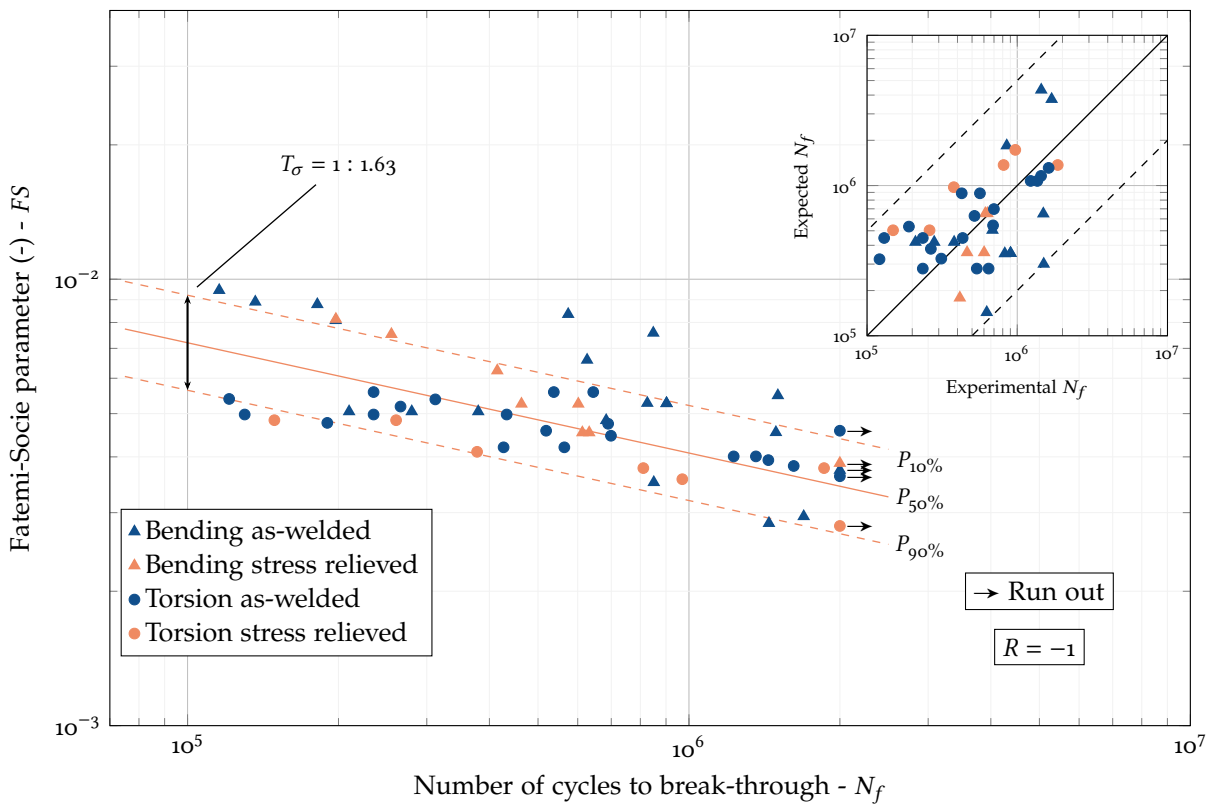


Figure 54: Fatemi-Socie critical plane factor over the number of cycles to break-through for pure bending and pure torsion loading in as-welded and stress relieved conditions

#### 6.4 CONCLUSION

In this chapter it has been shown how an effect of residual stresses on the fatigue life of a welded pipe-plate joint exists. The comparison of Fatemi-Socie damage parameters and hydrostatic stress in case of torsion and bending loading in AW and SR conditions shows that there is a clear difference in damage during torsion loading, while no difference was found during bending loading. The use of hydrostatic stress as damage factor indicated that the torsion load is not able, even in the presence of a notch, to modify the initial residual hydrostatic stress state. This therefore leads to a difference in the damage between AW and SR.

In order to gain more insight into the damage process due to residual stresses, an equivalent specimen geometry will be presented in the next chapter.



# 7

## RESIDUAL STRESSES INFLUENCE ON THE FATIGUE STRENGTH OF STRUCTURAL COMPONENTS

Considering the complex analysis that was needed, both experimentally and numerically, for the fatigue assessment of the welded joint, a preliminary numerical study was performed in order to design a simplified equivalent specimen geometry.

### 7.1 MATERIAL AND METHOD

In order to achieve a comparable behaviour as the welded specimen, a notched geometry was taken as a reference, thereby aiming in achieving similar notch stress gradients. Investigations of the fracture surfaces of the welded joint showed how the weld root represents the critical location of the joint for both types of loading, as already presented in Figures 42 and Figure 41. Optical microscope measurements of the weld root radius (i.e. whenever possible) identified an average dimension of  $0.2\text{ mm}$  and a virtually null opening angle Figure 55a. In view of the experimental limitations (i.e. the availability of cutting tools) to be considered for a future step of specimen manufacturing, it was decided to create a notch geometry with a radius of  $0.2\text{ mm}$  and an opening angle of  $35^\circ$  (Figure 55b). Furthermore the specimen was design with a maximum outer diameter of  $22\text{ mm}$  and a notch diameter of  $16\text{ mm}$ .

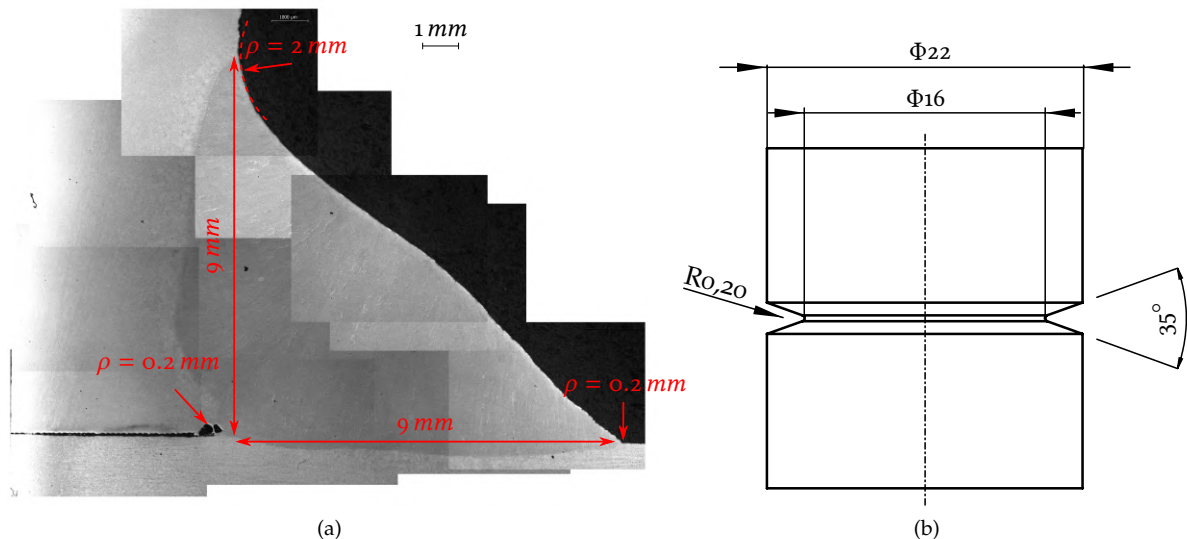


Figure 55: Weld seam cross section dimensional analysis (a), and dimensions of the notch specimen based on the weld root radius evaluation (b)

In the case of the notched specimen, the *as-welded* state (i.e. in presence of residual stresses) was characterised by a pre-compression followed by load releasing process resulting in a tensile residual stress state around the notch. This is the simplest and most direct way to induce residual stresses. Unlike the case of the welded joint where residual stresses were introduced by means of thermal processes, in this case plasticisation of the material was used instead.

### 7.2 FINITE ELEMENT MODEL

In order to achieve comparable residual stress conditions to the welded joint, different notched specimen geometries were designed in Ansys (Figure 56). The size of the notch resembles that of the weld root, thus obtaining a similar-sized plastic region. To carry out an exploratory analysis on residual

stress generation, a preload method was investigated. With this method a compressive preload was used to obtain tensile residual stresses in the vicinity of the notch. This loading mode was used together with torsion and traction/compression fatigue loading.

A 2D model (Figure 56b) was developed to investigate combined static and tensile/compression fatigue loading, while a 3D model (Figure 56a) was developed for the combined static and torsional fatigue loading. The numerical models used elastic-plastic material properties obtained from tensile tests carried out S355JR specimens, as shown in Figure 57. Both finite element models used quadratic elements, in particular the 3D model implemented 93240 elements and 389175 nodes, while the 2D model implemented 4090 elements and 12417 nodes.

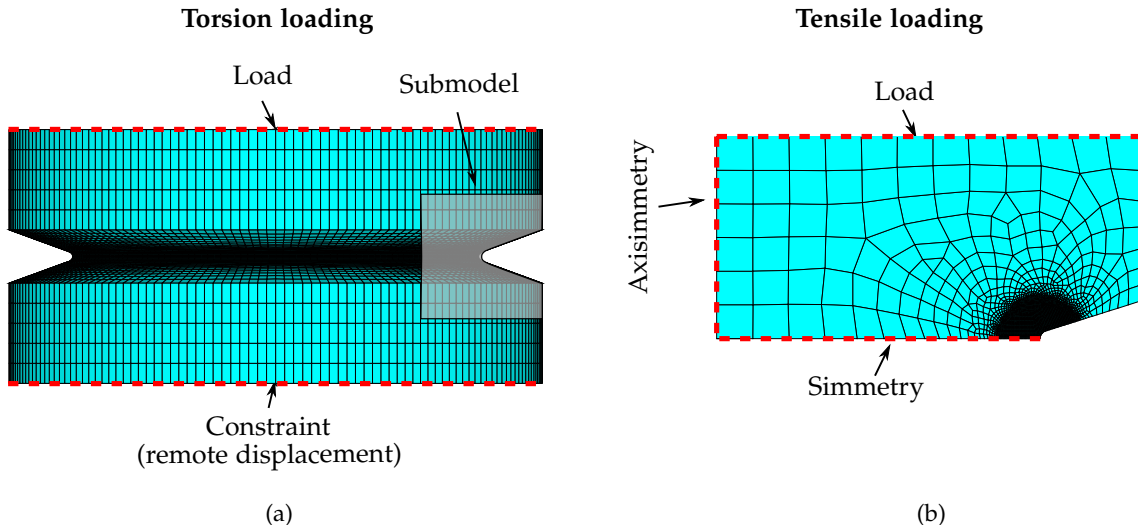


Figure 56: 3D finite element model of the notched specimen used for simulating torsional loading (a), 2D finite element model of the notched specimen used for simulating traction/compression loading (b)

The 3D model used linear-elastic material properties and employed boundary conditions of totally fixed remote displacement of the bottom face (i.e. to allow free Poisson's contraction) together with a load (i.e. force or torque) based on the type of analysis to be performed. Subsequently, the elasto-plastic material properties were introduced in a submodel analysis in order to derive the variables of interest in the vicinity of the notch only.

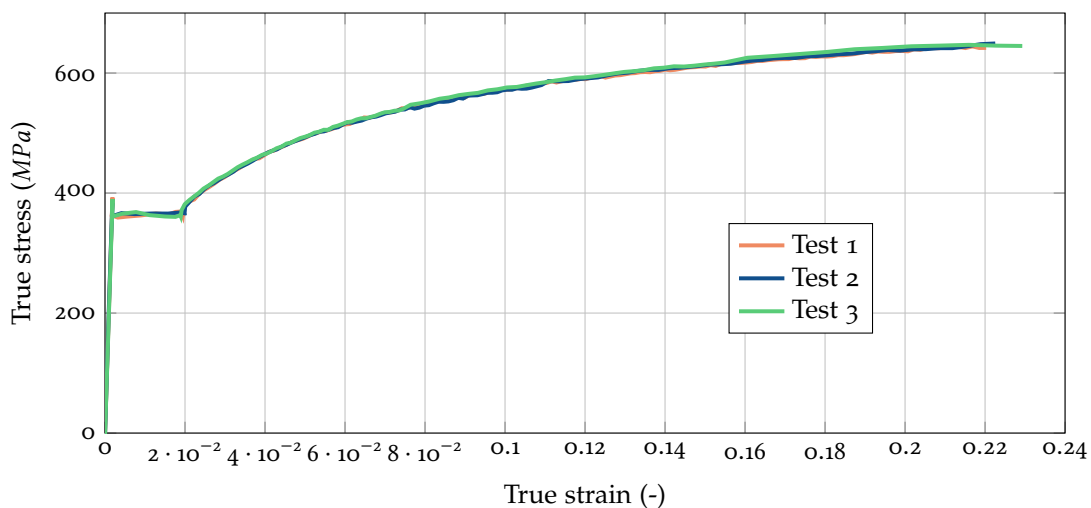


Figure 57: True stress and strain results obtained from three tensile tests performed on S355 structural steel specimens

The 2D model, on the other hand, directly utilises elasto-plastic material properties, symmetry conditions on the bottom face, axisymmetry with respect to the axis and loading force only applied along the axisymmetry plane.

### 7.3 RESULTS

In the following section, numerical results deriving from the finite element models presented before and in chapter 5 are provided. Figures 58–61 show the hydrostatic stress variation over the crack path for the welded joint (Figure 58 and Figure 60) and notched specimen (Figure 59 and Figure 61).

Figure 58 and Figure 59 represent the effect of a pure torsion load. It can be seen that under null preload (i.e. orange lines), the hydrostatic stress value is always close to zero (i.e. nominally zero). It should be noted that in case of notch specimen the AW and SR refers to specimen with preload or without respectively. If preloaded but before applying the fatigue loading, the specimen shows a pattern of hydrostatic stress (i.e. red dashed lines).

After an iterative analysis on preloading force values, a force of  $-35 \text{ MPa}$  was identified as the one to achieve a similar maximum hydrostatic stress value of  $246 \text{ MPa}$ , as found at the welded root.

It is evident how the values of initial hydrostatic stress were scarcely affected by the pure torsional load in both cases of notch specimen and welded joint (i.e. as can be seen comparing blue and dashed red line of Figure 58 and Figure 59). It can therefore be assumed that, based on the hydrostatic stress values, the configuration with preload is more critical respect to the configuration without preload, if pure torsional loading is considered.

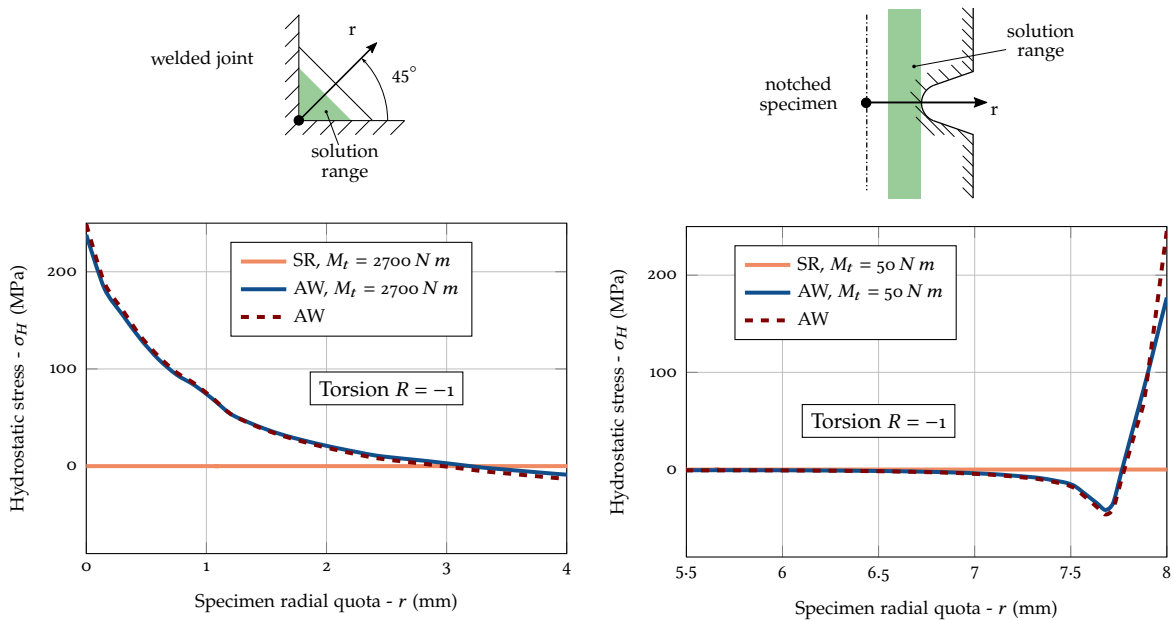


Figure 58: Hydrostatic stress for a pipe-to-plate welded joint over the crack path starting from the weld root; AW and SR conditions, before and after torsional fatigue loading are shown

Figure 59: Hydrostatic stress for a notched specimen over the notch section; AW and SR conditions, before and after torsional fatigue loading are shown

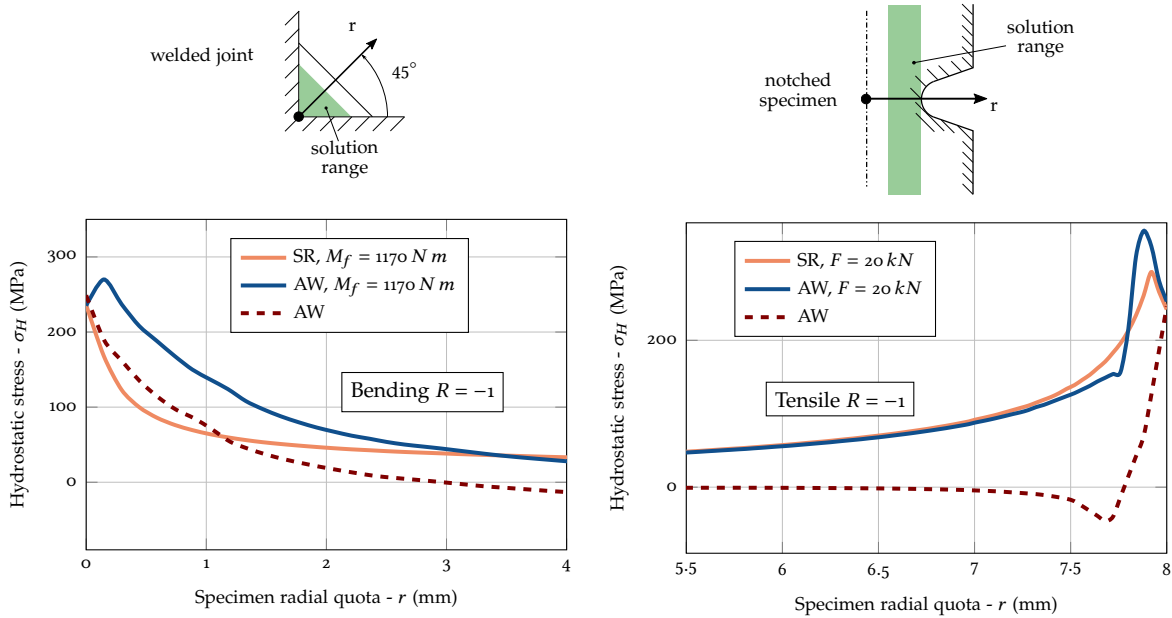


Figure 60: Hydrostatic stress for a pipe-to-plate welded joint over the crack path starting from the weld root; AW and SR conditions, before and after bending fatigue loading are shown

Figure 61: Hydrostatic stress for a notched specimen over the notch section; AW and SR conditions, before and after tensile fatigue loading are shown

In contrast, with bending (Figure 60) and traction/compression loading (Figure 61), the hydrostatic stress field generated by the preload is affected by the fatigue loading. It should be noted that, the difference in hydrostatic stress considering the configurations with and without preload under fatigue loading is smaller if compared to the pure torsion configuration. This means that the load in this case affects the residual stress field produced by the preloading and that therefore the conditions with and without preload become similarly critical. Naturally, these considerations have been done by incorporating material plasticity within the numerical simulations and accounting for a sufficiently large number of fatigue cycles in order obtain a stabilise material behaviour.

#### 7.4 CONCLUSION

By using a notched geometry, it was possible to achieve similar results to those obtained with the welded joints. Also in this case it was shown that a residual stress field is more damaging if the component is loaded in torsion. A possible explanation consider the hydrostatic stress as damage factor. The hydrostatic stress field introduce a degrading effect when residual stress are present only for the torsionally loaded component. In fact, if tensile load is able to modify the initial residual hydrostatic stress this is not true for the torsional loading. Therefore, the hydrostatic residual stress field remains unaltered throughout the whole component life, resulting in greater damage than the component without residual stress.

# 8

## CONCLUSION

---

The work presented in this thesis investigates in detail a welding process on a pipe-to-plate welded joint with subsequent fatigue life analysis of such component. Both numerical and experimental analyses have been carried out, in order to obtain extensive knowledge of the residual stress generation process and its effect on the fatigue life. In the following, the relevant conclusions are provided for each chapter followed by general remarks.

In the first part of this work ([chapter 3](#)), the [FEM](#) was employed to conduct a thermal numerical analysis for a pipe-to-plate welded joint. Three different methods for the simulation of thermal heat source were applied, i.e., constant initial temperature assigned to a given volume of elements, constant heat flux, and the Goldak's double-ellipsoid model. The methods require a different number of parameters to be set for the analysis. First of all, a sensitivity analysis on several parameters showed that thermal conductivity and heat capacity had a noticeable effect, while the influence of the other parameters on the output was negligible. Thereafter, it was shown that even the most simple numerical model [CIT](#) can be used to reasonably reproduce the thermal history close to the weld bead. With a proper choice of the initial temperature, the results were very similar to those obtained by the most sophisticated Goldak's double-ellipsoid model, whose accuracy has been already discussed in different studies. In general, results show that a negligible discrepancy in the temperature history can be obtained using the different models if the governing parameters are properly set. Consequently, the [CIT](#) model was adopted as the main procedure to simulate the welding process. The use of the [CIT](#) method reduces the number of parameters that have to be established, leading to a time-saving thermal study that describes a fairly similar thermal behaviour as compared to more complex methods. In order to correctly set the [CIT](#) thermal model for the subsequent structural analysis, experimental temperature measurements obtained during the welding of an equivalent specimen were adopted. It must be noted that the initial temperature described in this paper, as well as the other methods, only applies for the specific case analysed in this work; different setting-parameters have to be determined for different welded joint geometries.

In the second part of the work ([chapter 4](#)), numerical and experimental data of relaxed strains and residual stresses have been presented and discussed for a welded pipe-to-plate joint. Experimentally, it was found that relaxed strains measures are intrinsically affected by experimental errors. A reproduction of the experimental readings between different samples seems to be a difficult task; it is therefore necessary to deal with a degree of uncertainty during the experimental readings. Numerically, uncoupled thermal-structural simulations were used, as they allow great flexibility on both the implemented thermal and structural models, leading to a very flexible simulation of the welding process. The comparison between experimental and numerical results of relaxed strains pointed out how the thermal model employed ([CIT](#)), although its simplicity, once calibrated, it can provide fairly good results also from a structural point of view. In fact, used together with the [RWP](#), they present an accurate description of the actual weld seam stiffness during the cooling process. Furthermore, the significant variations in residual stresses near the run in-run-out point is a further indication of the inaccuracy of a two-dimensional modelling of the welding process often found in literature. The obtained results seems significant for the field, since residual stresses are considered to have a detrimental effect on the fatigue strength of welded components.

In the third part ([chapter 5](#) and [chapter 6](#)), the influence of residual stresses on the fatigue life of the pipe-to-plate welded joint was discussed when subjected to different types of loading. Experimental results, obtained by means of fully reversed bending and torsion tests up to specimen failure, were discussed on the basis of numerical data, considering both the Fatemi-Socie critical plane factor and hydrostatic stress. Experimental fatigue tests have clearly proved an effect of residual stresses on the fatigue behaviour of the studied component when loaded in torsion. In contrast, no significant influence was detected for specimens loaded in bending. Nevertheless, for both loading cases, the experimental results obtained with the stress relieved specimens appear to have a significantly lower scatter, when compared to the results obtained with the as-welded specimens. Both the Fatemi-Socie critical

plane factor and the hydrostatic stress exhibited common behaviour in describing bending-loaded and torsion-loaded as-welded and stress relieved conditions. In particular, the hydrostatic stress showed null values for the torsionally loaded stress relieved samples, while, as a result of the residual stress field, it gained non-zero values for the as-welded samples. Furthermore, the implemented thermal-structural model proved to be reliable and to provide effective stress cycles that appeared to be in agreement with the experimental results from the fatigue prediction point of view.

In the fourth part ([chapter 7](#)), a notched geometry was design in order to replicate, in a more controlled way, the residual stress gradient obtained as a result of the welding process. In order to better understand the outcomes obtained from the welded joints, an exploratory study was carried out on specimen geometry and the preload necessary for obtaining the correct residual stress field in the notch geometry. The results showed that, if hydrostatic stress is used as damage parameter, a larger difference in damage between the as-welded and stress relieved states was obtained when a pure torsion load was considered rather than a tensile load. This outcome is consistent with damage parameters evaluated in [chapter 5](#), showing how the influence of residual stress on the fatigue life of different components is dependent on the type of load implemented.

This research work has attempted to advance the knowledge about the effect of residual stresses on the fatigue life of welded components. In addition, it also identified some interesting aspects and provided suggestions on the numerical modelling of these processes. However, it is not intended to be exhaustive; rather, it is supposed to provide useful insights for future research in this field.

The study of welded joints still presents a number of open questions, mainly associated with the side effects of the welding process itself. It is still challenging to correctly account for residual stresses in structural evaluation criteria, even though many numerical and experimental methods exist for their assessment. Furthermore, the high variability associated with the size of the notches in a welded joint makes it difficult to rely on the measurements obtained, whether numerical or experimental. Using experimental calculation methods, it is often difficult to evaluate residual stresses close to the weld notches (i.e. weld root and weld toe), while numerical methods often have simplified input parameters (e.g. geometry, material properties, process model, etc.) which in any case throw uncertainty on the results. The combined use of numerical and experimental methods is therefore of fundamental importance, but requires large investments in terms of time and money.

In fact, although this work has studied the residual stress generation process in detail, this is not usually feasible in an industrial environment. Only in the research field the necessary time needed to develop complex numerical thermostructural analyses can be invested. Complex thermostructural numerical simulations require a high level of computational effort and time to solve the models. To date, the structural evaluation of welded joints is mainly based on standard methods that consider residual stresses and other defects by means of large safety factors. Indeed, the key aspect consists in the impossibility to generalise the residual stress field and thus ad-hoc measurements for each sample/component are generally required. The generation of residual stresses depends not only on the process but also on the geometry of the part.

Residual stresses study, although existing for more than a century, is still an open research field. Further research is needed to obtain effective and general methods for considering residual stresses and their degrading effects on structural components.

**Part III**  
**APPENDIX**



# A

## COMPARISON BETWEEN BI- AND TRI-DIMENSIONAL FINITE ELEMENT MODELS WITH ELASTIC PLASTIC AND LINEAR ELASTIC MATERIAL PROPERTIES

---

### A.1 FINITE ELEMENT ANALYSIS

The following appendix present a preliminary analysis on the comparison between bi- and tri-dimensional finite element models employing elastic plastic and linear elastic material properties for the simulation of the welding process already presented in [chapter 3](#), [chapter 4](#) and [chapter 6](#).

The commercial software Ansys was used for the following analysis. The numerical simulation consists of an uncoupled thermal-structural full transient analysis. The use of an uncoupled formulation is due to a negligible dimensional variation of the component during welding that leads to negligible temperature variations.

The simulations were carried on by means of thermal and structural steps, independently solved. Anyway, the analysis was structured in a way to consider the transient temperature field acting on the stress, through the thermal expansion coefficient and the thermal-mechanical temperature dependent properties, as already presented in [chapter 3](#), [chapter 4](#) and [chapter 6](#). The first step of the analysis consists of a heat conduction problem followed by a structural analysis where the specimen thermal history was applied as a load. The problem is intrinsically asymmetric due to the welding procedure, and for this reason, a 3D model was involved in the analysis. The purpose of the 3D model was to get the stress and strain fluctuation along the hoop direction. However, the 3D model required a very high computational effort because of its non-linearities; for this reason a 2D model was developed as well. A 2D model is easier to manipulate and optimize by varying its parameters, resulting in faster development of the procedure; an example of the two finite element models is shown in figure [62](#). Phase transformation effects were not considered to avoid over complicating the analyses, as the purpose was purely a comparison between different models parameters. However, temperature dependent thermal-mechanical material properties were included.

With reference to the specimen geometry, some assumptions were introduced in the FE-models:

- the weld seam geometry was simplified by a triangle, even if during the real process part of material flows towards the plate because of the gravity, as shown in Figure [62](#);
- the *element birth and death* method was used to approximates the real process; this is usually adopted for FE-simulations of the welding process (some examples are reported in [\[20\]](#), [\[114\]](#), [\[116\]](#));
- cooling of the molten material is simulated by a [CIT](#) method instead of a volumetric heat flux. This hypothesis is due to easier controllability of the nodal temperature, as explained in [chapter 3](#).

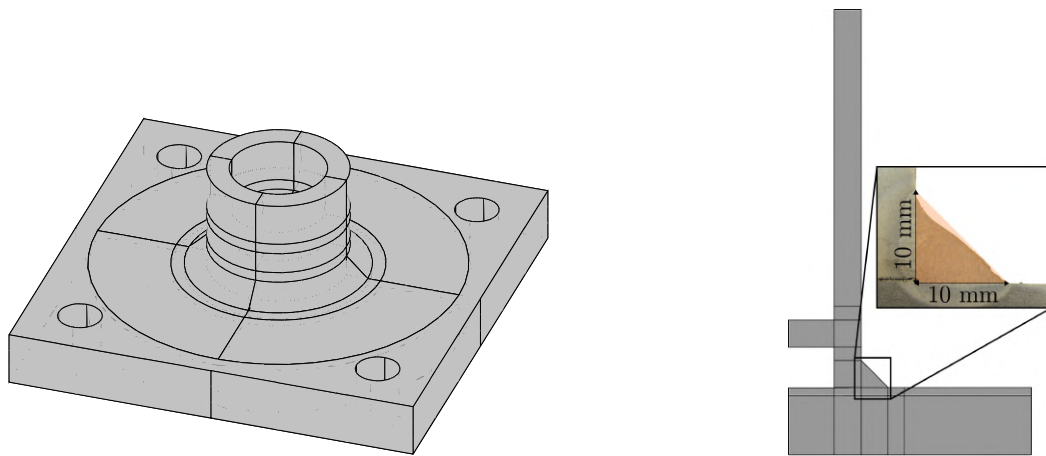


Figure 62: 3D and 2D FE-models

#### A.1.1 Thermal analysis

The thermal analysis is a transient non-linear simulation. A PLANE55 element was used in the 2D model, having four nodes and temperature as the only degree of freedom. The element SOLID70 was employed in the 3D model; it is a brick element with eight nodes and temperature as degree of freedom.

The load was defined by applying a fixed initial temperature ( $T_i$ ) at all the welding seam nodes. Essentially  $T_i$  was chosen in two different ways: the melting temperature of the base metal (i.e. the temperature at which the molten metal is expected to be in contact with the plate,  $T_i = 1673\text{ K}$ ) or the temperature found by infra-red scanning of the welding process done by Farson et al. [148] ( $T_i = 3273\text{ K}$ ). All the remaining nodes were initialized at the room temperature  $T_0 = 293\text{ K}$ .

The temperature dependent thermal material properties were collected from Bhatti et al. [19]. Both convection and radiation were considered constant during the simulation; the convection was set to a value of  $21\text{ W m}^{-2}\text{ K}^{-1}$ , while the radiation was set at 0.79 at ambient temperature. The convection is significant for lower temperatures than radiation, instead, for temperatures close to the material melting point, radiation is more significant.

#### A.1.2 Structural analysis

Similarly, even the structural analysis is a transient non-linear simulation. The same mesh and geometry of the thermal simulation were employed. A PLANE182 element was adopted for the 2D model, while the SOLID185 was used for the 3D one. In this case, the displacement at the nodes were the degree of freedom, i.e. two degrees of freedom (x-y) for the four nodes PLANE182 and three degrees of freedom (x-y-z) for the 8 nodes SOLID185.

The welding was executed by rotating the tube and plate around the tube axes, leaving the component free to move. Because of this, in the FE-model only the upper tube surface was fixed in the radial and hoop directions. Although the Boundary Conditions (BC's) were not related to the real process constraints, these were aimed to leave the specimen free to move in the weld region. Basically, the edge effect given by the constraints was dissipated in less than a tube thickness and, as regards the effect of the BC's on the stress-strain field, this is negligible.

Likewise, the thermal simulation, the *element birth and death* technique was applied with the same sequence to simulate the welding process. The load consisted of a thermal body force applied at each node for each time-step. The temperatures were obtained from a binary file resulting from the thermal simulation. Through the thermal expansion coefficient, the software calculated the deformation of each element. It was necessary to define two different materials reference zero strain temperatures: a material for the tube and plate with a reference temperature of  $293\text{ K}$ , one material for the weld seam with a reference temperature of  $1673.15\text{ K}$  or  $3273\text{ K}$  respectively.

The thermal expansion coefficient was taken from Bhatti et al. [19], while a multi-linear elastic-plastic

material law developed by Chen et al. [149] was implemented. The Poisson's ratio was kept constant at a value of 0.3. In general, it is common not to consider its variation during these analysis [19], [45], [47], [150].

## A.2 RESULTS AND DISCUSSION

Different simulations were carried out during this study as described below.

Strain measurements in radial direction were used, according to Table 9. Furthermore, results from 2D and 3D numerical analysis were evaluated and compared.

As it can be seen from figure 63 and figure 64 both temperature and material properties have been found to be parameters of influence for the numerical analysis.

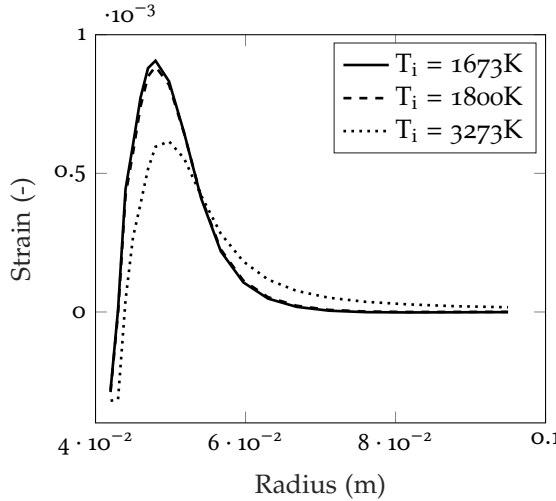


Figure 63: 2D simulation results comparison for different initial temperatures ( $T_i$ ) of the welding seam.

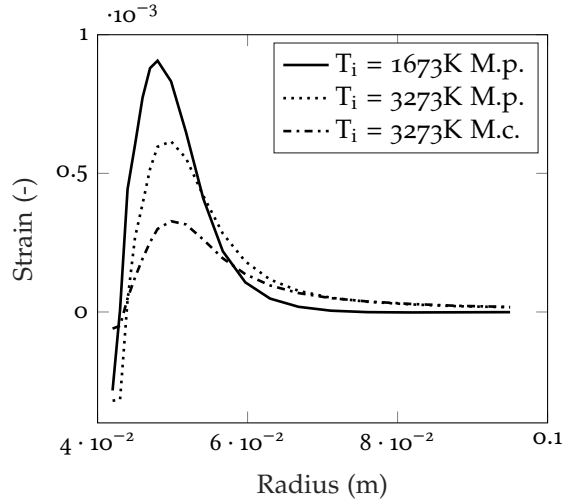


Figure 64: 2D simulation results comparison for different initial temperatures  $T_i$  and material properties (M.p. = Partial multi linear elastic-plastic, M.c. = Complete multi linear elastic-plastic)

Figure 63 shows the strain resulting from the difference between the strain obtained after holes cutting and the strain obtained after cooling, this for different  $T_i$  of the welding seam. It can be noticed that, as the starting temperature increases, the maximum residual strain decreases. A higher  $T_i$  heats up more material around the welding seam, however, the volumetric changes resistance of the material is weakened by the poor material properties at high temperature, leading to lower stresses and strains. For instance, figure 64 can be explained in the same way; where "M.p." refer to a partial set of multilinear elastic-plastic temperature dependent material properties (i.e. they are described until a temperature of 933 K), while "M.c." refers to a complete set of multilinear elastic-plastic temperature dependent material properties (i.e. the complete set used by Chen et al. [149]). In this case, the use of a complete set of elastic-plastic material properties further weakens the resistance of the material for volumetric changes. Basically, when the material is at temperatures higher than 933 K, the numerical program implements much lower yield strength and elastic modules that lead to lower residual strains.

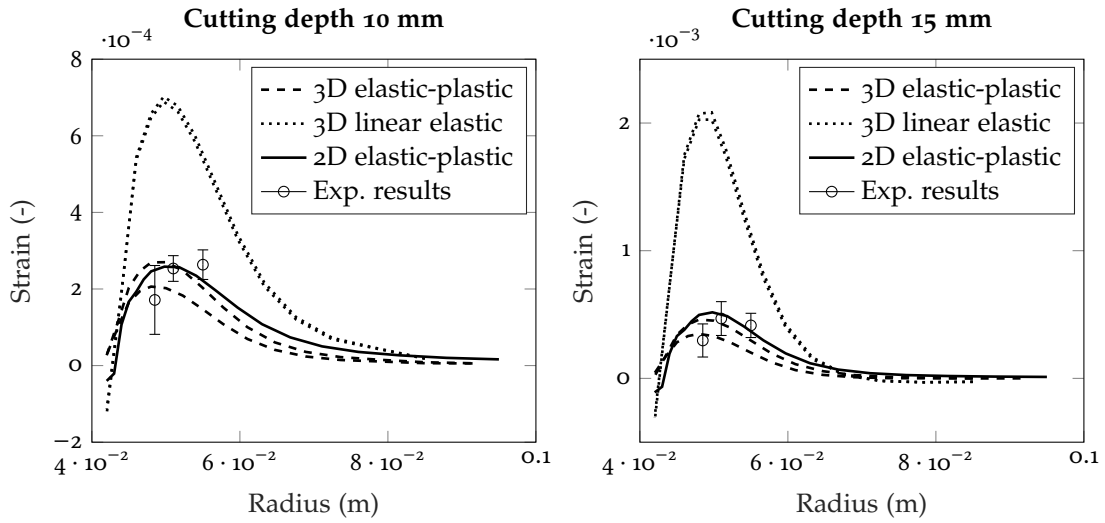


Figure 65: Comparison between numerical and experimental results for different cutting depth.

In figure 65 all the main results are shown. All the results are obtained for an initial welding seam's temperature of  $T_i = 1673 K$ . In particular, the 3D analyses reported the entire range of strain solutions caused by the stress and strain variance along the circumference. It can be noticed that the variation between the maximum and minimum strain is not remarkable for the linear-elastic 3D simulations. Actually, for the 3D linear elastic analysis, the maximum relative percentage difference between the maximum and minimum strain is 2.7%, while for the elastic-plastic model is 26%.

The experimental results are described through the mean value and standard deviation of all the specimens for different radius.

The 3D linear elastic simulation with temperature dependent material properties overestimates the experimental results as expected. The 3D and 2D elastic-plastic models with temperature dependent material properties lead to a better result compared the previous one.

On average, the 2D simulation is easier to setup. However the 3D analysis allows greater control over input parameters, considering the additional parameters with respect to the 2D simulation, such as the total welding time, the *element birth and death* method and the starting weld seam temperature.

# B

## ANALYTICAL MODELS FOR EVALUATING RESIDUAL STRESSES

In this appendix two analytical standard solution are adopted (i.e. membrane-plate, Williams) and the theory behind them is discussed and developed based on the assumptions required to describe the investigated pipe-to-plate welded joint. The idea underlying this theory assumes the residual stress field mainly generated by the shrinkage process of the weld bead during its cooling, as shown in Figure 66.

The axisymmetric membrane/plate theory combined with Williams' solution has been developed in order to provide an approximate analytical model of the stress field produced by a weld seam shrinkage.

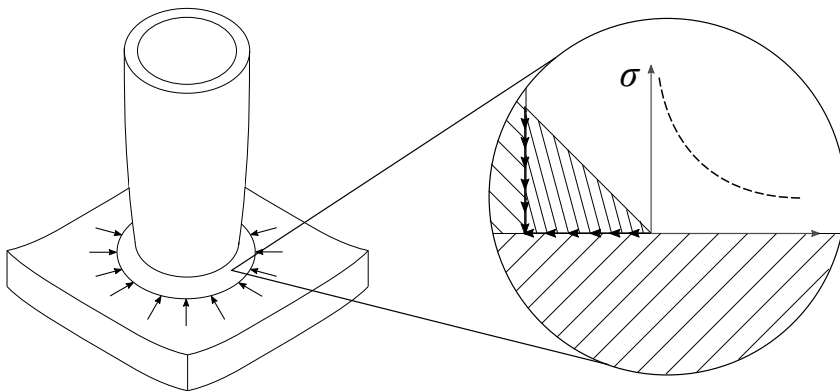


Figure 66: Weld seam shrinkage effect on the global deformation of the component

### B.1 MEMBRANE-PLATE & WILLIAMS THEORIES

The analytical axysimmetric membrane-plate solution was investigated to determine an approximate analytical model to describe residual stresses generated by a circular welding process. Overall, the developed model consists of two main solutions combined together:

1. membrane-plate solution was used to approximate the stress behaviour in a region far from the weld seam;
2. Williams' theory for sharp notches was employed in order to characterize the stress singularity due to the weld notch.

Figure 67 graphically summarizes the method explained above, showing the parameters of interest for the models employed. A cylindrical coordinate system  $\{r, \theta, z\}$  was introduced to describe the membrane-plate model, together with the parameters of plate thickness  $h$ , internal and external plate radius  $a_1$  and  $a_3$  and the radius  $a_2$  of load application<sup>12</sup>.

Regarding Williams' theory the necessary entities are a local polar coordinates  $\{r_w, \psi\}$ , the crack opening angle  $2\zeta$  and the governing parameter  $\zeta_S = \pi - \zeta$ , as already presented in Figure 6.

It is worth noting that the membrane-plate theory does not account for the existence of a notch, for this reason is expected an increasing difference between membrane-plate and Williams results closer to the weld seam (i.e. load application area).

<sup>12</sup> The load is represented as a line load applied on a circumference in radial direction. The  $a_2$  radius was considered as the average between the root and weld toe circumference radius.

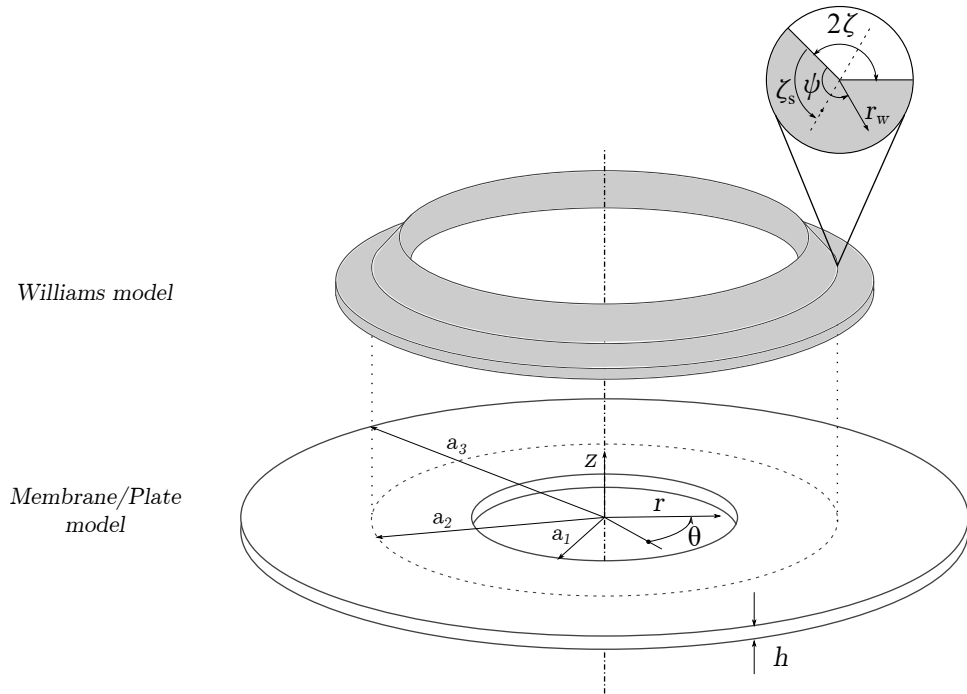
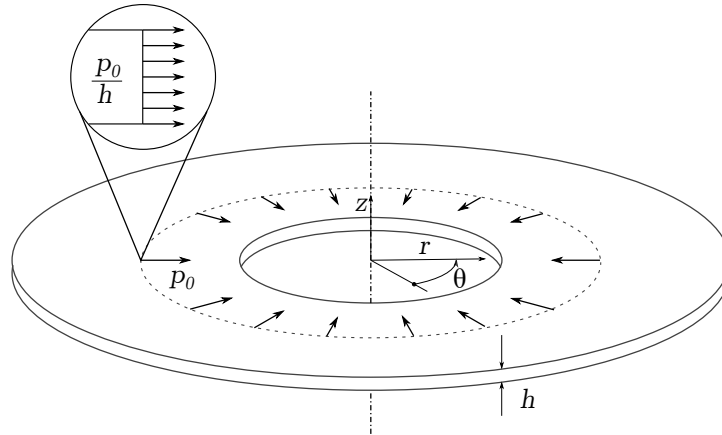


Figure 67: Axisymmetric membrane-plate model and Williams' notch theory

### B.1.1 Membrane model

Figure 68: Membrane model with a constant radial load  $p_0$  over the plate thickness  $h$ 

The general Lamé equation, behind the membrane theory, can be written as follows

$$\frac{E}{1-\nu^2} \frac{d}{dr} \left[ \frac{1}{r} \frac{d}{dr} (ru) \right] + f = 0 \quad (30)$$

where  $r$  is the radial coordinate,  $u$  is the radial displacement and  $f$  are the volumetric forces acting on the membrane. Assuming for our problem negligible volumetric forces (i.e.  $f = 0$ ), Lamé equation becomes homogeneous and unrelated to the elastic properties of the material

$$\frac{d^2u}{dr^2} - \frac{1}{r} \frac{du}{dr} - \frac{u}{r^2} = 0 \quad (31)$$

Radial displacement can be derived by integrating Lamé's equation and introducing integration constants  $c_1$  and  $c_2$

$$u(r) = c_1 r + \frac{c_2}{r} \quad (32)$$

the displacement can be restated considering the two-parts domain of Figure 68:  $I = \{(r, \theta, z) \in \mathbb{R}^3 | r < a_2\}$  and  $II = \{(r, \theta, z) \in \mathbb{R}^3 | r \geq a_2\}$

$$u^{(i)} = c_1^{(i)} r + \frac{c_2^{(i)}}{r} \quad (i = I, II) \quad (33)$$

starting from the displacement, radial and hoop membranal stresses solutions can be easily calculated

$$\sigma_{\theta\theta,M}^{(i)} = \frac{E}{1-\nu^2} \left[ c_1^{(i)}(1+\nu) + \frac{c_2^{(i)}}{r^2}(1-\nu) \right] \quad (i = I, II) \quad (34)$$

$$\sigma_{rr,M}^{(i)} = \frac{E}{1-\nu^2} \left[ c_1^{(i)}(1+\nu) - \frac{c_2^{(i)}}{r^2}(1-\nu) \right] \quad (i = I, II) \quad (35)$$

To obtain the four integration constants  $c_j^{(i)}$  ( $i = I, II; j = 1, 2$ ), it is necessary to set boundary conditions as follows

$$\begin{cases} \sigma_{rr,M}^{(I)}(a_1) = 0 \\ \sigma_{rr,M}^{(II)}(a_3) = 0 \\ u^{(I)}(a_2) = u^{(II)}(a_2) \\ \sigma_{rr,M}^{(II)}(a_2) - \sigma_{rr,M}^{(I)}(a_2) = \frac{p_o}{h} \end{cases} \quad (36)$$

It is worth noting that, the boundary conditions defined above are specific to the problem addressed here; however, they leave the analytical solution quite generalizable with respect to other axisymmetric problems of this kind.

### B.1.2 Plate model

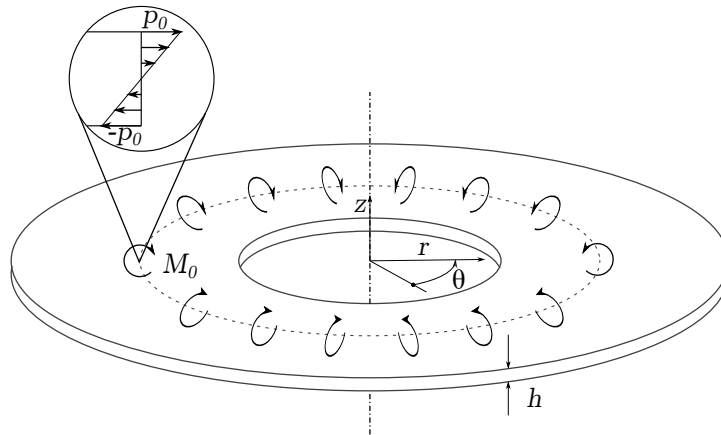


Figure 69: Plate model with a constant momentum load  $M_0 = \frac{p_0 h}{2}$  over the thickness

The general plate theory is based on equation 37, which can be considered the plate's equivalent of the deflection theory for beams

$$\frac{d}{dr} \left[ r \frac{d}{dr} \left( \frac{1}{r} \frac{d}{dr} \left( r \frac{dw}{dr} \right) \right) \right] = \frac{qr}{D} \quad (37)$$

where  $q$  represents the distributed loads and  $D = \frac{Eh^3}{12(1-\nu^2)}$  is the flexural rigidity of the plate. Similarly to section B.1.1, no distributed loads were assumed; the equation underlying the axisymmetric plate theory can now be written as follows

$$\frac{d}{dr} \left[ r \frac{d}{dr} \left( \frac{1}{r} \frac{d}{dr} \left( r \frac{dw}{dr} \right) \right) \right] = 0 \quad (38)$$

The integration of the homogeneous differential equation thus obtained provides the displacement  $w$  in  $z$  direction and its derivatives. To perform the integration, the constants  $d_1$ ,  $d_2$ ,  $d_3$  and  $d_4$  were introduced

$$w^{(i)} = \frac{r^2}{4} \left[ d_1^{(i)} \left( \ln \left( \frac{r}{a_3} \right) - 1 \right) + d_2^{(i)} \right] + d_3^{(i)} \ln \left( \frac{r}{a_3} \right) + d_4^{(i)} \quad (i = I, II) \quad (39)$$

$$\frac{dw^{(i)}}{dr} = \frac{r}{4} \left[ 2d_2^{(i)} + d_1^{(i)} \left( 2 \ln \left( \frac{r}{a_3} \right) - 1 \right) \right] + \frac{d_3^{(i)}}{r} \quad (i = I, II) \quad (40)$$

$$\frac{d^2 w^{(i)}}{dr^2} = \frac{d_1^{(i)}}{4} \left( 2 \ln \left( \frac{r}{a_3} \right) + 1 \right) + \frac{d_2^{(i)}}{2} - \frac{d_3^{(i)}}{r^2} \quad (i = I, II) \quad (41)$$

where  $a_3$  is a normalizing denominator for the variable  $r$ . An equally appropriate normalizing denominator could be the thickness of the plate  $h$ , its choice is arbitrary in this case, because together with the normalizing denominator, an integration constant  $d_2$  has been introduced.

The flexural components can be written as follows

$$M_{rr}^{(i)} = -D \left( \frac{d^2 w^{(i)}}{dr^2} + \nu \frac{1}{r} \frac{dw^{(i)}}{dr} \right) \quad (i = I, II) \quad (42)$$

$$M_{\theta\theta}^{(i)} = -D \left( \frac{1}{r} \frac{dw^{(i)}}{dr} + \nu \frac{d^2 w^{(i)}}{dr^2} \right) \quad (i = I, II) \quad (43)$$

To obtain the eight integration constants  $d_j^{(i)}$  ( $i = I, II; j = 1, 2, 3, 4$ ) it is necessary to set boundary conditions

$$\begin{cases} M_{rr}^{(I)}(a_1) = 0 \\ M_{rr}^{(II)}(a_3) = 0 \\ w^{(II)}(a_3) = 0 \\ d_1^{(I)} = 0 \\ d_1^{(II)} = 0 \\ w^{(I)}(a_2) = w^{(II)}(a_2) \\ \frac{dw^{(I)}}{dr}(a_2) = \frac{dw^{(II)}}{dr}(a_2) \\ M_{rr}^{(I)}(a_2) + \frac{\rho_o h}{2} = M_{rr}^{(II)}(a_2) \end{cases} \quad (44)$$

Starting from the flexural components radial and hoop stresses can be express as a function of  $z$

$$\sigma_{rr,P}^{(i)} = \frac{12}{h^3} M_{rr}^{(i)} z \quad (i = I, II) \quad (45)$$

$$\sigma_{\theta\theta,P}^{(i)} = \frac{12}{h^3} M_{\theta\theta}^{(i)} z \quad (i = I, II) \quad (46)$$

**SUPERPOSITION** Because of the linearity of the problem the superposition principle can be used on the analytical solutions previously found (i.e. membrane theory and plate theory). Since the two models share the reference system, it is possible to directly sum stress results without any coordinate transformation

$$\sigma_{rr}^{(i)} = \sigma_{rr,M}^{(i)} + \sigma_{rr,P}^{(i)} \quad (i = I, II) \quad (47)$$

$$\sigma_{\theta\theta}^{(i)} = \sigma_{\theta\theta,M}^{(i)} + \sigma_{\theta\theta,P}^{(i)} \quad (i = I, II) \quad (48)$$

As the domain  $II$  solution is more relevant for our purposes, only this solution will be discussed below. The stresses belonging to the domain  $II$  will no longer have a superscript in the following, thus to ease the reading process.

### B.1.3 Williams model

The membrane-plate solution is not suitable to describe the stress concentration resulting from the weld notch, because of the very nature of the theory itself. One way to better describe the stress behaviour in this area consists in applying a theory designed for sharp notches. In the following, Williams' theory [84] is adopted to represent the stress behaviour caused by the weld toe notch, combining it with the previously developed theory of membrane-plate.

Williams hypothesis for the Airy stress function<sup>13</sup>  $\Phi$  can be stated as

$$\Phi = r_w^{\lambda+1} F(\psi) \quad (49)$$

$$F(\psi) = e_1 \sin(\lambda + 1)\psi + e_2 \cos(\lambda + 1)\psi + e_3 \sin(\lambda - 1)\psi + e_4 \cos(\lambda - 1)\psi \quad (50)$$

where  $\Phi$  depends from the polar coordinates  $(r_w, \psi)$ , the general parameters  $e_1, e_2, e_3, e_4$  and the exponent  $\lambda$ . Williams corresponding stress field in polar coordinates is defined by the general relationships (i.e. relation between stresses and Airy stress function in polar coordinates)

$$\sigma_{rr} = \frac{1}{r^2} \frac{\partial^2 \Phi}{\partial \psi^2} + \frac{1}{r} \frac{\partial \Phi}{\partial r} \quad (51)$$

$$\sigma_{\psi\psi} = \frac{\partial^2 \Phi}{\partial r^2} \quad (52)$$

$$\sigma_{r\psi} = \frac{1}{r} \frac{\partial^2 \Phi}{\partial r \partial \psi} + \frac{1}{r^2} \frac{\partial \Phi}{\partial \psi} \quad (53)$$

that solved for the Airy stress function  $\Phi$  of Equation 49 leads to

$$\sigma_{rr} = r_w^{\lambda-1} [F''(\psi) + (\lambda + 1)F(\psi)] \quad (54)$$

---

<sup>13</sup> The scalar potential function  $\Phi$  is used to calculate stresses for 2D problems by applying equilibrium equations to stress components defined in Cartesian coordinates as  $\sigma_{xx} = \frac{\partial^2 \Phi}{\partial y^2}$ ,  $\sigma_{yy} = \frac{\partial^2 \Phi}{\partial x^2}$  and  $\tau_{xy} = \frac{\partial^2 \Phi}{\partial x \partial y}$

$$\sigma_{\psi\psi} = r_w^{\lambda-1} [\lambda(\lambda+1)F(\psi)] \quad (55)$$

$$\sigma_{r\psi} = r_w^{\lambda-1} [-\lambda F'(\psi)] \quad (56)$$

Under Williams' hypothesis of a free-free edges, the displacement  $u_i \propto r_w^\lambda$  can be kept bounded by considering  $\lambda > 1$ . The local boundary conditions that are required to calculate  $\lambda$  are

$$\begin{cases} \sigma_{\psi\psi}(0) = \sigma_{\psi\psi}(2\zeta_s) = 0 \\ \sigma_{r\psi}(0) = \sigma_{r\psi}(2\zeta_s) = 0 \end{cases} \quad (57)$$

which can be reformulated as follows

$$\begin{cases} F(0) = F(2\zeta_s) = 0 \\ F'(0) = F'(2\zeta_s) = 0 \end{cases} \quad (58)$$

Equations 58 can be restated in explicit form

$$\begin{cases} e_2 + e_4 = 0 \\ e_1(\lambda+1) + e_3(\lambda-1) = 0 \\ e_1 \sin(2\zeta_s(\lambda+1)) + e_2 \cos(2\zeta_s(\lambda+1)) + e_3 \sin(2\zeta_s(\lambda-1)) + e_4 \cos(2\zeta_s(\lambda-1)) = 0 \\ e_1(\lambda+1)\cos(2\zeta_s(\lambda+1)) - e_2(\lambda+1)\sin(2\zeta_s(\lambda+1)) + e_3(\lambda-1)\cos(2\zeta_s(\lambda-1)) - e_4(\lambda-1)\sin(2\zeta_s(\lambda-1)) = 0 \end{cases} \quad (59)$$

Being interested in the non trivial solution, it is desired to find the minimum value of  $\lambda$  that nullifies the determinant of the system 59. It is worth noting that, the values of the constants  $e_i (i = 1, 2, 3, 4)$  cannot be determined uniquely from the boundary conditions 59, because the equations are homogeneous.

At this point the solution obtained previously from the membrane-plate theory can be used to define the boundary conditions to uniquely determine the parameters  $e_i (i = 1, 2, 3, 4)$ . However, the first term of the Williams expansion, as shown in Equation 54, does not allowed the simultaneous definition of zero-order and first-order continuity between Williams and membrane-plate theory.

The solution proposed here involves the redefinition of the Equation 54 as follows

$$\sigma_{rr}^w = Ar^{\lambda-1} + B \quad (60)$$

and assuming the same behaviour for the hoop stress

$$\sigma_{\theta\theta}^w = Cr^{\lambda-1} + D \quad (61)$$

The constants  $A, B, C, D$  can be obtained defining boundary conditions starting from Equations 47, 48, 60, 61

$$\begin{cases} \sigma_{rr}^w(r_r) - \sigma_{rr}^{II}(r_r) = 0 \\ \frac{d\sigma_{rr}^w}{dr}|_{r=r_r} - \frac{d\sigma_{rr}^{II}}{dr}|_{r=r_r} = 0 \\ \sigma_{\theta\theta}^w(r_\theta) - \sigma_{\theta\theta}^{II}(r_\theta) = 0 \\ \frac{d\sigma_{\theta\theta}^w}{dr}|_{r=r_\theta} - \frac{d\sigma_{\theta\theta}^{II}}{dr}|_{r=r_\theta} = 0 \end{cases} \quad (62)$$

where the parameters  $r_r$  and  $r_\theta$  represents the radial coordinate of the chosen continuity point for the radial and hoop stress respectively.

## B.2 RESULTS AND DISCUSSION

In the following section, analytical results will be presented and discussed, especially regarding the difference between the original membrane-plate model or the one combined with Williams' solution. To obtain stresses results a numerical definition of the parameters is required. For this reason, parameters consistent with the case study presented in [chapter 3](#), [chapter 4](#) and [chapter 6](#) (i.e. pipe-to-plate welded joint) have been chosen. The results shown in Figures [70-71](#), employ the following numerical values

$$\left\{ \begin{array}{l} p_0 = 5000 \text{ N mm}^{-1} \\ h = 25 \text{ mm} \\ a_1 = 10 \text{ mm} \\ a_2 = 42 \text{ mm} \\ a_3 = 90 \text{ mm} \\ E = 206 \text{ GPa} \\ \nu = 0.3 \\ r_r = r_\theta = 70 \text{ mm} \\ 2\zeta = 135^\circ \Rightarrow \lambda = 0.6787 \end{array} \right. \quad (63)$$

Specifically, employing  $2\zeta = 135^\circ$  results in a minimum value of  $\lambda = 0.6787$  that nullifies the determinant of the system [59](#).

Regarding the membrane-plate theory, Figure [70](#) shows results of radial and hoop stresses on the plate surface for  $r > a_2$ . Since this model ignores stress concentration, radial and hoop stresses have finite maximum values of  $225 \text{ MPa}$  and  $-344 \text{ MPa}$  respectively, both in the weld toe location (i.e.  $r = a_2$ ).

After combining Williams' solution with the membrane-plate theory, an important divergence in stress results can be noticed nearby the weld toe position, as shown in Figure [71](#). Above all, Williams' theory introduces a singularity in the notch origin leading to infinite values of stress for  $r_w = 0$ . It should be noticed that, for  $r > 55 \text{ mm}$  no considerable difference exist between the two solutions, even if the continuity points were set at  $r_r = r_\theta = 70 \text{ mm}$ .

In addition, Figures [70-71](#) present stress results obtained from the finite element model described earlier in [chapter 4](#). Both radial and hoop stresses are provided as a convex hull of the stress results along the angular coordinate. First of all, it can be noted that since the finite element model is three-dimensional, a large variation in stress values can be found, mainly due to the presence of the run in-run out point. For a better understanding of results a three-dimensional comparison between numerical results and the analytical model considering Williams' theory is reported in Figures [72-73](#). Generally speaking, both the analytical models presented correctly match the stress gradient away from the weld bead; while only the implementation of Williams' theory manages to introduce the right gradient in the vicinity of the weld toe. However, if the radial stress is described quite faithfully, the hoop stress exhibits a significant discrepancy between analytical theory and numerical results. This difference is mainly due to the fact that the weld bead was not modelled with null thickness (i.e. as instead assumed by the analytical model). Since both radial and hoop stresses present positive values inside the weld bead (see Figure [48](#)), the outer stress results must increase for continuity of the solution. So although negative hoop stress values would be expected analytically near the weld toe, the contraction of the weld seam cause a change of stress solution, creating positive residual stresses values both in radial and hoop direction.

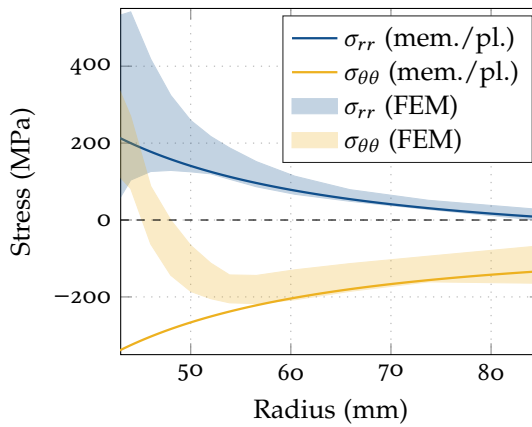


Figure 70: Solution deriving from superposition of membrane and plate theory for  $p_0 = 5000 \text{ N mm}^{-1}$

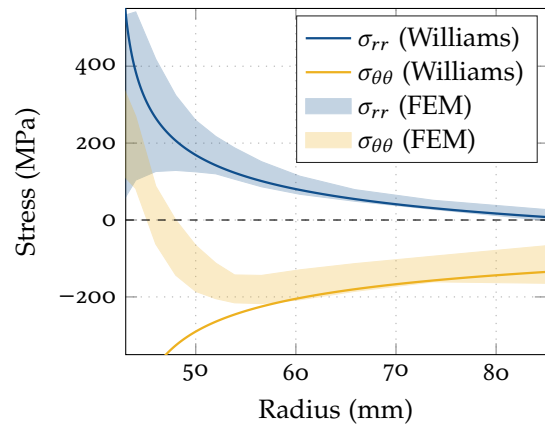


Figure 71: Solution deriving from Co and C1 continuity between Williams' theory and the membrane-plate theory for  $p_0 = 5000 \text{ N mm}^{-1}$

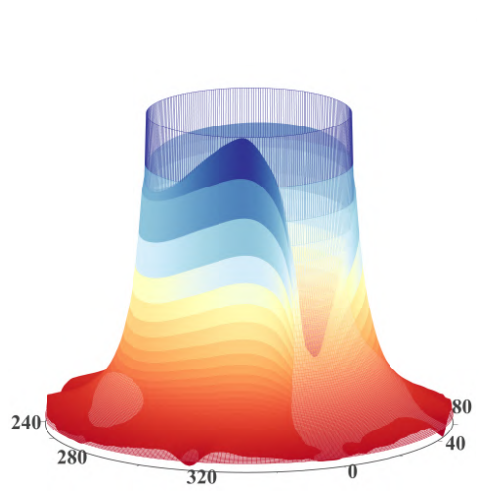


Figure 72: Qualitative comparison between analytical and numerical residual radial stress fields on the plate surface resulting after the implementation of Williams' solution; the solution of the analytical model is represented by means of the grid-like surface

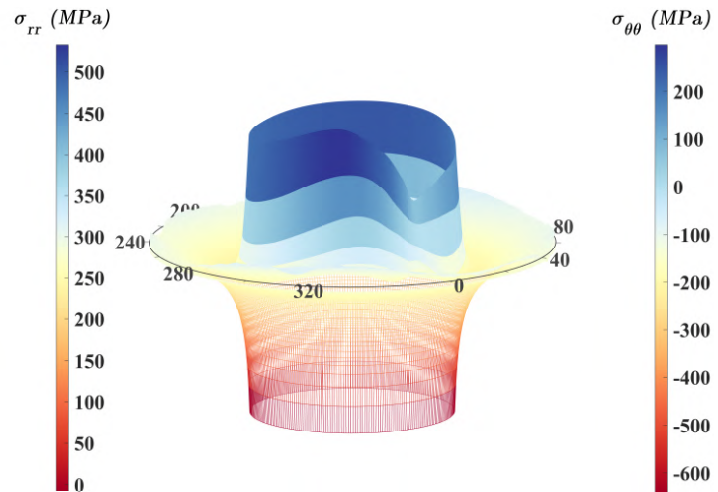


Figure 73: Qualitative comparison between analytical and numerical residual hoop stress fields on the plate surface resulting after the implementation of Williams' solution; the solution of the analytical model is represented by means of the grid-like surface

## BIBLIOGRAPHY

---

- [1] M. Clarin, *High strength steel : Local buckling and residual stresses*, Licentiate thesis, Luleå University of Technology, 2004.
- [2] Z. Barsoum and I. Barsoum, 'Residual stress effects on fatigue life of welded structures using LEFM,' *Engineering Failure Analysis*, vol. 16, no. 1, pp. 449–467, 2009, ISSN: 13506307. DOI: [10.1016/j.engfailanal.2008.06.017](https://doi.org/10.1016/j.engfailanal.2008.06.017).
- [3] G Vanboven, W Chen and R Rogge, 'The role of residual stress in neutral pH stress corrosion cracking of pipeline steels. part i: Pitting and cracking occurrence,' *Acta Materialia*, vol. 55, no. 1, pp. 29–42, 2007. DOI: [10.1016/j.actamat.2006.08.037](https://doi.org/10.1016/j.actamat.2006.08.037).
- [4] R Bartolozzi and F Frendo, 'Stiffness and strength aspects in the design of automotive coil springs for McPherson front suspensions: A case study,' *Proceedings of the Institution of Mechanical Engineers, Part D: Journal of Automobile Engineering*, vol. 225, no. 10, pp. 1377–1391, 2011, ISSN: 09544070. DOI: [10.1177/0954407011403853](https://doi.org/10.1177/0954407011403853).
- [5] R. Montanari, A. Fava and G. Barbieri, 'Experimental Techniques to Investigate Residual Stress in Joints,' in *Residual Stress Analysis on Welded Joints by Means of Numerical Simulation and Experiments*, InTech, 2018. DOI: [10.5772/intechopen.71564](https://doi.org/10.5772/intechopen.71564).
- [6] B. Zheng, S. Yang, X. Jin, G. Shu, S. Dong and Q. Jiang, 'Test on residual stress distribution of welded s600e high-strength stainless steel sections,' *Journal of Constructional Steel Research*, vol. 168, p. 105 994, 2020. DOI: [10.1016/j.jcsr.2020.105994](https://doi.org/10.1016/j.jcsr.2020.105994).
- [7] E. P. Zarandi and B. H. Skallerud, 'Experimental and numerical study of mooring chain residual stresses and implications for fatigue life,' *International Journal of Fatigue*, vol. 135, p. 105 530, 2020. DOI: [10.1016/j.ijfatigue.2020.105530](https://doi.org/10.1016/j.ijfatigue.2020.105530).
- [8] S. Goel, M. Neikter, J. Capek, E. Polatidis, M. Colliander, S. Joshi and R. Pederson, 'Residual stress determination by neutron diffraction in powder bed fusion-built alloy 718: Influence of process parameters and post-treatment,' *Materials & Design*, vol. 195, p. 109 045, 2020. DOI: [10.1016/j.matdes.2020.109045](https://doi.org/10.1016/j.matdes.2020.109045).
- [9] S. Joshi and J. R. Walton, 'Reconstruction of the residual stresses in a hyperelastic body using ultrasound techniques,' *International Journal of Engineering Science*, vol. 70, pp. 46–72, 2013. DOI: [10.1016/j.ijengsci.2013.05.001](https://doi.org/10.1016/j.ijengsci.2013.05.001).
- [10] C. Xu, W. Song, Q. Pan, H. Li and S. Liu, 'Nondestructive testing residual stress using ultrasonic critical refracted longitudinal wave,' *Physics Procedia*, vol. 70, pp. 594–598, 2015. DOI: [10.1016/j.phpro.2015.08.030](https://doi.org/10.1016/j.phpro.2015.08.030).
- [11] G. A Alpsten, 'Thermal residual stresses in hot-rolled steel members, december 1968,' Fritz Laboratory Reports, Tech. Rep., 1968.
- [12] T. Nitschke-Pagel, 'Limitations and recommendations for the measurement of residual stresses in welded joints,' in *Residual Stresses 2018*, vol. 6, Materials Research Proceedings, 2018, pp. 221 –226. DOI: [10.21741/9781945291890-35](https://doi.org/10.21741/9781945291890-35).
- [13] M. C. Smith and A. C. Smith, 'NeT bead-on-plate round robin: Comparison of residual stress predictions and measurements,' *International Journal of Pressure Vessels and Piping*, vol. 86, no. 1, pp. 79–95, 2009, ISSN: 03080161. DOI: [10.1016/j.ijpvp.2008.11.017](https://doi.org/10.1016/j.ijpvp.2008.11.017).
- [14] C. D. Ridgeway, C. Gu, K. Ripplinger, D. Detwiler, M. Ji, S. Soghrati and A. A. Luo, 'Prediction of location specific mechanical properties of aluminum casting using a new CA-FEA (cellular automaton-finite element analysis) approach,' *Materials & Design*, vol. 194, p. 108 929, 2020, ISSN: 18734197. DOI: [10.1016/j.matdes.2020.108929](https://doi.org/10.1016/j.matdes.2020.108929).
- [15] T. Greß, V. G. Nardi, S. Schmid, J. Hoyer, Y. Rizaiev, T. Boll, S. Seils, B. Tonn and W. Volk, 'Vertical continuous compound casting of copper aluminum bilayer rods,' *Journal of Materials Processing Technology*, vol. 288, p. 116 854, 2021, ISSN: 09240136. DOI: [10.1016/j.jmatprotec.2020.116854](https://doi.org/10.1016/j.jmatprotec.2020.116854).

- [16] E. Anglada, A. Meléndez, A. Obregón, E. Villanueva and I. Garmendia, 'Performance of optimization algorithms in the model fitting of the multi-scale numerical simulation of ductile iron solidification,' *Metals*, vol. 10, no. 8, p. 1071, 2020, ISSN: 20754701. DOI: [10.3390/met10081071](https://doi.org/10.3390/met10081071).
- [17] P. Jayakrishna, S. Chakraborty, S. Ganguly and P. Talukdar, 'A novel method for determining the three dimensional variation of non-linear thermal resistance at the mold-strand interface in billet continuous casting process,' *International Communications in Heat and Mass Transfer*, vol. 119, p. 104984, 2020, ISSN: 07351933. DOI: [10.1016/j.icheatmasstransfer.2020.104984](https://doi.org/10.1016/j.icheatmasstransfer.2020.104984).
- [18] M. Sandeep and M. Sandeep, 'Modeling and analysis of residual stresses in castings using AlSi12(fe) and NiCu30(fe) materials,' *IOP Conference Series: Materials Science and Engineering*, vol. 912, no. 3, p. 032047, 2020, ISSN: 1757899X. DOI: [10.1088/1757-899x/912/3/032047](https://doi.org/10.1088/1757-899x/912/3/032047).
- [19] A. A. Bhatti, Z. Barsoum, H. Murakawa and I. Barsoum, 'Influence of thermo-mechanical material properties of different steel grades on welding residual stresses and angular distortion,' *Materials & Design (1980-2015)*, vol. 65, pp. 878–889, 2015, ISSN: 18734197. DOI: [10.1016/j.matdes.2014.10.019](https://doi.org/10.1016/j.matdes.2014.10.019).
- [20] A. Capriccioli and P. Frosi, 'Multipurpose ANSYS FE procedure for welding processes simulation,' *Fusion Engineering and Design*, vol. 84, no. 2-6, pp. 546–553, 2009, ISSN: 09203796. DOI: [10.1016/j.fusengdes.2009.01.039](https://doi.org/10.1016/j.fusengdes.2009.01.039).
- [21] H. Xin and M. Veljkovic, 'Residual stress effects on fatigue crack growth rate of mild steel s355 exposed to air and seawater environments,' *Materials & Design*, vol. 193, p. 108732, 2020, ISSN: 18734197. DOI: [10.1016/j.matdes.2020.108732](https://doi.org/10.1016/j.matdes.2020.108732).
- [22] J. Chen, E. Salvati, F. Uzun, C. Papadaki, Z. Wang, J. Everaerts and A. M. Korsunsky, 'An experimental and numerical analysis of residual stresses in a TIG weldment of a single crystal nickel-base superalloy,' *Journal of Manufacturing Processes*, vol. 53, pp. 190–200, 2020, ISSN: 15266125. DOI: [10.1016/j.jmapro.2020.02.007](https://doi.org/10.1016/j.jmapro.2020.02.007).
- [23] K. Hemmesi, M. Farajian and M. Boin, 'Numerical studies of welding residual stresses in tubular joints and experimental validations by means of x-ray and neutron diffraction analysis,' *Materials & Design*, vol. 126, pp. 339–350, 2017, ISSN: 18734197. DOI: [10.1016/j.matdes.2017.03.088](https://doi.org/10.1016/j.matdes.2017.03.088).
- [24] K. Hemmesi, P. Mallet and M. Farajian, 'Numerical evaluation of surface welding residual stress behavior under multiaxial mechanical loading and experimental validations,' *International Journal of Mechanical Sciences*, vol. 168, p. 105127, 2020, ISSN: 00207403. DOI: [10.1016/j.ijmecsci.2019.105127](https://doi.org/10.1016/j.ijmecsci.2019.105127).
- [25] J.-H. Lee, B.-S. Jang, H.-J. Kim, S. H. Shim and S. W. Im, 'The effect of weld residual stress on fracture toughness at the intersection of two welding lines of offshore tubular structure,' *Marine Structures*, vol. 71, p. 102708, 2020, ISSN: 09518339. DOI: [10.1016/j.marstruc.2020.102708](https://doi.org/10.1016/j.marstruc.2020.102708).
- [26] P. Asadi, S. Alimohammadi, O. Kohantorabi, A. Fazli and M. Akbari, 'Effects of material type, preheating and weld pass number on residual stress of welded steel pipes by multi-pass TIG welding (c-mn, SUS304, SUS316),' *Thermal Science and Engineering Progress*, vol. 16, p. 100462, 2020, ISSN: 24519049. DOI: [10.1016/j.tsep.2019.100462](https://doi.org/10.1016/j.tsep.2019.100462).
- [27] J. Lin, N. Ma, X. Liu and Y. Lei, 'Modification of residual stress distribution in welded joint of titanium alloy with multi electron beam heating,' *Journal of Materials Processing Technology*, vol. 278, p. 116504, 2020, ISSN: 09240136. DOI: [10.1016/j.jmatprotec.2019.116504](https://doi.org/10.1016/j.jmatprotec.2019.116504).
- [28] N. Ansaripour, A. Heidari and S. A. Eftekhari, 'Multi-objective optimization of residual stresses and distortion in submerged arc welding process using genetic algorithm and harmony search,' *Proceedings of the Institution of Mechanical Engineers, Part C: Journal of Mechanical Engineering Science*, vol. 234, no. 4, pp. 862–871, 2019, ISSN: 20412983. DOI: [10.1177/0954406219885977](https://doi.org/10.1177/0954406219885977).
- [29] H. Majidi, A. Torabi, M. Zabihi, S. Razavi and F. Berto, 'Energy-based ductile failure predictions in cracked friction-stir welded joints,' *Engineering Failure Analysis*, vol. 102, pp. 327–337, 2019, ISSN: 13506307. DOI: [10.1016/j.engfailanal.2019.04.066](https://doi.org/10.1016/j.engfailanal.2019.04.066).
- [30] Y. Lu, S. Zhu, Z. Zhao, T. Chen and J. Zeng, 'Numerical simulation of residual stresses in aluminum alloy welded joints,' *Journal of Manufacturing Processes*, vol. 50, pp. 380–393, 2020, ISSN: 15266125. DOI: [10.1016/j.jmapro.2019.12.056](https://doi.org/10.1016/j.jmapro.2019.12.056).

- [31] Z. Xiao, C. Chen, H. Zhu, Z. Hu, B. Nagarajan, L. Guo and X. Zeng, 'Study of residual stress in selective laser melting of ti6al4v,' *Materials & Design*, vol. 193, p. 108846, 2020, ISSN: 18734197. DOI: [10.1016/j.matdes.2020.108846](https://doi.org/10.1016/j.matdes.2020.108846).
- [32] X. Song, S. Feih, W. Zhai *et al.*, 'Advances in additive manufacturing process simulation: Residual stresses and distortion predictions in complex metallic components,' *Materials & Design*, vol. 193, p. 108779, 2020, ISSN: 18734197. DOI: [10.1016/j.matdes.2020.108779](https://doi.org/10.1016/j.matdes.2020.108779).
- [33] R. Wagener, M. Hell, M. Scurria and T. Bein, 'Deriving the structural fatigue behavior of additively manufactured components,' in *TMS 2020 149th Annual Meeting & Exhibition Supplemental Proceedings*, Springer International Publishing, 2020, pp. 139–149, ISBN: 9783030362959. DOI: [10.1007/978-3-030-36296-6\\_13](https://doi.org/10.1007/978-3-030-36296-6_13).
- [34] S. Razavi, B. V. Hooreweder and F. Berto, 'Effect of build thickness and geometry on quasi-static and fatigue behavior of ti-6al-4v produced by electron beam melting,' *Additive Manufacturing*, vol. 36, p. 101426, 2020, ISSN: 22148604. DOI: [10.1016/j.addma.2020.101426](https://doi.org/10.1016/j.addma.2020.101426).
- [35] K. Schnabel, J. Baumgartner and B. Möller, 'Fatigue assessment of additively manufactured metallic structures using local approaches based on finite-element simulations,' *Procedia Structural Integrity*, vol. 19, pp. 442–451, 2019, ISSN: 24523216. DOI: [10.1016/j.prostr.2019.12.048](https://doi.org/10.1016/j.prostr.2019.12.048).
- [36] K. An, L. Yuan, L. Dial, I. Spinelli, A. D. Stoica and Y. Gao, 'Neutron residual stress measurement and numerical modeling in a curved thin-walled structure by laser powder bed fusion additive manufacturing,' *Materials & Design*, vol. 135, pp. 122–132, 2017, ISSN: 18734197. DOI: [10.1016/j.matdes.2017.09.018](https://doi.org/10.1016/j.matdes.2017.09.018).
- [37] Y. Zhou, X. Chen, Z. Fan and S. Rao, 'Finite element modelling of welding residual stress and its influence on creep behavior of a 2.25cr-1mo-0.25v steel cylinder,' *Procedia Engineering*, vol. 130, pp. 552–559, 2015. DOI: [10.1016/j.proeng.2015.12.264](https://doi.org/10.1016/j.proeng.2015.12.264).
- [38] X. Wang, Q. Meng and W. Hu, 'Numerical analysis of low cycle fatigue for welded joints considering welding residual stress and plastic damage under combined bending and local compressive loads,' *Fatigue & Fracture of Engineering Materials & Structures*, 2020. DOI: [10.1111/ffe.13216](https://doi.org/10.1111/ffe.13216).
- [39] L. Bertini, F. Bucchi, F. Frendo, M. Moda and B. D. Monelli, 'Residual stress prediction in selective laser melting,' *The International Journal of Advanced Manufacturing Technology*, vol. 105, no. 1-4, pp. 609–636, 2019. DOI: [10.1007/s00170-019-04091-5](https://doi.org/10.1007/s00170-019-04091-5).
- [40] D. Gery, H. Long and P. Maropoulos, 'Effects of welding speed, energy input and heat source distribution on temperature variations in butt joint welding,' *Journal of Materials Processing Technology*, vol. 167, no. 2-3, pp. 393–401, 2005. DOI: [10.1016/j.jmatprotec.2005.06.018](https://doi.org/10.1016/j.jmatprotec.2005.06.018).
- [41] J. Goldak, A. Chakravarti and M. Bibby, 'A new finite element model for welding heat sources,' *Metallurgical Transactions B*, vol. 15, no. 2, pp. 299–305, 1984. DOI: [10.1007/bf02667333](https://doi.org/10.1007/bf02667333).
- [42] J. Moravec, T. Kik and I. Novakova, 'APPLICATION OF NUMERICAL SIMULATIONS ON x10crwmovnb9-2 STEEL MULTILAYER WELDING,' *MM Science Journal*, vol. 2016, no. 05, pp. 1190–1193, 2016. DOI: [10.17973/mmsj.2016\\_11\\_201628](https://doi.org/10.17973/mmsj.2016_11_201628).
- [43] M. Zubairuddin, S. K. Albert, S. Mahadevan, M. Vasudevan, V. Chaudhari and V. K. Suri, 'Experimental and finite element analysis of residual stress and distortion in GTA welding of modified 9cr-1mo steel,' *Journal of Mechanical Science and Technology*, vol. 28, no. 12, pp. 5095–5105, 2014. DOI: [10.1007/s12206-014-1132-0](https://doi.org/10.1007/s12206-014-1132-0).
- [44] T. Flint, J. Francis, M. Smith and J. Balakrishnan, 'Extension of the double-ellipsoidal heat source model to narrow-groove and keyhole weld configurations,' *Journal of Materials Processing Technology*, vol. 246, pp. 123–135, 2017. DOI: [10.1016/j.jmatprotec.2017.02.002](https://doi.org/10.1016/j.jmatprotec.2017.02.002).
- [45] J. Cho, B. Lee, Y. Moon and C. V. Tyne, 'Investigation of residual stress and post weld heat treatment of multi-pass welds by finite element method and experiments,' *Journal of Materials Processing Technology*, vol. 155-156, pp. 1690–1695, 2004. DOI: [10.1016/j.jmatprotec.2004.04.325](https://doi.org/10.1016/j.jmatprotec.2004.04.325).
- [46] D. Deng, 'FEM prediction of welding residual stress and distortion in carbon steel considering phase transformation effects,' *Materials and Design*, vol. 30, no. 2, pp. 359–366, 2009, ISSN: 02641275. DOI: [10.1016/j.matdes.2008.04.052](https://doi.org/10.1016/j.matdes.2008.04.052).

- [47] D. Deng and H. Murakawa, 'Prediction of welding residual stress in multi-pass butt-welded modified 9cr-1mo steel pipe considering phase transformation effects,' *Computational Materials Science*, vol. 37, no. 3, pp. 209–219, 2006. DOI: [10.1016/j.commatsci.2005.06.010](https://doi.org/10.1016/j.commatsci.2005.06.010).
- [48] Y.-F. Hu, K.-F. Chung, H. Ban and D. A. Nethercot, 'Investigations into residual stresses in s690 cold-formed circular hollow sections due to transverse bending and longitudinal welding,' *Engineering Structures*, vol. 219, p. 110911, 2020. DOI: [10.1016/j.engstruct.2020.110911](https://doi.org/10.1016/j.engstruct.2020.110911).
- [49] Z. Lei, J. Zou, D. Wang, Z. Guo, R. Bai, H. Jiang and C. Yan, 'Finite-element inverse analysis of residual stress for laser welding based on a contour method,' *Optics & Laser Technology*, vol. 129, p. 106289, 2020. DOI: [10.1016/j.optlastec.2020.106289](https://doi.org/10.1016/j.optlastec.2020.106289).
- [50] R. Reda, M. Magdy and M. Rady, 'Ti-6al-4v TIG weld analysis using FEM simulation and experimental characterization,' *Iranian Journal of Science and Technology, Transactions of Mechanical Engineering*, vol. 44, no. 3, pp. 765–782, 2019. DOI: [10.1007/s40997-019-00287-y](https://doi.org/10.1007/s40997-019-00287-y).
- [51] A. Chiocca, F. Frendo and L. Bertini, 'Experimental evaluation of relaxed strains in a pipe-to-plate welded joint by means of incremental cutting process,' *Procedia Structural Integrity*, vol. 28, pp. 2157–2167, 2020, ISSN: 24523216. DOI: [10.1016/j.prostr.2020.11.043](https://doi.org/10.1016/j.prostr.2020.11.043).
- [52] D. Radaj, C. M. Sonsino and W. Fricke, *Fatigue Assessment of Welded Joints by Local Approaches: Second Edition*. 2006, pp. 1–639, ISBN: 9781855739482. DOI: [10.1533/9781845691882](https://doi.org/10.1533/9781845691882).
- [53] Ö. Karakaş, F. Berto and L. Susmel, *Special Issue: Fatigue Assessment of Welded Joints by Modern Concepts*, 2017. DOI: [10.1016/j.ijfatigue.2017.05.009](https://doi.org/10.1016/j.ijfatigue.2017.05.009).
- [54] EN 1993-1-1/AC, *Eurocode 3: Design of steel structures - Part 1-1: General rules and rules for buildings*, 2009.
- [55] W. Fricke, *IIW Recommendations for the Fatigue Assessment of Welded Structures By Notch Stress Analysis: IIW-2006-09*. Woodhead Pub, 2012, pp. 1–41, ISBN: 9780857098559. DOI: [10.1533/9780857098566](https://doi.org/10.1533/9780857098566).
- [56] A. F. Hobbacher, 'The new IIW recommendations for fatigue assessment of welded joints and components – a comprehensive code recently updated,' *International Journal of Fatigue*, vol. 31, no. 1, pp. 50–58, 2009. DOI: [10.1016/j.ijfatigue.2008.04.002](https://doi.org/10.1016/j.ijfatigue.2008.04.002).
- [57] D. Taylor, 'The theory of critical distances,' *Engineering Fracture Mechanics*, vol. 75, no. 7, pp. 1696–1705, 2008, ISSN: 00137944. DOI: [10.1016/j.engfracmech.2007.04.007](https://doi.org/10.1016/j.engfracmech.2007.04.007).
- [58] H. Neuber, 'Theory of notch stresses: Principles for exact calculation of strength with reference to structural form and material,' *Springer-Verlag*, p. 292, 1958.
- [59] ——, 'Über die berücksichtigung der spannungskonzentration bei festigkeitsberechnungen,' *Konstruktion*, vol. 20, no. 7, pp. 245–251, 1968.
- [60] M. El May, N. Saintier, T. Palin-Luc and O. Devos, 'Non-local high cycle fatigue strength criterion for metallic materials with corrosion defects,' *Fatigue and Fracture of Engineering Materials and Structures*, vol. 38, no. 9, pp. 1017–1025, 2015, ISSN: 14602695. DOI: [10.1111/ffe.12329](https://doi.org/10.1111/ffe.12329).
- [61] R. Peterson, 'Notch sensitivity, metal fatigue,' *Notch Sensitivity, Metal Fatigue*, pp. 293–306, 1959, cited By 31.
- [62] D. Taylor, 'The theory of critical distances,' in *Fracture of Nano and Engineering Materials and Structures - Proceedings of the 16th European Conference of Fracture*, Kluwer Academic Publishers, 2006, pp. 1095–1096, ISBN: 9781402049712. DOI: [10.1007/1-4020-4972-2\\_543](https://doi.org/10.1007/1-4020-4972-2_543).
- [63] Karakaş, G. Zhang and C. M. Sonsino, 'Critical distance approach for the fatigue strength assessment of magnesium welded joints in contrast to Neuber's effective stress method,' *International Journal of Fatigue*, vol. 112, pp. 21–35, 2018, ISSN: 01421123. DOI: [10.1016/j.ijfatigue.2018.03.004](https://doi.org/10.1016/j.ijfatigue.2018.03.004).
- [64] D. Taylor, 'Geometrical effects in fatigue: a unifying theoretical model,' *International Journal of Fatigue*, vol. 21, no. 5, pp. 413–420, 1999, ISSN: 01421123. DOI: [10.1016/S0142-1123\(99\)00007-9](https://doi.org/10.1016/S0142-1123(99)00007-9).
- [65] D. Taylor, P. Bologna and K. Bel Knani, 'Prediction of fatigue failure location on a component using a critical distance method,' *International Journal of Fatigue*, vol. 22, no. 9, pp. 735–742, 2000, ISSN: 01421123. DOI: [10.1016/S0142-1123\(00\)00062-1](https://doi.org/10.1016/S0142-1123(00)00062-1).

- [66] M. H. El Haddad, K. N. Smith and T. H. Topper, 'Fatigue crack propagation of short cracks,' *Journal of Engineering Materials and Technology, Transactions of the ASME*, vol. 101, no. 1, pp. 42–46, 1979, ISSN: 15288889. DOI: [10.1115/1.3443647](https://doi.org/10.1115/1.3443647).
- [67] L. Susmel, 'The theory of critical distances: a review of its applications in fatigue,' *Engineering Fracture Mechanics*, vol. 75, no. 7, pp. 1706–1724, 2008, ISSN: 00137944. DOI: [10.1016/j.engfracmech.2006.12.004](https://doi.org/10.1016/j.engfracmech.2006.12.004).
- [68] F. Berto, P. Lazzarin and D. Radaj, 'Fictitious notch rounding concept applied to sharp V-notches: Evaluation of the microstructural support factor for different failure hypotheses. Part II: Microstructural support analysis,' *Engineering Fracture Mechanics*, vol. 76, no. 9, pp. 1151–1175, 2009, ISSN: 00137944. DOI: [10.1016/j.engfracmech.2008.01.015](https://doi.org/10.1016/j.engfracmech.2008.01.015).
- [69] D. Radaj, '8 - notch stress approach for assessment of fatigue strength of seam welded joints,' in *Design and Analysis of Fatigue Resistant Welded Structures*, ser. Woodhead Publishing Series in Welding and Other Joining Technologies, D. Radaj, Ed., Woodhead Publishing, 1990, pp. 208–276, ISBN: 978-1-85573-004-5. DOI: [10.1533/9781845698751.208](https://doi.org/10.1533/9781845698751.208).
- [70] D. Radaj, C. Sonsino and W. Fricke, '4 - notch stress approach for seam-welded joints,' in *Fatigue Assessment of Welded Joints by Local Approaches (Second Edition)*, ser. Woodhead Publishing Series in Welding and Other Joining Technologies, D. Radaj, C. Sonsino and W. Fricke, Eds., Second Edition, Woodhead Publishing, 2006, pp. 91–190, ISBN: 978-1-85573-948-2. DOI: [10.1533/9781845691882.91](https://doi.org/10.1533/9781845691882.91).
- [71] A. F. Hobbacher, *Recommendations for Fatigue Design of Welded Joints and Components*. Springer International Publishing, 2016. DOI: [10.1007/978-3-319-23757-2](https://doi.org/10.1007/978-3-319-23757-2).
- [72] W. Fricke, *IIW Recommendations for the Fatigue Assessment of Welded Structures By Notch Stress Analysis: IIW-2006-09*. Elsevier, 2012, pp. 1–41, ISBN: 9780857098559. DOI: [10.1533/9780857098566](https://doi.org/10.1533/9780857098566).
- [73] C. M. Sonsino, 'Course of SN-curves especially in the high-cycle fatigue regime with regard to component design and safety,' *International Journal of Fatigue*, vol. 29, no. 12, pp. 2246–2258, 2007, ISSN: 01421123. DOI: [10.1016/j.ijfatigue.2006.11.015](https://doi.org/10.1016/j.ijfatigue.2006.11.015).
- [74] C. M. Sonsino, 'A consideration of allowable equivalent stresses for fatigue design of welded joints according to the notch stress concept with the reference radii rref = 1.00 and 0.05 mm,' *Welding in the World*, vol. 53, no. 3-4, R64–R75, 2009, ISSN: 00432288. DOI: [10.1007/BF03266705](https://doi.org/10.1007/BF03266705).
- [75] C. M. Sonsino, T. Bruder and J. Baumgartner, *S-N lines for welded thin joints - Suggested slopes and fat values for applying the notch stress concept with various reference RADII*, 2010. DOI: [10.1007/BF03266752](https://doi.org/10.1007/BF03266752).
- [76] 'Method for Prediction of Coffin Manson Parameters from Monotonic Tensile Property for Aluminium 6XXX Series Alloy to Predict Fatigue Life,' in *SAE Technical Papers*, vol. 2019-Janua, SAE International, 2019. DOI: [10.4271/2019-26-0314](https://doi.org/10.4271/2019-26-0314).
- [77] L. F. Coffin Jr, 'A study of the effects of cyclic thermal stress on a ductile metal,' Jun. 1953.
- [78] S. S. Manson, 'Behavior Of Materials Under Conditions Of Thermal Stress,' Tech. Rep., 1953, pp. 317–350.
- [79] W. N. Findley, 'A Theory for the Effect of Mean Stress on Fatigue of Metals Under Combined Torsion and Axial Load or Bending,' *Journal of Engineering for Industry*, vol. 81, no. 4, pp. 301–305, 1959, ISSN: 0022-0817. DOI: [10.1115/1.4008327](https://doi.org/10.1115/1.4008327).
- [80] M. W. Brown and K. J. Miller, 'A Theory for Fatigue Failure under Multiaxial Stress-Strain Conditions,' *Proceedings of the Institution of Mechanical Engineers*, vol. 187, no. 1, pp. 745–755, 1973, ISSN: 0020-3483. DOI: [10.1243/pime\\_proc\\_1973\\_187\\_069\\_02](https://doi.org/10.1243/pime_proc_1973_187_069_02).
- [81] A. Fatemi and D. F. Socie, 'A critical plane approach to multiaxial fatigue damage including out-of-phase loading,' *Fatigue & Fracture of Engineering Materials & Structures*, vol. 11, no. 3, pp. 149–165, 1988, ISSN: 14602695. DOI: [10.1111/j.1460-2695.1988.tb01169.x](https://doi.org/10.1111/j.1460-2695.1988.tb01169.x).
- [82] A. Carpinteri and A. Spagnoli, 'Multiaxial high-cycle fatigue criterion for hard metals,' *International Journal of Fatigue*, vol. 23, no. 2, pp. 135–145, 2001, ISSN: 01421123. DOI: [10.1016/S0142-1123\(00\)00075-X](https://doi.org/10.1016/S0142-1123(00)00075-X).

- [83] P Lazzarin and R Tovo, 'A notch intensity factor approach to the stress analysis of welds,' *Fatigue and Fracture of Engineering Materials and Structures*, vol. 21, no. 9, pp. 1089–1103, 1998, ISSN: 8756758X. doi: [10.1046/j.1460-2695.1998.00097.x](https://doi.org/10.1046/j.1460-2695.1998.00097.x).
- [84] M. L. Williams, 'Stress Singularities Resulting From Various Boundary Conditions in Angular Corners of Plates in Extension,' *Journal of Applied Mechanics*, vol. 19, no. 4, pp. 526–528, 1952, ISSN: 0021-8936. doi: [10.1115/1.4010553](https://doi.org/10.1115/1.4010553).
- [85] G. Meneghetti, 'The use of peak stresses for fatigue strength assessments of welded lap joints and cover plates with toe and root failures,' *Engineering Fracture Mechanics*, vol. 89, pp. 40–51, 2012, ISSN: 00137944. doi: [10.1016/j.engfracmech.2012.04.007](https://doi.org/10.1016/j.engfracmech.2012.04.007).
- [86] P. Lazzarin and R. Zambardi, 'A finite-volume-energy based approach to predict the static and fatigue behavior of components with sharp V-shaped notches,' *International Journal of Fracture*, vol. 112, no. 3, pp. 275–298, 2001, ISSN: 03769429. doi: [10.1023/A:1013595930617](https://doi.org/10.1023/A:1013595930617).
- [87] H. Nisitani and T. Teranishi, 'KI of a circumferential crack emanating from an ellipsoidal cavity obtained by the crack tip stress method in FEM,' *Engineering Fracture Mechanics*, vol. 71, no. 4-6, pp. 579–585, 2004, ISSN: 00137944. doi: [10.1016/S0013-7944\(03\)00035-3](https://doi.org/10.1016/S0013-7944(03)00035-3).
- [88] G. Meneghetti and P. Lazzarin, 'Significance of the elastic peak stress evaluated by FE analyses at the point of singularity of sharp V-notched components,' *Fatigue and Fracture of Engineering Materials and Structures*, vol. 30, no. 2, pp. 95–106, 2007, ISSN: 8756758X. doi: [10.1111/j.1460-2695.2006.01084.x](https://doi.org/10.1111/j.1460-2695.2006.01084.x).
- [89] G. Meneghetti, 'The peak stress method applied to fatigue strength assessments of load carrying transverse fillet welds with toe or root failures,' *SDHM Structural Durability and Health Monitoring*, vol. 8, no. 2, pp. 111–130, 2012, ISSN: 19302983. doi: [10.3970/sdhm.2012.008.111](https://doi.org/10.3970/sdhm.2012.008.111).
- [90] G. Meneghetti, 'The peak stress method for fatigue strength assessment of tube-to-flange welded joints under torsion loading,' *Welding in the World*, vol. 57, no. 2, pp. 265–275, 2013, ISSN: 00432288. doi: [10.1007/s40194-013-0022-x](https://doi.org/10.1007/s40194-013-0022-x).
- [91] G. Meneghetti, C. Guzzella and B. Atzori, 'The peak stress method combined with 3D finite element models for fatigue assessment of toe and root cracking in steel welded joints subjected to axial or bending loading,' in *Fatigue and Fracture of Engineering Materials and Structures*, vol. 37, John Wiley & Sons, Ltd, 2014, pp. 722–739. doi: [10.1111/fme.12171](https://doi.org/10.1111/fme.12171).
- [92] B. Standards, 'BS 7910: Guide to methods for assessing the acceptability of flaws in metallic structures,' *BSI Standards Publication*, vol. 3, no. 1, p. 306, 2013.
- [93] T. L. Anderson and D. A. Osage, 'API 579: A comprehensive fitness-for-service guide,' *International Journal of Pressure Vessels and Piping*, vol. 77, no. 14-15, pp. 953–963, 2000, ISSN: 03080161. doi: [10.1016/S0308-0161\(01\)00018-7](https://doi.org/10.1016/S0308-0161(01)00018-7).
- [94] N. Tebedge, G. Alpsten and L. Tall, 'Residual-stress measurement by the sectioning method - A procedure for residual-stress measurements by the sectioning method is described. Two different hole-drilling methods were performed and the results are compared,' *Experimental Mechanics*, vol. 13, no. 2, pp. 88–96, 1973, ISSN: 00144851. doi: [10.1007/BF02322389](https://doi.org/10.1007/BF02322389).
- [95] M. B. Prime, 'Cross-sectional mapping of residual stresses by measuring the surface contour after a cut,' *Journal of Engineering Materials and Technology, Transactions of the ASME*, vol. 123, no. 2, pp. 162–168, 2001, ISSN: 00944289. doi: [10.1115/1.1345526](https://doi.org/10.1115/1.1345526).
- [96] A. S. f. T. and Materials, 'ASTM E-837 (2008)e1. Standard Test Method for Determining Residual Stresses by the Hole-Drilling Strain-Gage Method.,' Tech. Rep., 1999, pp. 1–17.
- [97] Y. Javadi, M. Akhlaghi and M. A. Najafabadi, 'Using finite element and ultrasonic method to evaluate welding longitudinal residual stress through the thickness in austenitic stainless steel plates,' *Materials and Design*, vol. 45, pp. 628–642, 2013, ISSN: 02641275. doi: [10.1016/j.matdes.2012.09.038](https://doi.org/10.1016/j.matdes.2012.09.038).
- [98] T. Greß, V. Glück Nardi, S. Schmid, J. Hoyer, Y. Rizaiev, T. Boll, S. Seils, B. Tonn and W. Volk, 'Vertical continuous compound casting of copper aluminum bilayer rods,' *Journal of Materials Processing Technology*, vol. 288, p. 116854, 2021, ISSN: 09240136. doi: [10.1016/j.jmatprotec.2020.116854](https://doi.org/10.1016/j.jmatprotec.2020.116854).

- [99] J. Choi and J. Mazumder, 'Numerical and experimental analysis for solidification and residual stress in the GMAW process for AISI 304 stainless steel,' *Journal of Materials Science*, vol. 37, pp. 2143–2158, 2002, ISSN: 00222461. DOI: [10.1023/A:1015258322780](https://doi.org/10.1023/A:1015258322780).
- [100] N. Ansaripour, A. Heidari and S. A. Eftekhari, 'Multi-objective optimization of residual stresses and distortion in submerged arc welding process using Genetic Algorithm and Harmony Search,' *Proceedings of the Institution of Mechanical Engineers, Part C: Journal of Mechanical Engineering Science*, vol. 234, no. 4, pp. 862–871, 2020, ISSN: 20412983. DOI: [10.1177/0954406219885977](https://doi.org/10.1177/0954406219885977).
- [101] N. Ben Moussa, H Sidhom and C Braham, 'Numerical and experimental analysis of residual stress and plastic strain distributions in machined stainless steel,' *International Journal of Mechanical Sciences*, vol. 64, no. 1, pp. 82–93, 2012, ISSN: 00207403. DOI: [10.1016/j.ijmecsci.2012.07.011](https://doi.org/10.1016/j.ijmecsci.2012.07.011).
- [102] N. Stenberg and J. Proudian, 'Numerical modelling of turning to find residual stresses,' in *Procedia CIRP*, vol. 8, 2013, pp. 258–264. DOI: [10.1016/j.procir.2013.06.099](https://doi.org/10.1016/j.procir.2013.06.099).
- [103] Z. Pan, S. Y. Liang and H. Garmestani, 'Finite element simulation of residual stress in machining of Ti-6Al-4V with a microstructural consideration,' *Proceedings of the Institution of Mechanical Engineers, Part B: Journal of Engineering Manufacture*, vol. 233, no. 4, pp. 1103–1111, 2019, ISSN: 20412975. DOI: [10.1177/0954405418769927](https://doi.org/10.1177/0954405418769927).
- [104] E. Abboud, B. Shi, H. Attia, V. Thomson and Y. Mebrahtu, 'Finite element-based modeling of machining-induced residual stresses in Ti-6Al-4V under finish turning conditions,' in *Procedia CIRP*, vol. 8, Elsevier B.V., 2013, pp. 63–68. DOI: [10.1016/j.procir.2013.06.066](https://doi.org/10.1016/j.procir.2013.06.066).
- [105] P. Łuczyński, M. Giesen, T. S. Gier and M. Wirsum, 'Uncoupled CFD-FEA methods for the thermo-structural analysis of turbochargers,' *International Journal of Turbomachinery, Propulsion and Power*, vol. 4, no. 4, p. 39, 2019, ISSN: 2504186X. DOI: [10.3390/ijtpp4040039](https://doi.org/10.3390/ijtpp4040039).
- [106] S. Jain and A. Agrawal, 'Coupled Thermal – Structural Finite Element Analysis for Exhaust Manifold of an Off-road Vehicle Diesel Engine,' *International Journal of Soft Computing and Engineering*, vol. 3, no. 4, pp. 226–230, 2013.
- [107] P. R. De Freitas Teixeira, D. B. De Araújo and L. A. B. Da Cunha, 'Study of the Gaussian distribution heat source model applied to numerical thermal simulations of tig welding processes,' *Ciencia y Engenharia/ Science and Engineering Journal*, vol. 23, no. 1, pp. 115–122, 2014, ISSN: 19834071. DOI: [10.14393/19834071.2014.26140](https://doi.org/10.14393/19834071.2014.26140).
- [108] J. Zhu, M. Khurshid and Z. Barsoum, 'Accuracy of computational welding mechanics methods for estimation of angular distortion and residual stresses,' *Welding in the World*, vol. 63, pp. 1391–1405, 2019, ISSN: 18786669. DOI: [10.1007/s40194-019-00746-9](https://doi.org/10.1007/s40194-019-00746-9).
- [109] L. Wikander, L. Karlsson, M. Nasstrom and P. Webster, 'Finite element simulation and measurement of welding residual stresses,' *Modelling and Simulation in Materials Science and Engineering*, vol. 2, no. 4, pp. 845–864, 1994. DOI: [10.1088/0965-0393/2/4/004](https://doi.org/10.1088/0965-0393/2/4/004).
- [110] D. P. D. Frank P. Incropera, *Introduction to Heat Transfer*. John Wiley & Sons, 1986, ISBN: 978-0471829829.
- [111] R. Parkitny and J. Winczek, 'Analytical solution of temporary temperature field in half-infinite body caused by moving tilted volumetric heat source,' *International Journal of Heat and Mass Transfer*, vol. 60, pp. 469–479, 2013. DOI: [10.1016/j.ijheatmasstransfer.2013.01.038](https://doi.org/10.1016/j.ijheatmasstransfer.2013.01.038).
- [112] F. N. Bayock, P. Kah, P. Layus and V. Karkhin, 'Numerical and experimental investigation of the heat input effect on the mechanical properties and microstructure of dissimilar weld joints of 690-MPa QT and TMCP steel,' *Metals*, vol. 9, no. 3, p. 355, 2019. DOI: [10.3390/met9030355](https://doi.org/10.3390/met9030355).
- [113] J. Winczek, E. Gawronska, M. Gucwa and N. Sczygiol, 'Theoretical and experimental investigation of temperature and phase transformation during SAW overlaying,' *Applied Sciences*, vol. 9, no. 7, p. 1472, 2019. DOI: [10.3390/app9071472](https://doi.org/10.3390/app9071472).
- [114] D. Deng, H. Murakawa and W. Liang, 'Numerical and experimental investigations on welding residual stress in multi-pass butt-welded austenitic stainless steel pipe,' *Computational Materials Science*, vol. 42, no. 2, pp. 234–244, 2008. DOI: [10.1016/j.commatsci.2007.07.009](https://doi.org/10.1016/j.commatsci.2007.07.009).

- [115] J. Sun, J. Klassen, T. Nitschke-Pagel and K. Dilger, 'Effects of heat source geometric parameters and arc efficiency on welding temperature field, residual stress, and distortion in thin-plate full-penetration welds,' *The International Journal of Advanced Manufacturing Technology*, vol. 99, no. 1-4, pp. 497–515, 2018. doi: [10.1007/s00170-018-2516-6](https://doi.org/10.1007/s00170-018-2516-6).
- [116] T.-L. Teng, P.-H. Chang and W.-C. Tseng, 'Effect of welding sequences on residual stresses,' *Computers & Structures*, vol. 81, no. 5, pp. 273–286, 2003. doi: [10.1016/s0045-7949\(02\)00447-9](https://doi.org/10.1016/s0045-7949(02)00447-9).
- [117] *Données physiques sur quelques aciers d'utilisation courante*. Code 15004, Edition OTUA.
- [118] P.-J. Cunat, 'The welding of stainless steels,' *Euro Inox*, vol. Materials and Applications Series, Volume 3, 2007.
- [119] W. A. B. K. E. Bowditch, *Welding technology fundamentals*. Tinley Park, Ill. : Goodheart-Willcox Co., 1997.
- [120] Cai, Dong, Lin, Murphy, Fan and Yang, 'Heat source characteristics of ternary-gas-shielded tandem narrow-gap GMAW,' *Materials*, vol. 12, no. 9, p. 1397, 2019. doi: [10.3390/ma12091397](https://doi.org/10.3390/ma12091397).
- [121] G. Salerno, C. J. Bennett, W. Sun and A. A. Becker, 'Residual stress analysis and finite element modelling of repair-welded titanium sheets,' *Welding in the World*, vol. 61, no. 6, pp. 1211–1223, 2017. doi: [10.1007/s40194-017-0506-1](https://doi.org/10.1007/s40194-017-0506-1).
- [122] P. Sismanis, M. Bouzouni and S. Papaefthymiou, 'Modeling of crucial process parameters for the continuous improvement of special steels at the stoma plant,' *Journal of Materials Engineering and Performance*, vol. 27, no. 10, pp. 5130–5135, 2018. doi: [10.1007/s11665-018-3616-z](https://doi.org/10.1007/s11665-018-3616-z).
- [123] H. Wohlfahrt, T. Nitschkepagel, K. Dilger, D. Siegele, M. Brand, J. Sakkietbutra and T. Loose, 'Residual stress calculations and measurements — review and assessment of the iiw round robin results,' *Welding in the World*, vol. 56, no. 9-10, pp. 120–140, 2012. doi: [10.1007/bf03321387](https://doi.org/10.1007/bf03321387).
- [124] R. Sepe, J. Wiebesiek and C. M. Sonsino, 'Numerical and experimental validation of residual stresses of laser-welded joints and their influence on the fatigue behaviour,' *Fatigue & Fracture of Engineering Materials & Structures*, vol. 43, no. 6, pp. 1126–1141, 2019, ISSN: 8756-758X. doi: [10.1111/ffe.13180](https://doi.org/10.1111/ffe.13180).
- [125] A. Standard, 'ASTM E92-16 standard test methods for Vickers hardness and Knoop hardness of metallic,' in *Am. Soc. Test. Mater.*, vol. 82, 2016, pp. 1–27.
- [126] X. Wang, C. Shao, X. Liu and F. Lu, 'Transition and fracture shift behavior in LCF test of dissimilar welded joint at elevated temperature,' *Journal of Materials Science and Technology*, vol. 34, no. 4, pp. 720–731, 2018, ISSN: 10050302. doi: [10.1016/j.jmst.2017.06.015](https://doi.org/10.1016/j.jmst.2017.06.015).
- [127] T. E. Rao, G. R. Krishna and M. V. Kumar, 'Investigation of microstructure and mechanical properties of MIG welded mild steel plates,' *Annales de Chimie: Science des Materiaux*, vol. 43, no. 4, pp. 257–263, 2019, ISSN: 19585934. doi: [10.18280/acsm.430409](https://doi.org/10.18280/acsm.430409).
- [128] W. S. H. Wan Muda, N. S. Mohd Nasir, S. Mamat and S. Jamian, 'Effect of welding heat input on microstructure and mechanical properties at coarse grain heat affected zone of ABS grade a steel,' *ARPN Journal of Engineering and Applied Sciences*, vol. 10, no. 20, pp. 9487–9495, 2015, ISSN: 18196608.
- [129] W. Dudziński, Ł. Konat and G. Pękalski, 'Structural and strength characteristics of wear-resistant martensitic steels,' *Archives of Foundry Engineering*, vol. 8, no. 2, pp. 21–26, 2008.
- [130] Y. Wang and L. Li, 'Microstructure evolution of fine-grained heat-affected zone in type IV failure of P91 welds,' *Welding Journal*, vol. 95, no. 1, 27s–36s, 2016, ISSN: 00432296.
- [131] J. Harris, 'Engineering metallurgy: Part 1 Applied physical metallurgy,' *International Materials Reviews*, vol. 39, no. 5, pp. 213–214, 1994, ISSN: 0950-6608. doi: [10.1179/imr.1994.39.5.213](https://doi.org/10.1179/imr.1994.39.5.213).
- [132] J. Hollomon and L. Jaffe, 'Time-Temperature Relations in Tempering Steels,' *Transactions of The American Institute of Mining and Metallurgical Engineers*, vol. 162, pp. 223–249, 1945.
- [133] R. A. Grange, C. R. Hribal and L. F. Porter, 'Hardness of Tempered Martensite in Carbon and Low-Alloy Steels,' *Metall Trans A*, vol. 8 A, no. 11, pp. 1775–1785, 1977, ISSN: 0360-2133. doi: [10.1007/BF02646882](https://doi.org/10.1007/BF02646882).

- [134] F. Frendo, G. Marulo, A. Chiocca and L. Bertini, 'Fatigue life assessment of welded joints under sequences of bending and torsion loading blocks of different lengths,' *Fatigue and Fracture of Engineering Materials and Structures*, vol. 43, no. 6, pp. 1290–1304, 2020, ISSN: 14602695. DOI: [10.1111/ffe.13223](https://doi.org/10.1111/ffe.13223).
- [135] A. Hobbacher, 'Recommendations for fatigue design of welded joints and components,' International Institute of Welding, Tech. Rep., 2008.
- [136] A. Chiocca, F. Frendo and L. Bertini, 'Evaluation of residual stresses in a pipe-to-plate welded joint by means of uncoupled thermal-structural simulation and experimental tests,' *International Journal of Mechanical Sciences*, vol. 199, p. 106401, 2021, ISSN: 00207403. DOI: [10.1016/j.ijmecsci.2021.106401](https://doi.org/10.1016/j.ijmecsci.2021.106401).
- [137] S. H. Cho and J. W. Kim, 'Analysis of residual stress in carbon steel weldment incorporating phase transformations,' *Science and Technology of Welding and Joining*, vol. 7, no. 4, pp. 212–216, 2002, ISSN: 13621718. DOI: [10.1179/136217102225004257](https://doi.org/10.1179/136217102225004257).
- [138] J. D. Caprace, G. Fu, J. F. Carrara, H. Remes and S. B. Shin, 'A benchmark study of uncertainty in welding simulation,' *Marine Structures*, vol. 56, pp. 69–84, 2017, ISSN: 09518339. DOI: [10.1016/j.marstruc.2017.07.005](https://doi.org/10.1016/j.marstruc.2017.07.005).
- [139] Z. Lopez and A. Fatemi, 'A method of predicting cyclic stress-strain curve from tensile properties for steels,' *Materials Science and Engineering A*, vol. 556, pp. 540–550, 2012, ISSN: 09215093. DOI: [10.1016/j.msea.2012.07.024](https://doi.org/10.1016/j.msea.2012.07.024).
- [140] A. Siljander, P. Kurath and F. V. Lawrence, 'Nonproportional fatigue of welded structures,' in *ASTM Special Technical Publication*, American Society for Testing and Materials, 1992, pp. 319–338, ISBN: 0803114230. DOI: [10.1520/stp24166s](https://doi.org/10.1520/stp24166s).
- [141] K. Hemmesi, M. Farajian and A. Fatemi, 'Application of the critical plane approach to the torsional fatigue assessment of welds considering the effect of residual stresses,' *International Journal of Fatigue*, vol. 101, pp. 271–281, 2017, ISSN: 01421123. DOI: [10.1016/j.ijfatigue.2017.01.023](https://doi.org/10.1016/j.ijfatigue.2017.01.023).
- [142] G. Kang and H. Luo, 'Review on fatigue life prediction models of welded joint,' *Acta Mechanica Sinica*, vol. 36, pp. 701–726, 2020, ISSN: 16143116. DOI: [10.1007/s10409-020-00957-0](https://doi.org/10.1007/s10409-020-00957-0).
- [143] N. P. Andrianopoulos and A. Pikrakis, 'On the effect of hydrostatic stress on fatigue crack propagation,' *International Journal of Structural Integrity*, vol. 8, no. 2, pp. 240–255, 2017, ISSN: 17579872. DOI: [10.1108/IJSI-06-2016-0021](https://doi.org/10.1108/IJSI-06-2016-0021).
- [144] G. Qilafku, N. Kadi, J. Dobranski, Z. Azari, M. Gjonaj and G. Pluvnidge, 'Fatigue of specimens subjected to combined loading. Role of hydrostatic pressure,' *International Journal of Fatigue*, vol. 23, no. 8, pp. 689–701, 2001, ISSN: 01421123. DOI: [10.1016/S0142-1123\(01\)00030-5](https://doi.org/10.1016/S0142-1123(01)00030-5).
- [145] B. Kondori and A. A. Benzerga, 'Effect of stress triaxiality on the flow and fracture of Mg alloy AZ31,' *Metallurgical and Materials Transactions A: Physical Metallurgy and Materials Science*, vol. 45, pp. 3292–3307, 2014, ISSN: 10735623. DOI: [10.1007/s11661-014-2211-7](https://doi.org/10.1007/s11661-014-2211-7).
- [146] B. Crossland, 'Effect of large hydrostatic pressures on the torsional fatigue strength of an alloy steel,' *Proceedings of the International Conference on Fatigue of Metals*, pp. 138–149, 1956.
- [147] D. J. Burns and J. S. C. Parry, 'Effect of Large Hydrostatic Pressures on the Torsional Fatigue Strength of two Steels,' *Journal of Mechanical Engineering Science*, vol. 6, no. 3, pp. 293–310, 1964, ISSN: 0022-2542. DOI: [10.1243/jmes\\_jour\\_1964\\_006\\_042\\_02](https://doi.org/10.1243/jmes_jour_1964_006_042_02).
- [148] D. Farson, R. Richardson and X. Li, 'Infrared measurement of base metal temperature in gas tungsten arc welding,' *Welding Journal*, vol. 77, no. 9, Sep. 1998.
- [149] J. Chen, B. Young and B. Uy, 'Behavior of high strength structural steel at elevated temperatures,' *Journal of Structural Engineering*, vol. 132, no. 12, pp. 1948–1954, 2006. DOI: [10.1061/\(asce\)0733-9445\(2006\)132:12\(1948\)](https://doi.org/10.1061/(asce)0733-9445(2006)132:12(1948)).
- [150] Z. Barsoum and A. Lundbäck, 'Simplified FE welding simulation of fillet welds – 3d effects on the formation residual stresses,' *Engineering Failure Analysis*, vol. 16, no. 7, pp. 2281–2289, 2009. DOI: [10.1016/j.engfailanal.2009.03.018](https://doi.org/10.1016/j.engfailanal.2009.03.018).